Daniele Andrea Thallner

Palaeointensity of the geomagnetic field recorded in two multilevel archaeological sites in Austria

Master's Thesis

University of Leoben

Department of Applied Geosciences and Geophysics
Chair of Applied Geophysics
Head: Univ.-Prof. Dipl.-Geophys. Dr.rer.nat Florian Bleibinhaus

Supervisor: Priv.-Doz. Dr.rer.nat. Elisabeth Schnepp

Leoben, November 2016

Statutory Declaration

I declare that I have authored this thesis independently, that I have not used other than the declared sources/resources, and that I have explicitly marked all material which has been quoted either literally or by content from the used sources.

Leoben, _____ _____

Date Signature

Eidesstattliche Erklärung[1]

Ich erkläre an Eides statt, dass ich die vorliegende Arbeit selbstständig verfasst, andere als die angegebenen Quellen/Hilfsmittel nicht benutzt, und die den benutzten Quellen wörtlich und inhaltlich entnommenen Stellen als solche kenntlich gemacht habe.

Leoben, am _____ _____

Datum Unterschrift

[1] Beschluss der Curricula-Kommission für Bachelor-, Master- und Diplomstudien vom 10.11.2008; Genehmigung des Senates am 1.12.2008

Abstract

To understand the origin as well as the history of Earth's magnetic field, it is necessary to gain information about the field for longer periods of time. This information is stored in magnetic minerals in rocks in the form of a remanent magnetisation, that was gained during the cooling of the rock from a high temperature and can be determined with palaeomagnetic methods. With the age of the last cooling of the rock, which can be determined by geochronological dating methods, models of the temporal changes of Earth's magnetic field can be computed. These model curves can then be used to verify the results of the geochronological and archaeological datings.

For this thesis, samples from two archaeological sites in Austria have been worked on. The first site in Semlach/Eisner was a Roman iron production facility in Carinthia (Cech, 2008). Intensity measurements were conducted on fragments of three furnaces. The second site was the early medieval Valley settlement in Thunau am Kamp (Obenaus, 2015). Here, three oven features were sampled and the direction and intensity of their magnetisation was measured. Furthermore, the palaeointensities of three other ovens as well as ceramic shards associated with four other ovens have been determined. The intensities were measured with both domain state corrected multispecimen protocol experiments (Fabian and Leonhardt, 2010) and Thellier experiments in the version of Coe (1967).

After a discussion to show that the measured values represent the ancient magnetic field, the measured directions and intensities were used together with already published data from Semlach and Thunau (Schnepp, 2016; Schnepp et al., 2015; Schnepp, 2017) to date the features. With the exception of one feature of Thunau, where it was not possible to conduct successful intensity measurements, the archaeological ages of all features could be verified. In this thesis, three new directions and 11 new intensities have been found that can be used to compute and improve reference curves of the ancient magnetic field.

Zusammenfassung

Für die Erforschung der Entstehung sowie der zeitlichen Entwicklungen des Erdmagnetfeldes ist es notwendig, Informationen über das Verhalten des Feldes in früheren Zeiträumen zu besitzen. Diese Informationen sind unter anderem in Form von remanenten Magnetisierungen, die beim Abkühlen eines Gesteines erworben wurden, in magnetischen Mineralen gespeichert und können über paläomagnetische Methoden gemessen werden. Über die Kombination dieser Messwerte mit dem Alter der letzten Abkühlungen der Gesteine, welche über geochronologische oder archäologische Datierungsmethoden ermittelt werden, ist es möglich, aus den Daten Modelle der zeitlichen Entwicklung des Magnetfeldes zu erstellen. Diese Modelle, deren Genauigkeit mit der Menge an verwendeten Messdaten steigt, helfen umgekehrt wiederum, die Ergebnisse der geochronologische und archäologischen Datierungen als unabhängige Messmethode zu bestätigen.

Zu diesem Zweck wurden in dieser Masterarbeit Gesteinsproben von zwei archäologischen Ausgrabungen in Österreich bearbeitet. Bei der ersten Ausgrabung in Semlach/Eisner handelt es sich um eine Kaiserzeitliche Eisenproduktionsstätte in Kärnten (Cech, 2008). Hier wurden Intensitätsmessungen an Bruchstücken von drei Öfen durchgeführt. Die zweite Ausgrabung in Thunau am Kamp ist eine frümittelalterliche Talsiedlung (Obenaus, 2015). Drei Öfen wurden hier im Zuge der Arbeit beprobt und die Richtung und Intensität ihrer Magnetisierung wurde gemessen. Weiters wurden Intensitätsmessungen an Proben von drei weiteren Öfen, sowie an Keramikscherben aus den Füllungen von vier Ofenbefunden durchgeführt. Die Intensitäten wurden über Domain State Corrected Multispecimen Protokoll Experimente (Fabian and Leonhardt, 2010) sowie mit Thellier Experimenten in der Version von Coe (1967) ermittelt.

Nach einer Diskussion, ob die gemessenen Richtungen und Intensitäten das Erdmagnetfeld zur Zeit der letzten Abkühlung der Proben widerspiegelt, wurden die Messdaten in Kombination mit bereits publizierten Ergebnissen von archäomagnetischen Messungen aus Semlach und Thunau (Schnepp, 2016; Schnepp et al., 2015; Schnepp, 2017) zur Datierung der Befunde verwendet. Abgesehen von einem Befund aus Thunau, bei dem es nicht möglich war, erfolgreiche Paläointensitätsmessungen durchzuführen, konnten mit den archäomagnetischen Datierungen die archäologischen Alter der Befunde bestätigt werden. Drei neue Richtungen und 11 neue Intensitäten wurden für die Verwendung bei der Erstellung und Verbesserung von Referenzkurven des Erdmagnetfeldes ermittelt.

Contents

1. Introduction

1.1. Conceptual Formulation and Aims

This thesis deals with the dating of baked clay material and pot shards from archaeological sites in order to confirm archaeologically estimated ages. It is a practical application of palaeomagnetics in archaeology by using a natural science method. Such a confirmation may be useful if the age of an archaeological locality is not documented in historical writings or if there are only few finds like pottery, grave goods or tools allowing to date the locality via comparison with other localities with similar finds. It is also necessary if the locality was occupied in time periods where dating with other natural science methods is inaccurate. But even for a sufficiently archaeologically dated site, an additional confirmation of the age with an independent dating method is usually advantageous.

Archaeological material from two locations has been investigated: three furnaces from the Roman site Semlach/Eisner (see section 4.1) and three ovens as well as ceramic shards associated with seven other ovens from the Early Medieval site Thunau am Kamp (see section 4.2). The directions and intensities of Earth's magnetic field at the time of the last heating of the ovens are recorded in the archaeological materials. In the laboratory, these directions are retrieved with palaeomagnetic methods and the intensities with the domain state corrected multispecimen protocol method (Fabian and Leonhardt, 2010) and Coe's version of the Thellier experiment (Thellier and Thellier, 1959; Coe, 1967). The first goal of this thesis is to determine, if the measured data represents the palaeofield. If it does, then it can be compared with reference curves of the temporal change of the geomagnetic field (secular variation), which experienced relatively strong movements in this time period, to be able to date the archaeological sites. Here, the thesis aims to determine, if dating with full vector information of the palaeofield results in more precise dating results than dating with directional data only. Because the investigation used well dated archaeological

material, the final goal of this thesis is to provide well dated directional and intensity data for the improvement of the Austrian secular variation reference curve.

Precisely dated sites are a requirement, that the measured data can be used in the computation and improvement of reference curves. Well-proven reference curves of the directional changes of the magnetic field already exist for the area of Central Europe (e.g. Schnepp and Lanos, 2005, 2006). However, reference curves for intensities have mainly been modelled for Western Europe due to few intensity data in Central/Eastern Europe. The existing curves are continuously updated with new data to improve the curves and minimize their error envelopes, while new curves can be computed if enough data is available. Not only does this lead to an improvement in future archaeomagnetic dating projects, it also helps understanding and model Earth's magnetic field of the last few thousand years, (e.g. Batt, 1997; Gallet et al., 2002; Korte et al., 2009), as well as the dynamics of Earth's core (e.g. Christensen et al., 2010). The next chapter deals with the basics of the physical background as the Earth's magnetic field and magnetism of archaeological materials, while chapter 3 delineates the principals of archaeomagnetism.

2. Physical Background

2.1. Earth's Magnetic Field

Earth's magnetic field (EMF) behaves approximately like a dipole field of a relatively small but very strong bar magnet positioned close to Earth's center as shown in figure 2.1a. This geocentric axial dipole accounts for about 90% of the observed field. The other 10% origin from higher order terms of the non-dipole field (Meert et al., 2003). In review papers from the time period between the 1950ies (Creer et al., 1954; Cox and Doell, 1960) and today (Merill and McFadden, 2003), it is assumed that the best fitting geocentric dipole axis does not match Earth's rotational axis. However, averaged over several million years, William Gilbert's assumption that the axis can be considered as geocentric and axial has been the foundation of the field of paleomagnetism (Tauxe, 2005). Therefore, the Earth's magnetic field can be described rather well by assuming a permanent magnet in Earth's center. Due to the fact that, with an average geothermal gradient of 30 °C/km, the temperature below depths of 20-30 km at about 500-600 °C is already higher than the Curie temperature of most crustal rocks, which makes the existence of a permanent magnet at Earth's center impossible. Today it is agreed upon, that Earth's liquid core is the source of the magnetic field. The physical processes are defined in a rotating reference system with the Maxwell equations and the Navier-Stokes differential equations and are merged in the term "geodynamo". The geodynamo is powered by convection, which gains energy from heat and crystallisation processes of the inner core. The transformation of thermal energy in mechanical and ultimately magnetic energy is enabled by the motion of the liquid iron and its modification by the Coriolis force due to Earth's rotation (Christensen et al., 2010). Since the end of the last millennium, it has been possible to simulate a self sustaining geodynamo in complex computer simulations (e.g. Jault and Cardin, 1999; Davies and Constable, 2014). Complementary experiments have been conducted in Riga and Karlsruhe (Stieglitz, 2001).

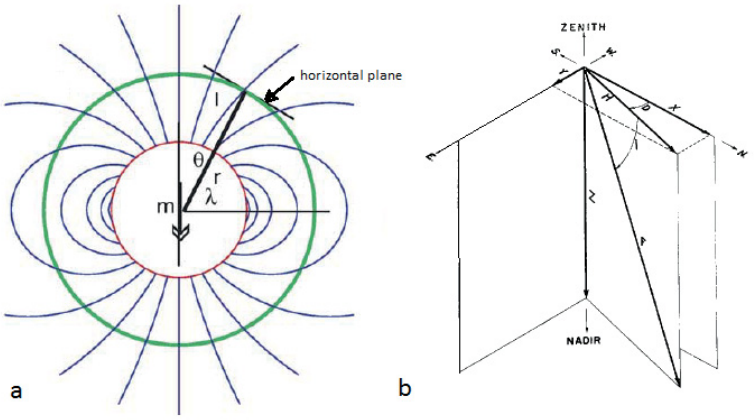

Figure 2.1.: a: Field lines of Earth's magnetic field with moment m, modified after (Tauxe, 2005); b: Relations of field vector components, where D = declination, I = inclination, X = North component, Y = East component, H = Horizontal intensity, Z = Vertical intensity and F = Total intensity. (Nelson et al., 1962)

The measurement of Earth's magnetic field at any point on Earth's surface consists of the determination of the field's direction and intensity. These two parameters are defined as a field vector at any given point on Earth's surface. Projecting this vector on a horizontal plane gives the horizontal component H of the vector. The direction of H defines a vertical plane, the so-called magnetic meridian, through the Earth's center. The angle between magnetic meridian and geographic meridian is called declination D. Here, the declination is measured clockwise starting from north in the range from 0° to 360°. The angle on the vertical plane between the field vector and its horizontal component is called inclination I. Per definition, the inclination is positive if the field vector points "downwards" in relation to the horizontal plane (Nelson et al., 1962). The geometrical relations of the vector components are pictured in figure 2.1b.

2.2. Secular Variation

Direct measurements of Earth's magnetic field have been conducted for about several hundred years. Starting with scattered land based observations in the 16^{th} century and magnetic observations on ships since the 17^{th} century, declinations and inclinations were measured (Jackson et al., 2000). After Carl Friedrich Gauss developed a method for measuring absolute intensities in 1832 (Jackson et al., 2000), magnetic observatories were

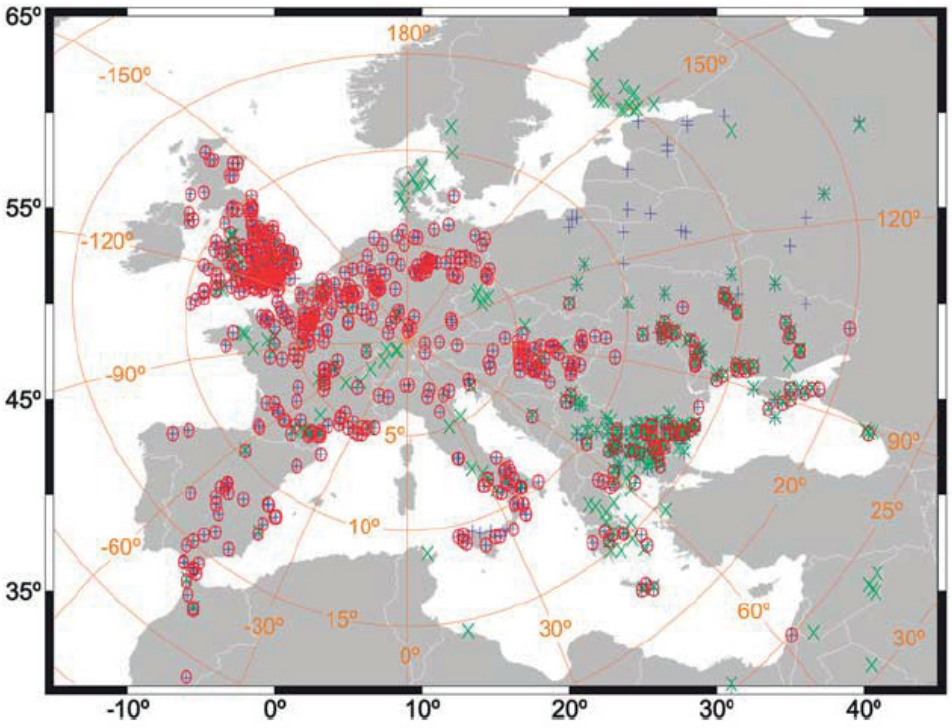

Figure 2.2.: Spatial distribution of measurement data of declination (red), inclination (blue) and intensity (green) in Europe used for creation of SCHA.DIF.3K, a regional archaeomagnetic model for Europe. (Pavón-Carrasco et al., 2009)

founded all over the world. These observatories enabled measurements at the same location in regular intervals and were far more accurate than the older data from ships due to their difficulties of determining their exact location. These measurements showed that the direction and intensity of the magnetic field are not constant. Over the course of hundreds of years, changes of inclination of up to 15° and of declination and of up to 40° can occur (Gallet et al., 2002). These variations at any location can be divided into categories of transient variations, occurring on a daily time frame due to magnetic storms, sun activity and similar influences, and secular variations that are slower changes of the main field due to changes in the convectional flow in Earth's core. With the mentioned direct measurement, models of the palaeosecular variation (PSV) of Earth's history can only be computed for the time frame of these measurements with high error margins for the time before the 19^{th} century. The secular variations before the existence of these direct measurements can not be measured directly but can be determined as described in chapter 3. In time periods of millions of years, the dipole field has not only changed but also reversed completely about

every 250 000 years. (Soffel, 1991; Nelson et al., 1962; Tauxe, 2005)

Starting with pioneering work of Thellier (1938) in France, palaeosecular variation has been used for dating purposes and to uncover the dynamics of Earth's core and the EMF. Because of the complexity of Earth's magnetic field, not being a perfect dipole field, secular variations differ for every point on Earth's surface. As there is no known pattern of the spatial distribution of secular variation, it is not trivial to reduce field data of one location to field data of another location (Schnepp, 2007) which resulted in the development of models for palaeosecular variation, because archaeomagnetic dating is only possible in areas where sufficient field reference data or a valid PSV model is available (Ech-Chakrouni et al., 2013).

However, the global distribution of reference data for PSV models is not consistent due to different developments in archaeomagnetism in different countries. While the majority of data origins from countries like Great Britain (Batt, 1997), France (Thellier, 1981; Gallet et al., 2002; Hervé et al., 2011), Germany (Schnepp and Lanos, 2005) and Bulgaria (Kovacheva, 1997), countries like Austria (Schnepp and Lanos, 2006; Schnepp et al., 2015) or Italy (Tema et al., 2013) are slowly catching up. The distribution of data in Europe published until 2009 can be seen in figure 2.2.

Different approaches have been taken to create PSV models from the available archaeomagnetic data. Among the first to try to create a global PSV model, Daly and Le Goff (1996) computed regional curves of the PSV. They took the available archaeomagnetic world data, sorted them according to their geographical region and corrected them to correspond to a single site ('world site') that was associated to the geographical region of the data. Such a world site was created in the geographical center of every country, where the amount of data for the last 2000 years was sufficient for a statistical analysis. Using a reduction through a virtual geomagnetic pole (VGP) (Irving, 1964), they relocated declination, inclination and intensity from the regional sites, where a well dated archaeological structure has been studied, to the corresponding world site. Knowing that this relocation process introduced an error that grows with the distance between regional and world site, the sparse distribution of studied archaeological structures forced them to use regional sites that were not in close surroundings of the world site (e.g. the regional sites in France are inside a circle with a diameter of roughly 1000 km around the French world site Paris). Using the bivariate extension (Le Goff, 1990) of the Fisher statistics (Fisher, 1953) and incrementally moving time windows, smoothed curves of mean values and standard deviations for declination,

inclination and intensity, averaged over 80 year intervals and weighted according to the number of samples from each site, were computed for each world site for the last 2000 years. A first improvement of this sliding window method was published by Le Goff et al. (2002). Here, the size of the time windows was no longer a constant value, but dependent on the data density at each time interval.

Extending the approach of Le Goff et al. (2002), Lanos et al. (2005) introduced a Bayesian hierarchical modelling method to account for the different sources of scatter and errors in archaeomagnetic data. Their aim was to take into account all the errors resulting from the different number of specimens taken from each sample or site. By examining the sampling methods, they distingueshed five hierarchical sampling levels (measurement-, specimen-, sample-, site- and field hierarchical level) and their associated errors. This allows to improve the mean values at each level by raising the number of observations (as long as the variables at each level are independent), while the bivariate statistics (Le Goff, 1990) and the weighted univariate statistics (Kovacheva, 1997; Batt, 1997) only observe the data at the window level and imitate hierarchical behaviour of the data by weighing. As a moving average method, it is well adapted to evenly distributed well dated data. Dating errors and unevenly distribution of the used data can lead to large errors because the Bayesian elliptic distribution is influenced by the window width. This method was refined by introducing prior knowledge like the archaeological dating ranges or stratigraphic constraints (Schnepp et al., 2003; Lanos, 2004). Meanwhile many regional PSV curves for Europe exist, e.g. for France (Hervé et al., 2011; Genevey et al., 2016), Germany (Schnepp and Lanos, 2005) or the United Kingdom (Zananiri et al., 2007).

In contrast to the moving window methods to obtain local curves, Korte et al. (2009) developed temporally continuous global spherical harmonic models, using multi-pole expansions. Following a series of snapshot models (Constable et al., 2000), the spherical harmonic descriptions were expanded to higher degrees while pseudo-structures were suppressed with regularization techniques. This led to a series of global models that were created by using all available archaeomagnetic and sediment data for the last 3 ka from five datasets (Korte et al., 2005). The resulting models are the 'Continuous model from Archeomagnetic and Lake Sediment data' (CALS3K.x) series. These global models are usually very smooth due to the tradeoff between the spatial and temporal smoothness and the fit to the global data. Pavón-Carrasco et al. (2009) used an approach similar to the CALS models while trying to avoid the high smoothness of the global models as achieved by the local PSV curves. This lead to the development of regional SHA.DIF.x models that use the spherical cap

harmonic analysis technique on Bayesian European PSV curves for an European model. In this method, the EMF is represented in a closed conical domain by a complete set of functions.

All these models suffer from the limitations given by the uneven data density in different locations. Areas with sparse data coverage lead to too smooth areas in the models. In addition to the inhomogeneous spatial distribution of data, there are also gaps in the temporal distribution of data. This increases the error margin of the models in these time periods even if the spatial distribution was sufficient. Time errors are also a major error source, especially for models that use time window techniques. However, the quality and precision of archaeomagnetic dating curves is not only dependent on the amount of data and their spatial and temporal distribution, but also on the reduction to the world sites, the precision of every archaeomagnetic measurement of every site and especially the precision of the archaeological dating (Le Goff et al., 2002).

2.3. Magnetic Fields in Materials

Due to the movement of electrons around the atomic core, all atoms have magnetic dipole moments. In addition, each electron has its own magnetic moment originating from its spin. The resulting magnetic field of an atom is therefore dependent on the arrangement of electrons. The alignment of magnetic dipoles in an external field leads to an amplification of the field, meaning that in magnetically polarized materials magnetic fields, that are parallel to the magnetic dipole moments, are generated by the magnetic dipoles. According to the behaviour of the molecules of a material in an external magnetic field, all materials can be divided into five categories: paramagnetic, diamagnetic, ferromagnetic, ferrimagnetic and antiferromagnetic matter.

Para- and ferromagnetic materials consist of atoms or molecules with permanent magnetic dipole moments, where the interactions between the magnetic dipoles in paramagnetic matter is so weak, that it is rarely possible to detect a preferred magnetic direction. By applying an external magnetic field the dipoles are partially oriented in the direction of the field, leading to an amplification of the resulting field. The interaction of magnetic dipoles in ferromagnetic materials is so strong, that even weak external magnetic fields are strongly amplified. Antiferromagnetism and ferrimagnetism can be compared to superposition of

the magnetic properties of two ferromagnetic materials with different alignments of dipoles in a single material. Diamagnetism describes materials that do not have a permanent magnetic moment. Is an external field applied, then the magnetic dipoles align antiparallel and attenuate the field. Diamagnetism can be found in all materials, but it is so weak that it is usually masked by para- or ferromagnetism.

If a material is put in an external magnetic field and the permanent as well as the induced magnetic dipoles align accordingly, then the material is called magnetic. There, the magnetisation M is defined as the resulting magnetic moment per volume element:

$$\vec{M} = \frac{d\vec{m}_m}{dV} \tag{2.1}$$

If the external magnetic field $\vec{B_o}$ is generated with a very long coil with length L, N turns and the current I, and a material is put inside the coil then the material is magnetised by $\vec{B_o}$ and has the magnetisation $\vec{M}$. The resulting magnetic field inside the coil is given by

$$\vec{B} = \vec{B_o} + \mu_o * \vec{M}, \tag{2.2}$$

where μ_o is the permeability of vacuum or the magnetic field constant with the SI-value of $\mu_o = 4 * \pi * 10^{-7}$ [Vs/Am]. Without the material and only the coil present the magnetic field is given by

$$B_o = \mu_o * n * I \text{ with } n = \frac{N}{L}. \tag{2.3}$$

This information and the definition of magnetic field strength of $\vec{B} = \mu * \vec{H} = \mu_r * \mu_o * \vec{H}$ with a relative permeability of $\mu_r = 1$ result in

$$H = n * I. \tag{2.4}$$

Is the coil filled with a material while I is kept constant, then H inside the coil remains constant because it is only dependent on the current in the coil. In contrast, B changes due to the change of $\mu_o * \vec{M}$ in equation 2.2. Therefore, a magnetic field is entirely characterized by the vectorial value of $\vec{B}$, where the intensity of B is a parameter for the strength of the magnetic field. The magnetisation of a material and the magnetic field strength H are connected via the proportionality constant κ_m, the dimensionless susceptibility, that is connected with the permeability of a material via

$$\mu = \mu_o * (1 + \kappa_m). \tag{2.5}$$

The interaction of magnetic moments in ferro(i)magnetic materials is so strong, that the moments align themselves in small regions even without an external field. These areas of microscopic scale are called magnetic domains. Inside these domains, all magnetic moments are aligned equally which results in a submicroscopic local maximum magnetisation inside one domain. These domains are separated by walls made of dipoles which are not aligned with either of the adjacent domains. The energy necessary to keep up such a wall is called wall energy. The magnetic energy stored in one magnetic domain is called stray-field energy. Every magnetic particle tries to keep its overall energy level as low as possible (Evans and Heller, 2003). This is achieved by subdividing its magnetic domains until the wall energy of the rising amount of walls prevents the overall energy of the particle from being lowered by creating more domains and an optimum amount of domains n_{opt} is found depending on the particle or grain size. If a particle has the size of a domain that is not subdivided further due to the prevention of a decrease of overall energy by the energy of a new wall that would be created at the subdivision, then this particle is called single domain particle. Particles that are larger and therefore contain more than one magnetic domain are called multi-domain particles. (Soffel, 1991)

Is an external magnetic field applied to a ferro(i)magnetic sample, then the alignments of the magnetic moments change due to the external magnetic field in a way that the averaged orientation of the magnetic domains does not equal zero and the resulting overall field is amplified. Figure 2.3 shows the magnetisation M of a ferromagnetic sample as a function of the external field strength H. In case of an initially non-magnetised material, M rises with rising H. The curve flattens in the proximity of point P_1, where the magnetization of the material reaches the saturation value M_s, the maximum possible magnetisation of the sample. Above the saturation, the field B in the coil is only rising as H is rising. However, the sample is not magnetised any further from this point forward. If the external field decreases, the magnetisation of the material does not decrease the same way as it increased. The reason for this is, that not all magnetic domains rotate back to arbitrary directions. Even if the external field is zero, a magnetic field, called the remanent magnetic field M_{rs}, is still active due to the residual magnetisation of the material. Is the external field now reversed and raised in the opposite direction, then the overall magnetic field can be brought back to zero. The field necessary for this is known as coercive field H_R. Is the field raised further, then the magnetic moments of the sample align themselves again in direction of the external field until the material reaches saturation at point P_2. If the external field is now again moved to $H = 0$, then the material again has a remanent

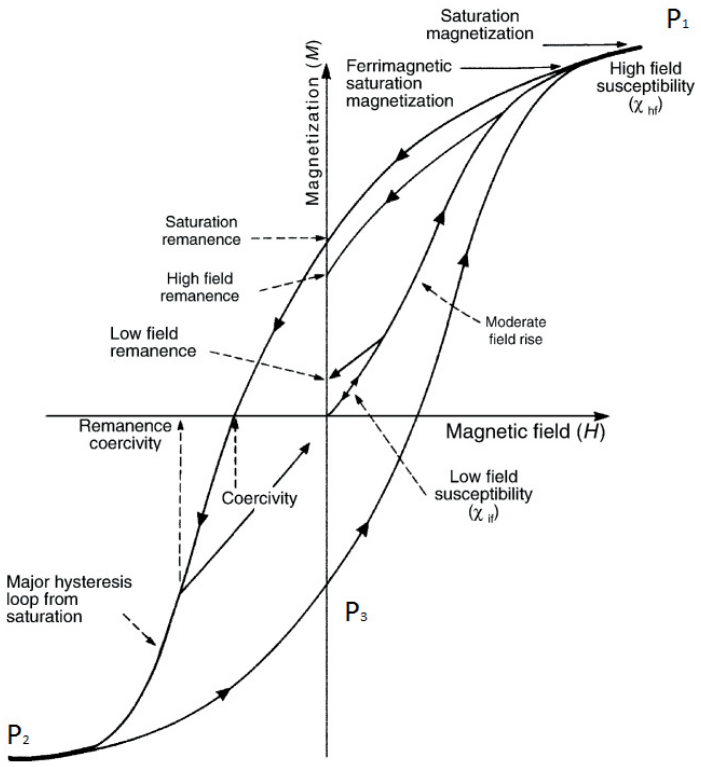

Figure 2.3.: Function of the magnetisation M of a ferromagnetic sample as a function of an external field strength H. Modified after (Gubbins and Herrero-Bervera, 2007).

magnetisation at P_3, but in the direction of the last magnetisation which is the opposite direction as the first time. Is H now reversed and raised one more time, then the so-called hysteresis loop completes in point P_1. This means that the magnetisation of a material is strongly dependent on its past history and every point inside the loop can be reached with appropriate changes of H.

The area that is enclosed by the hysteresis curve is proportional to the amount of energy that is lost as heat in the process of magnetising or demagnetising. If the enclosed area and therefore the loss of energy while magnetising is small, then the material is called magnetically soft. Contrarily, a material is called magnetically hard if the enclosed area is large. When a ferro(i)magnetic material is exposed to heat, then the rising kinetic energy of the atoms influences the interactions between the magnetic moments and therefore the alignment of the magnetic moments. As described above, by reaching a material-specific critical temperature, the so-called Curie temperature, the kinetic energy of the

atoms is so high that the magnetic moments do not interact any more and the material therefore has a paramagnetic character as long as the temperature remains above the Curie temperature. If the temperature is lowered below the Curie temperature, the material regains its ferromagnetic character. The small temperature range below the Curie temperature, where the movement of the magnetic moments is "blocked" is called blocking temperature. Here the relaxation time of the magnetic moments increases from values of about 1 s to values of up to 10^8 years (Soffel, 1991; Nagata, 1961; Gubbins and Herrero-Bervera, 2007).(Tipler, 1994)

Rocks usually contain a small fraction of magnetic minerals, usually iron (hydr)oxydes or iron sulphides. Typical magnetic minerals are Magnetite (Fe_2O_4), Titanomagnetite (Fe_2TiO_4), Hematite (Fe_2O_3), Pyrrhotite ($Fe_{1-x}S_{x=0to0.2}$) and Goethite (FeOOH). As the rocks form, these minerals' domains statistically align with the EMF and can preserve the field as natural remanent magnetisation (NRM). Depending on the process during which the NRM was imprinted on the minerals, several types of remanent magnetisation can be distinguished.

2.4. Types of Remanent Magnetisation

Natural Remanent Magnetisation (NRM)

A weak remanent magnetisation as described in section 2.3 can be observed in all naturally occurring rocks due to the presence of ferro(i)magnetic minerals in the rocks. It is called natural remanent magnetisation (NRM). The content of ferro(i)magnetic minerals is often so small, that highly sensitive measurement instruments are necessary to detect them. Several physical and chemical processes exist that can create the NRM and it is usually a combination of different types of remanent magnetisations as the processes affect different grain fractions, blocking temperatures or coercive force ranges (Soffel, 1991; Butler, 1992). The most relevant types of remanent magnetisation for palaeo- and archaeomagnetic evaluations are briefly described in this section.

Thermoremanent Magnetisation (TRM)

Thermoremanent magnetisation (TRM) is created when rocks are cooled down from a temperature higher than the maximum Curie temperature of the magnetic minerals in an external field H, such as the Earth's magnetic field or a laboratory field (Thellier, 1938). As the heated rocks are penetrated by the field lines of the external field, the magnetic moments roughly align themselves with the field lines. When the rock is now cooled below the Curie temperature and the magnetic particles in the minerals reach their blocking temperature, the magnetic moments remain in their aligned direction and the TRM is imprinted. Here, the direction of the created TRM is parallel to the direction of the external field and the intensity is proportional to the external field intensity. The intensities of the TRM and the external field show linear relation if the intensity of H is not too high depending on the mineral (e.g. lower than two times the intensity of the EMF for Magnetite) (Nagata, 1961). It can be assumed that the TRM of a rock is a representation of Earth's magnetic field at the last time the rock was cooled down from a temperature above its Curie temperature. The creation of a TRM is well-understood for single domain particles, while multi-domain particles show a more complicated behaviour due to interactions of domain walls and crystal structure of the minerals (Néel, 1949; Evans and Heller, 2003; Biggin and Poidras, 2006a). In comparison to most other remanence types, the TRM is the most resistant to demagnetisation processes (Soffel, 1991).

Partial Thermoremanent Magnetisation (pTRM)

Similar to the TRM, a rock that is heated to a temperature below the Curie temperature and then cooled in an external field H gains a magnetisation that is proportional to H, the partial thermoremanent magnetisation (pTRM). Here, only those ferro(i)magnetic minerals are magnetised, whose blocking temperatures have been reached during the heating. The mineral grains with higher blocking temperatures are not influenced by H. Thellier (1938) showed that the sum of all pTRMs of a rock equals its TRM. The formation of a pTRM is again similar for single-domain and multi-domain particles, but more complex for the latter due to the interaction of domain walls and crystals as well as the broader range of blocking temperatures of multi-domain particles (Néel, 1949; Soffel, 1991; Gubbins and Herrero-Bervera, 2007).

Chemical Remanence (CRM)

A chemical remanence (CRM) is formed when a ferro(i)magnetic mineral crystallises below its Curie temperature in the presence of an external magnetic field H, e.g. during weathering of the minerals. With growing size of the crystals, they enter various stages from superparamagnetic to single-domain to multi-domain behaviour. CRMs show similar characteristics as TRMs like high blocking temperatures and high coercive forces and are therefore hard to distinguish. The CRM shows a proportionality to H, which is dependent on the sizes of the ferro(i)magnetic minerals and can therefore not be used to determine the intensity of a palaeofield, but can cause errors in the measurement of intensity (Soffel, 1991; Butler, 1992).

Other Types

If rocks are exposed to magnetic fields over long time periods they can adopt a remanent magnetisation in the direction of the external field. If the external field is weak, then the remanence is called viscous remanent magnetisation (VRM). If the external field is strong, the remanence is called isothermal remanence (IRM). In contrast to the VRM, the IRM magnetises a material in a short time period. It is used to determine (magnetic) mineral types in rocks by creating hysteresis loops. The VRM is considered as noise in palaeomagnetics and can often easily be removed by demagnetising the rocks. Other remanences that are not relevant in this thesis, origin from the sedimentation of grains with magnetic minerals, that align themselves according to an external field during sedimentation (depositional remanent magnetisation DRM and post-depositional remanent magnetisation PDRM) (Soffel, 1991).

Anhysteretic Remanent Magnetisation (ARM)

The ARM of a rock sample is never a part of the NRM. It is an artificially created magnetisation that is similar to a TRM. Instead of heating the sample above the Curie temperature, the sample is here exposed to an alternating field (AF) with an amplitude, higher than the maximum coercive force of the magnetic minerals in the sample. This is again done in the presence of an external field H with a much smaller amplitude than the

alternating field. If the amplitude of the AF is steadily lowered to zero, while H is kept constant, then an ARM is created that is proportional to H (Soffel, 1991; Gubbins and Herrero-Bervera, 2007).

2.5. Magnetism of Archaeological Materials

In order to measure the PSV in the last few thousand years, archaeological material is used for so called archaeomagnetic investigations. Typically, all kinds of artefacts like bricks, ceramic containers or shards of ceramics as well as parts of ovens and fireplaces are used because they meet the demands needed for an archaeomagnetic investigation. For one, the before mentioned artefacts consist of a clayey, loamy material that contain traces of iron-bearing minerals like Magnetite, Iron-Hydroxides or Hematite which are able to store a well quantifiable record of Earth's magnetic field (Soffel, 1991).

In addition, the material has to be baked. A TRM is imprinted, if the material is heated above the Curie temperature of its ferro(i)magnetic phases during the baking process. Or at least a pTRM with high blocking temperatures on the material is created if the Curie temperature is not reached. As minerals alter at high temperatures, new magnetic carriers can be formed or changed through the transformation of minerals, like goethite to hematite at temperatures between 200 and 400 °C or magnetite to maghemite through oxidation at low temperatures (Schwertmann and Taylor, 1989; Hanesch et al., 2006).

Whenever an artefact like an oven or a fireplace is fired above its Curie temperature, all initial magnetic information is wiped and a new TRM is imprinted during cooling. Therefore only the record of Earth's magnetic field at the time of the last heating/baking is stored. Due to the small grain sizes of the magnetic mineral components, it is not unusual to also find a relatively high VRM in the NRM that has to be removed before analysing the characteristic remanence of the baked clay (Soffel, 1991).

Not all archaeological artefacts can be used to determine all information about the palaeofield. The direction of the palaeofield can only be obtained from an artefact that has not been moved since the last time it was heated and that can be sampled in-situ. Some fired material like bricks or pottery fragments can sometimes be used to determine the inclination of the palaeofield if the artefacts were stacked in a regular way during their production (McIntosh and Catanzariti, 2006).

The archaeointensity can be determined from all artefacts that carry the TRM of the palaeofield. For this, the samples do not need to be oriented. Therefore, intensity measurements are also possible for collapsed parts of ovens, pottery or bricks. A major concern for all artefacts that are not found at their location of the last heating, which can often be the case for pottery, bricks or tiles, is that their location of origin is not known. Full vector analysis of the palaeofield can therefore only be done on artefacts that are oriented and of known location. This is usually the case for furnaces, fireplaces and similar archaeological features.

3. Principles of Archaeomagnetism

3.1. Estimation of Field Vector Direction

There are several methods to analyse the remanent magnetisation of a rock sample by demagnetising the samples progressively. These methods are alternating field, thermal, chemical and shockwave demagnetisations (Soffel, 1991). The first two kinds will be discussed in more detail because they have been used in the course of this thesis.

Basis for the following demagnetisation methods is, that rocks with some range of particle sizes have also a certain range of blocking temperatures and coercive forces of the particles (Néel, 1949). This is used in the demagnetisation processes in a way that by application of a temperature or a field, the relaxation time of certain grain size fractions is lowered and the particles of these fraction lose parts or all of their magnetisation (Soffel, 1991).

For an alternating field (AF) demagnetisation a sample is exposed to an external alternating field field with known intensity and constant frequency. For each of the three spatial directions the amplitude is quickly increased up to a maximum amplitude and subsequently slowly lowered to zero (Soffel, 1991). Magnetic moments of particles with a coercive force smaller than the amplitude of the external field align themselves with the alternating direction of the external field. During the slow decrease of amplitude, less and less moments are influenced by the external field and the remanence of the fractions with coercive forces smaller than the maximum amplitude averages to zero. If the sample is not shielded from external fields other than the AF, this process results in a creation of an ARM. Hence for demagnetisation purposes the experiment is carried out in a space shielded from the EMF as far as possible and carried out in all three perpendicular axes of the sample's coordinate system. The process is repeated several times with the AF's intensity increased for every step until the NRM of the sample is down to 10% of the initial value or it is no longer possible to increase the AF's intensity due to instrumental limitations.

A lot of information can be gained from analysing the behaviour of the sample's NRM decrease along the demagnetisation steps. The different types of remanent magnetisations create different forms of demagnetisation curves. A TRM as well as a CRM usually shows a high resistance against the demagnetisation, while VRMs and IRMs are usually easily removed. The AF intensity, that results in a loss of 50% of the initial NRM is called the "median destructive field" (MDF) that correlates to the coercivity which can be used to determine the mineral content of the sample (Soffel, 1991).

When thermally (TH) demagnetising a rock sample, the approach is quite similar to an AF demagnetisation. Instead of an alternating field, heat is applied to the sample while it is shielded from all external fields to avoid imprinting a pTRM while cooling down. Here, the magnetic information of all particles with a blocking temperature lower than the maximum temperature gets deleted. Again, several heating steps with increasing values of maximum heat are done. In contrast to AF demagnetisation, SD and MD particles can behave differently due to the broader range of blocking temperatures for MD particles. Samples with a high percentage of SD particles are usually quite resistant against the TH demagnetisation up to the small range of blocking temperatures that are a bit lower than the Curie temperature. At that point, NRM of the sample decreases quickly. Samples with a high fraction of MD particles may already lose a significant amount of its NRM at temperatures far below their Curie temperature. Another difficulty that can emerge while heating is the alteration of minerals at higher temperatures. The level of alteration can and should be observed by measuring the sample's susceptibility after each heating step (Dunlop, 1974; Soffel, 1991; Gubbins and Herrero-Bervera, 2007).

Similar to AF measurements, TRM and CRM show again high resistance to the demagnetisation due to the blocking temperatures being close to the Curie points of these remanence types. All samples can however be completely demagnetised if the maximum temperature exceeds the Curie temperatures and all external fields are perfectly compensated. VRM fractions of NRM show different blocking temperatures depending on the timespan of the imprinting. "Younger" VRMs that come from external fields that have only been affecting the sample for a short time show generally lower blocking temperatures than "older" VRMs due to the presence of the EMF. (Soffel, 1991)

In order to find the direction of the TRM caused by the palaeofield vector, one has to distinguish the respective characteristic remanent magnetisation (ChRM) direction from secondary components by analysing the three orthogonal components of the residual NRM

at every demagnetisation step. In contrast to other remanence types, the ChRM is not created by a chemical or natural physical process. It is rather a nomination of a defined part of the NRM for a specific problem, e.g. the TRM formed at a rock's cooling below its Curie temperature. Usually, rocks can have more than one ChRM. By analysing a rock's NRM using demagnetisation experiments, one can distinguish the different ChRMs (Soffel, 1991). Zijderveld (1967) proposed a way of doing this by plotting the residual NRM at every step in an orthogonal projection of the field vector on the planes of X (North-component) and Y (East component) as well as Y and Z (vertical component). In such Zijderveld diagrams it is possible to distinguish the different remanence types and their coercive forces or blocking temperatures during the destruction of the NRM. If an NRM consists only of one magnetisation type (e.g. the TRM of the last heating of the sample), then the measurement points converge to the origin on a straight line. If several magnetisation types are demagnetised, then the measurement points may have several linear segments, form curved lines and may not converge to the origin, as shown in fig 3.1 a. In this figure, a secondary component is removed in the demagnetisation steps up to 360 °C. Above this temperature, a single component is demagnetised and the measurement points converge to the origin. If the responses of different magnetisation types to the demagnetisation are similar, it may not be possible to distinguish them and the diagram will show only one component with a wrong direction (Merill et al., 1998). Different NRM components can be further analysed with the method of difference vectors that will not be further discussed in this thesis.(Soffel, 1991)

An illustration of direction's behaviour is done by plotting them in a polar version of a Schmidt net. Here, the inclination and declination are plotted instead of the Cartesian components. Figure 3.1b shows the change of direction during a demagnetisation. If only one NRM component would be present, the measurement points for the different demagnetisation steps would stay at one point in this projection because neither the declination nor the inclination would change. Starting with an NRM measurement at declination and inclination of roughly 180°/-15°, a secondary component is removed with demagnetisation steps up to 10 mT and a single component is left for the following demagnetisation steps up to 50 mT at 150°/30°. In the last two demagnetisation steps, declination and inclination change again, possibly due to remaining hard magnetic components. The directions of the components can be found with principal component analysis (PCA) (Kirschvink, 1980). This is done by transforming the orthogonal coordinate system to one that corresponds to the data geometry and estimating the directions of planes and lines of a least-squares fit along the

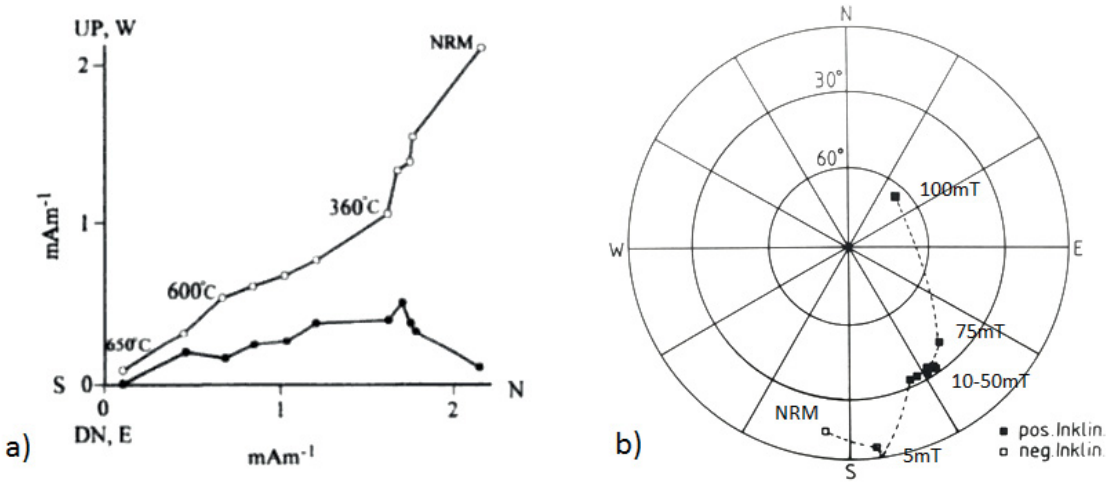

Figure 3.1.: a) Exemplary Zijderveld diagram of a TH demagnetisation, showing the N vs W plot (black dots) and Up vs. W plots (white dots) for different temperatures (from Merill et al., 1998); b) Exemplary illustration of an AF demagnetisation in a Schmidt net showing demagnetisation steps up to 100 mT (modified after Soffel, 1991).

demagnetisation path.

To find the direction of the NRM or ChRM of an archaeological feature, the directions of serveral oriented samples taken from it are combined. Due to local differences in the NRM compositions, orientation errors and other effects, the directions of the different samples are more or less scattered and a mean value has to be found. When doing this, a vectorial average of unit vectors with all obtained ChRM directions is calculated using the so called Fisher statistics (Fisher, 1953). When several specimens from the same samples were analysed, the mean ChRM is found as hierarchical means for each independently oriented sample from its specimens which are then averaged for the site or structure (Lanos et al., 2005).

When calculating the mean direction, the values for the samples are assumed as accurately measured and not dependant on the NRM's intensities. The unit vectors for the value pairs D_i and I_i of i samples are split into their North- (l_i), East- (m_i) and vertical (n_i) components. They are calculated by

$$l_i = cos(D_i) * cos(I_i) \tag{3.1}$$

$$m_i = sin(D_i) * cos(I_i) \tag{3.2}$$

$$n_i = sin(I_i) \tag{3.3}$$

With these components, the vector sum $\vec{R}$ of the i unit vectors and the mean values for the North- (X), East- (Y) and vertical (Z) components can be calculated with

$$\vec{R} = \sqrt{(\sum l_i)^2 + (\sum m_i)^2 + (\sum n_i)^2} \tag{3.4}$$

$$X = \frac{1}{R} * \sum l_i \; ; \; Y = \frac{1}{R} * \sum m_i \; ; \; Z = \frac{1}{R} * \sum n_i \tag{3.5}$$

Now, the declination and the inclination of the mean direction can be calculated by

$$tan(D) = \frac{Y}{X} \tag{3.6}$$

$$sin(I) = Z \tag{3.7}$$

where D and I assume values between 0° and 360° and -90° and +90°. (Soffel, 1991)

The statistical method of Fisher (1953) allows the quantification of the scatter around the mean value. It is assumed that the scatter is grouped around the mean value following a Gaussian distribution on the sphere. The probability density P(ϕ) of the Fisher statistic is given by

$$P(\phi) = \frac{k_0}{4\pi sinh(k_0)} * exp(k_0 cos(\phi)) \tag{3.8}$$

where ϕ is the angle between a data point and the mean value of the group, and k_0 is the precision parameter. k_0 assumes values between ∞ for identical values and 0 for randomly distributed values. For values of $k_0 \geq 3$, an approximated value k can be used which can be calculated by

$$k = \frac{(N-1)}{(N-R)} \tag{3.9}$$

where N is the number of used directions and R is the vector sum of the unit vectors, as calculated in equation 3.4. Due to inevitable scatter of the vectors, R is always smaller than N. Datasets with values of $k \leq 3$ are usually unreliable and useless for a palaeomagnetic analysis. To show a confidence limit of a mean value, the value of α_{95} is usually also calculated. This value represents the radius of a circle on the sphere. Inside this circle there is a probability of 95% to find the true value. α_{95} can be calculated with

$$cos\alpha_{95} = (1 - \frac{(N-R)}{R}[(\frac{1}{P})^{1/(N-1)} - 1]) \tag{3.10}$$

Palaeomagnetic mean values are usually presented with their precision parameter k and the confidence radius α_{95}. (Fisher, 1953; Soffel, 1991)

3.2. Estimation of Palaeointensity

In addition to the analysis of the palaeofield vector's direction, a determination of the field's absolute intensity is also necessary to fully understand the ancient field (Gubbins and Herrero-Bervera, 2007). Several methods have been developed to measure such palaeointensities. Not all types of NRM can be used to measure palaeointensities. A suited NRM type has to store the information about the palaeofield in a well understood way and it has to be reproducible in the lab. While types like IRM do not store information about the palaeofield, types like CRM cannot be reproduced in the laboratory. TRM (or pTRM) do meet the requirements and can therefore be used to determine palaeointensities. (Soffel, 1991) Two methods that use TRM/pTRM do determine palaeointensities have been used for this thesis and are discussed in detail below. Other methods like the Shaw method (Shaw, 1974) will not be discussed here.

3.2.1. Thellier Method

The oldest method of determining intensities is the Thellier method (Thellier, 1938; Thellier and Thellier, 1959). Basis of this method are several assumptions for the measured intensities:
1) For small fields ($\leq$100 μT), the intensity of TRM is proportional to the external field H_e that created it during heating and cooling.
2) The (p)TRM gained during heating from room temperature to Curie temperature in a field is the same as the (p)TRM gained during cooling.
3) The sum of all pTRMs equal the TRM (Thellier, 1938; Thellier and Thellier, 1959).

For the basic principle of an original Thellier experiment it is assumed that the sample's NRM is the TRM_{pal} that was imprinted by a palaeofield H_{pal} with unknown intensity. By heating to and cooling from the Curie temperature in a field H_{lab} with known intensity an artificial TRM_{lab} is imprinted. According to the assumptions above, the following proportionalities are assumed:

$$TRM_{pal} \propto H_{pal} \text{ and } TRM_{lab} \propto H_{lab} \tag{3.11}$$

Under the premise that no chemical or physical alterations have affected the sample's magnetic minerals since the imprinting of TRM_{pal} and during imprinting TRM_{lab} the

intensity of the palaeofield can be calculated by

$$H_{pal} = H_{lab} \frac{TRM_{pal}}{TRM_{lab}} \tag{3.12}$$

This basic principle does not account for the possibility of the samples' NRM not being a single component of TRM. Chemical alterations of minerals during the heating process are also not checked as well. Therefore Thellier and Thellier (1959) proposed incremental heating of several steps below the Curie temperature in order to analyse the behaviour of direction and possible alterations. PSD and MD grains furthermore pose problems, because they do not fully obey the assumptions above, e.g. for PSD/MD grains magnetisation obtained after pTRM demagnetisation being greater than the pTRM acquisition (Riisager and Riisager, 2001) caused by the differences of their blocking and unblocking temperatures.

The incremental steps of the Thellier experiment are still used in modified versions today. In the original version of Thellier and Thellier (1959) the sample is heated and cooled two times in a known H_{lab}, where the specimen is reversed in the second heating step. With vectorial addition and/or subtraction it is possible to retrieve residual NRM and imprinted pTRM. This double-step is repeated for a number of increments from room temperature to the Curie temperature. To check for alterations at high temperatures, a pTRM value is measured in a repetition step at a lower temperature after the sample was already heated to the maximum temperature. If this pTRM value agrees with the previously measured pTRM value, then this was seen as a sign that no alterations had occurred at the high temperature steps.

Coe (1967) altered Thelliers' protocol in that way that he used a heating and cooling step in zero-field and measured the residual NRM, followed by a second heating step in H_{lab} to measure residual NRM + imprinted pTRM, which was retrieved by subtracting the zero-field value from the in-field value. These steps were again repeated for several temperatures up to T_C. He also applied "pTRM-check" repetition steps at a few temperatures for monitoring alteration. To detect anomalies due to effects in MD grains, Riisager and Riisager (2001) introduced a "pTRM tail-check" to Coe's version of the Thellier experiment. This check is done by a third heating step performed after the in-field heating/cooling step. Like heating step 1, this step is heated in zero-field. If a part of the pTRM of this temperature step is carried by MD grains, then it may be blocked at the in-field temperature step and not be unblocked by the new zero-field heating. For a thermally stable specimen, the remanence difference between the two zero-field steps is defined as a "pTRM-tail", imprinted to MD

grains during the in-field step. pTRM checks are defined as positive, if the pTRM-tail represents less than 20 % of the pTRM at the corresponding temperature (Riisager and Riisager, 2001).

In addition, Krása et al. (2003) introduced an additivity check to also detect MD behaviour. Here, an additional demagnetisation step is introduced to check the additivity of two imprinted pTRMs at temperatures T_1 and T_2 (where $T_1 > T_2$). In this step, the specimen is partially demagnetised from room temperature to T_2 and the remaining remanence is determined. The validity of the additivity law is confirmed if the remaining remanence equals the value of pTRM(T_1)-pTRM(T_2). Additivity test failures are caused by MD particles with unblocking temperatures below their respective blocking temperatures. (Schnepp, 1991; Soffel, 1991)

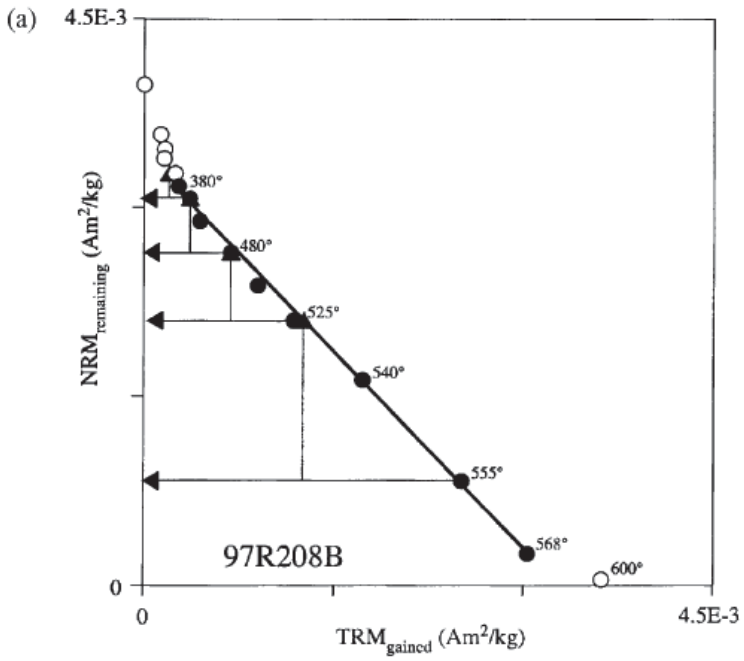

Figure 3.2.: pNRM is plotted versus pTRM in an Arai plot (Arai et al., 1963) from (Riisager and Riisager, 2001). Black dots show linear behaviour and define the slope, horizontal lines show the (very weak) pTRM-tail and vertical lines represent pTRM-checks. Values used for determination of the slope are shown in full symbols, other values in open symbols.

Following Arai et al. (1963) for the analysis of a Thellier experiment, the residual NRM after every temperature step is plotted versus the pTRM that was imprinted by H_{lab} at the

temperature step. According to Thellier's law of additivity, these results show a linear relation between NRM (= $pTRM_{pal}$) and pTRM (= $pTRM_{lab}$) and a straight line as seen in figure 3.2 with a negative slope defined by the data points. Here, secondary components below 380° distort the line while a chemical alteration seems to start above 568°. These points are not considered for the calculation of the slope as only those pTRMs with blocking/unblocking temperatures that are not affected by secondary non-TRM components are used for the palaeointensity estimates. A linear behaviour is also not expected from MD grains which usually result in a concave-up Arai plot due to different contributions of reciprocal and non-reciprocal elements of the magnetisation (Biggin and Poidras, 2006a,b). The slope of the linear line found in a Thellier experiment represents the ratio of TRM_{pal} and TRM_{lab}. With equation 3.12 it can be seen that the product of the absolute value of the slope and the laboratory field H_{lab} equals to the palaeointensity H_{pal}.

3.2.2. The Multispecimen Domain State Corrected Protocol (MSP-DSC)

Despite the vast popularity of the Thellier method, new methods of determining palaeointensities have been developed to avoid the Thellier method's disadvantages:
- It takes a lot of time to heat and cool samples. Due to the large amount of heating steps a Thellier experiment including all kinds of checks is especially time consuming.
- Most rocks are not stable enough to endure the repeated heating steps and chemical alterations are common at high temperatures.
- In strict sense, the Thellier method is only viable for chemically stable SD grains. Chemical alterations, PSD- and MD behaviour can be detected, but not avoided.

Especially due to the last two points, only a fraction of all Thellier experiments is successful which makes the point of time consumption relevant as well. For example, in Hervé et al. (2011), 75 % of measured samples show concave NRM-TRM plots and were rejected.

A better understanding of MD TRM provided by Biggin and Poidras (2006b) enabled Dekkers and Böhnel (2006) to develop a multispecimen method that reduces these disadvantages. This "multispecimen parallel differential pTRM method" (from here on referred to as MSP-DB) is based on the linear relationship between pTRM and the inducing field. This relationship can be applied to all domain states of magnetic minerals as long as there is no alteration during the experiment. To make sure that the magnetic history of all samples

were exactly the same, a multispecimen approach is used. Here, a sample is divided into several sister specimens of which each is used only in one heating step. In this method, a $pTRM_{lab}(T)$ is imprinted parallel to the NRM (assumed to be a full TRM_{pal}) while the specimen is heated to a chosen temperature and cooled back to room temperature in a laboratory field H_{lab}. If the resulting remanence is larger than the initial NRM, then H_{lab} has been larger than H_{pal}. If the resulting remanence is smaller than the NRM, then H_{lab} must have been smaller than H_{pal} and if the resulting remanence is equal to the NRM, then $H_{lab} = H_{pal}$. With statistical methods and several samples with different H_{lab} imprinted at the same temperatures, H_{pal} can be determined. The parallel imprint of the $pTRM_{lab}(T)$ also removes possible biases due to pTRM tails. The biggest advantage of this method is the possibility to freely chose the heating temperature. With this, the temperature can be chosen so low, that alterations in the specimens can be avoided. However, this method requires the different sister-specimens to be very homogeneous and seems to overestimate palaeointensities for PSD and MD grains especially with respect to the unblocking behaviour. (Dekkers and Böhnel, 2006; Fabian and Leonhardt, 2010)

After the development of the MSP-DB method, Fabian and Leonhardt (2010) tested it with very well characterized synthetic samples with different domain-states, proposed improvements for the method and introduced their "domain-state corrected multiple-specimen palaeointensity determination technique" (MSP-DSC). These improvements were meant to deal with finding an ideal temperature to avoid alterations, identify VRM fractions, quantify domain states, the used NRM fraction, domain state dependent overestimates as well as thermal stability. Finally it provides a more sophisticated statistical evaluation of the measurement and its uncertainty interval. Nevertheless, four heating steps are required for each specimen.

In contrast to Thellier experiments, only one heating temperature is used, where $T < T_C$. The method features five measurement steps, where the first two resemble the MSP-DB steps while the other three are used to estimate NRM fraction, domain state and alteration as well as to quantify validity parameters. The measurement steps in order are:

1) Measurement of initial NRM ($= TRM_{Pal}$) $\vec{m}_0$
2) Heating to and cooling from temperature T in field H_{lab} which is aligned parallel to the NRM, resulting in the measured remanence $\vec{m}_1$
3) Heating to and cooling from temperature T in field H_{lab} which is aligned antiparallel to the NRM, resulting in measured remanence $\vec{m}_2$

4) Heating to temperature T in zero-field and cooling from temperature T in field H_{lab} which is aligned parallel to the NRM, resulting in the measured remanence $\vec{m}_3$
5) Repetition of step 2), resulting in remanence $\vec{m}_4$

As stated above, measurements of the remanences $\vec{m}_0$ and $\vec{m}_1$ resemble the measurements of MSP-DB. $\vec{m}_2$ is used for a normalization to the NRM fraction in order to correct the scatter and slope of the multispecimen plot by adding it to $\vec{m}_1$ to get the residual remanence, i.e. the fraction of NRM, which is replaced by the laboratory TRM. Fabian and Leonhardt (2010) also showed, that the comparison of the remanences $\vec{m}_3$ and $\vec{m}_1$ can be used to estimate the domain-state bias of the overprinted TRM. The measurement of $\vec{m}_4$ is used to estimate alteration by calculating the ratio

$$\delta_{alt} = (\vec{m}_1 - \vec{m}_4)/\vec{m}_1. \tag{3.13}$$

To get the domain state, the relative pTRM-tail size is compared to the pTRM:

$$\mu_{DS} = \frac{\vec{m}_1 - \vec{m}_3}{\vec{m}_3 - \frac{1}{2}(\vec{m}_1 + \vec{m}_2)} \tag{3.14}$$

This ratio gives values close to zero for SD particles, while the results for MD particles can be higher than 20% (Fabian and Leonhardt, 2010). This is explained in a phenomenological model that is based on the difference between blocking and unblocking remanences and used to visualize complex thermal cycles in investigations (Fabian, 2001). In this model, a magnetic sample is represented by a collection of independent magnetisation elements with a distinct blocking temperature T_B and unblocking temperature T_{UB}. The sample is characterized with respect to thermal magnetisation processes via the function $\varkappa(T_B,T_{UB})$ which describes the quantity of magnetisation elements. All magnetisation elements gain a remanence $\varkappa(T_B,T_{UB})\vec{H}$ when they are cooled below T_B in an external field $\vec{H}$ and are demagnetised when they are heated above T_{UB} (Fabian and Leonhardt, 2010).

A phenomenological vizualisation of the MSP-DSC method is shown in figure 3.3-A). Here, the diagrams a) to e) visualize the five measurement steps and how the relevant areas representing magnetisation, shown in figure 3.3-B), are affected. Diagram α) is the result of calculating $(\vec{m}_0 - \vec{m}_1)/2$ from a) and b), which represents the original MSP-DB method. The result of calculating $(\vec{m}_1 + \vec{m}_2)/2$, which enables the determination of the NRM fraction for the fraction correction shown in β). The domain state effect, as difference between step 2, heated and cooled in-field, and 4, heated in zero-field and cooled in-field, and calculated by $(\vec{m}_1 - \vec{m}_3)$ is visualised in γ. The subtracion of $\vec{m}_1$ from $\vec{m}_4$ to determine

thermal stability is not shown in the figure. Deviations of the result of $(\vec{m}_1 - \vec{m}_4)$ from zero can origin from measurement uncertainties or alterations.

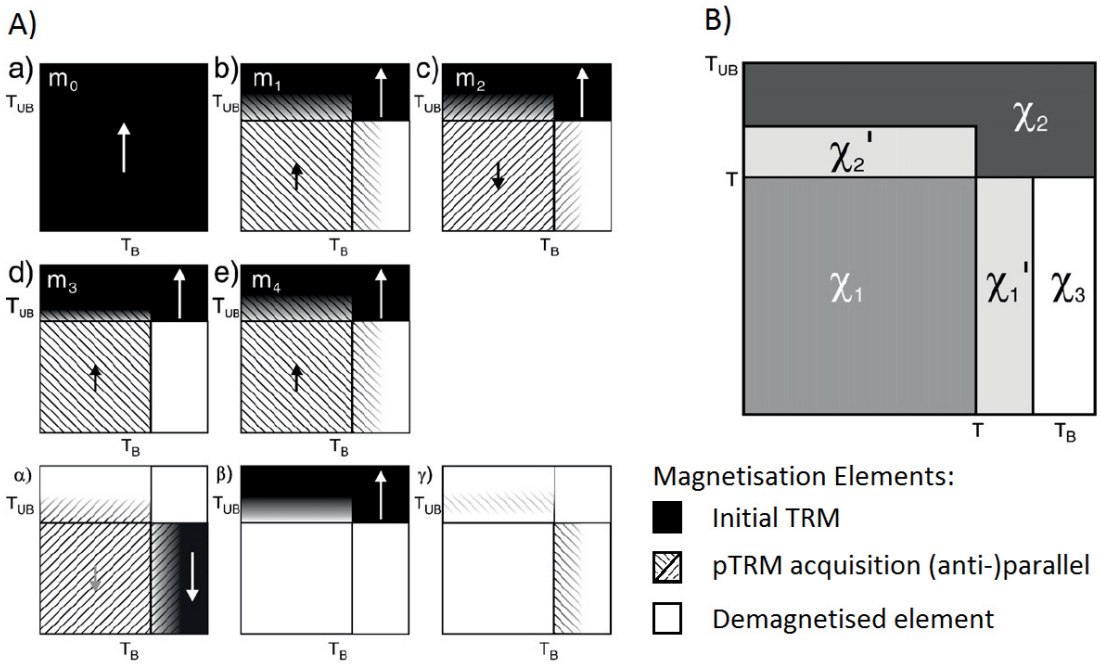

Figure 3.3.: A) Phenomenological visualisation of the MSP-DSC method. B) Visualisation of the relevant areas for the MSP-DSC experiment. (Fabian and Leonhardt, 2010). For further explanation see text.

A simplified representation of the relevant integral susceptibilities of TRM imprints is shown in figure 3.3-B) and the resulting remanences of the measurement steps $\vec{m}_i$ can be described with the integral susceptibilities and the laboratory field. For the initial TRM of a sample $(\vec{m}_0)$ is

$$\vec{m}_0 = \varkappa_2 H + \varkappa_1 H + \varkappa_2' H + \varkappa_1' H + \varkappa_3 H \tag{3.15}$$

With the measured remanences and the representation as susceptibilities and field, an upper estimate of the palaeofield's intensity H_{max} can be calculated with

$$H_{max} = \frac{2\vec{m}_0 - \vec{m}_1 - \vec{m}_2}{\vec{m}_1 - \vec{m}_2} H_{lab} = (1 + \frac{\varkappa_3}{\varkappa_1 + \varkappa_1' + \varkappa_2'})H. \tag{3.16}$$

With the phenomenological model, Fabian and Leonhardt (2010) show that H_{max} always overestimates H_{pal} if $\varkappa_3$ is > 0, which is common for samples that contain PSD or

MD particles. With the proportionality of $\varkappa_3$ and $\varkappa_1'$ and the resulting ratio of ($\vec{m}_1$-$\vec{m}_3$)/H_{lab}=$\varkappa_1'+\frac{1}{2}\varkappa_2'$, Fabian and Leonhardt (2010) introduce a fraction α, for which

$$\varkappa_3 = \alpha \frac{\vec{m}_1 - \vec{m}_3}{H_{lab}} \tag{3.17}$$

and their experiments suggest α values between 0.2 and 0.8. With this fraction α, it is possible to calculate a domain-state corrected estimated palaeointensity with

$$H_{est} = \frac{2\vec{m}_0 - \vec{m}_1 - \vec{m}_2}{(1+2\alpha)\vec{m}_1 - 2\alpha\vec{m}_3 - \vec{m}_2} H_{lab} \tag{3.18}$$

The results are presented in plots as seen in figure 3.4, where the ratio Q of pTRM and initial NRM are plotted against H_{lab}. The intersection of the regression line of the plot-points and the zero-level of Q gives the value for H_{pal}. In figure 3.4 a), the MSP-DB ratios, calculated with

$$Q_{DB} = \frac{\vec{m}_1 - \vec{m}_0}{\vec{m}_0} \tag{3.19}$$

are plotted. A free line fitted to the data provides H_{pal}. The fraction-corrected ratios Q_{FC} are obtained by correcting the pTRM fraction f by using $\vec{m}_2$ from the measurement step with reversed field:

$$Q_{FC} = 2\frac{\vec{m}_1 - \vec{m}_0}{2\vec{m}_0 - \vec{m}_1 - \vec{m}_2}, \tag{3.20}$$

represented in figure 3.4 b). Implementing equation 3.17, one gains the equation to calculate the domain-state corrected ratio Q_{DSC} with

$$Q_{DSC} = 2\frac{(1+\alpha)\vec{m}_1 - \vec{m}_0 - \alpha\vec{m}_3}{2\vec{m}_0 - \vec{m}_1 - \vec{m}_2}. \tag{3.21}$$

Q_{DSC} versus field is shown in the lower plots in figure 3.4 c). Q_{DSC} values can be used to improve the field calculation as well as quantify the domain-state effect in the MSP plot by combining them with the Q_{FC} results. (Fabian and Leonhardt, 2010)

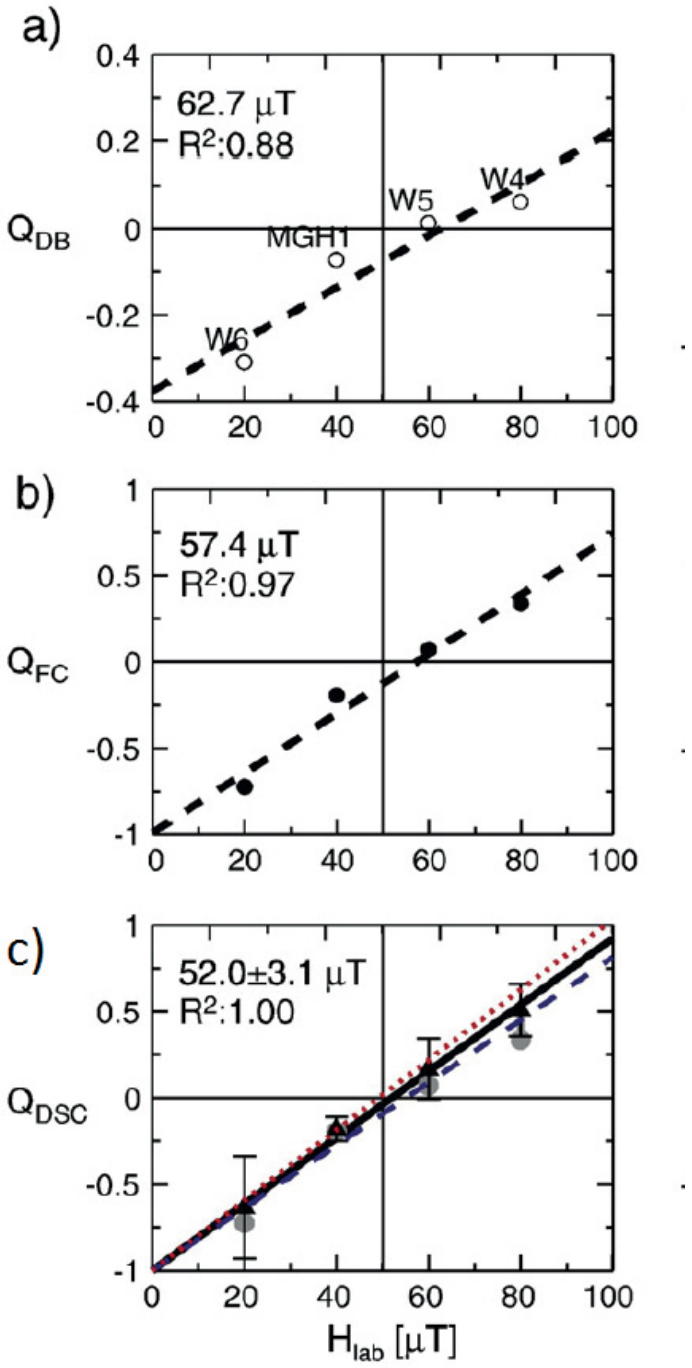

Figure 3.4.: Resulting plots of the multispecimen protocol method for a synthetic sample series. The different ratios of Q of pTRM and initial NRM are plotted against the H_{Lab} (see text). The black solid line in c) represents a domain-state correction using α=0.5, the blue dashed and the red dotted lines represent corrections with α=0.2 and α=0.8 respectively. Modified from (Fabian and Leonhardt, 2010).

4. Site Descriptions and Sample Preparation

4.1. Semlach/Eisner

Archaeological Context

The site Semlach/Eisner is located in the southwest of Semlach (Hüttenberg) in the north-south aligned Görtschitztal in Carinthia (46.928 °N, 14.557 °E). Hüttenberg, located in the former Celtic kingdom *Noricum*, was integrated into the Roman empire in 15 BC (Dobesch, 1983). The historical significance of Hüttenberg results from its iron ore deposits that were mined until 1978. Due to the discoveries of several Roman iron smelting furnaces and mining tools since the late nineteenth century the area has been suspected to have been the centre of the production of *Ferrum Noricum*, the famous Noric steel mentioned in numerous Greek and Latin literary sources since the Late Iron Age (Cech, 2014).

While remains of roman settlements in the area around Hüttenberg have been found since the late 19^{th} century, the archaeological investigation of the iron production facilities at Hüttenberg itself started in the year 2003 and continued at the site Semlach/Eisner until 2010 (Cech, 2014). The exact excavation site was located by interviewing locals and geophysical surveys before and during excavations, which, using geomagnetic, geoelectric and electromagnetic methods were conducted in and around the site. Such an integrated geophysical survey was used to delimit the historical industrial area and identify masonry foundations, smithing hearths and smelting furnaces as well as slag deposits (Walach et al., 2011; Stückler, 2010). The conducted excavations of the site unearthed the features seen in figure 4.1. The excavated features comprise of several Roman walls, a cistern, beam slot constrictions, ore roasting pits, 6 bloomery furnaces and 12 smithing hearths, and can be

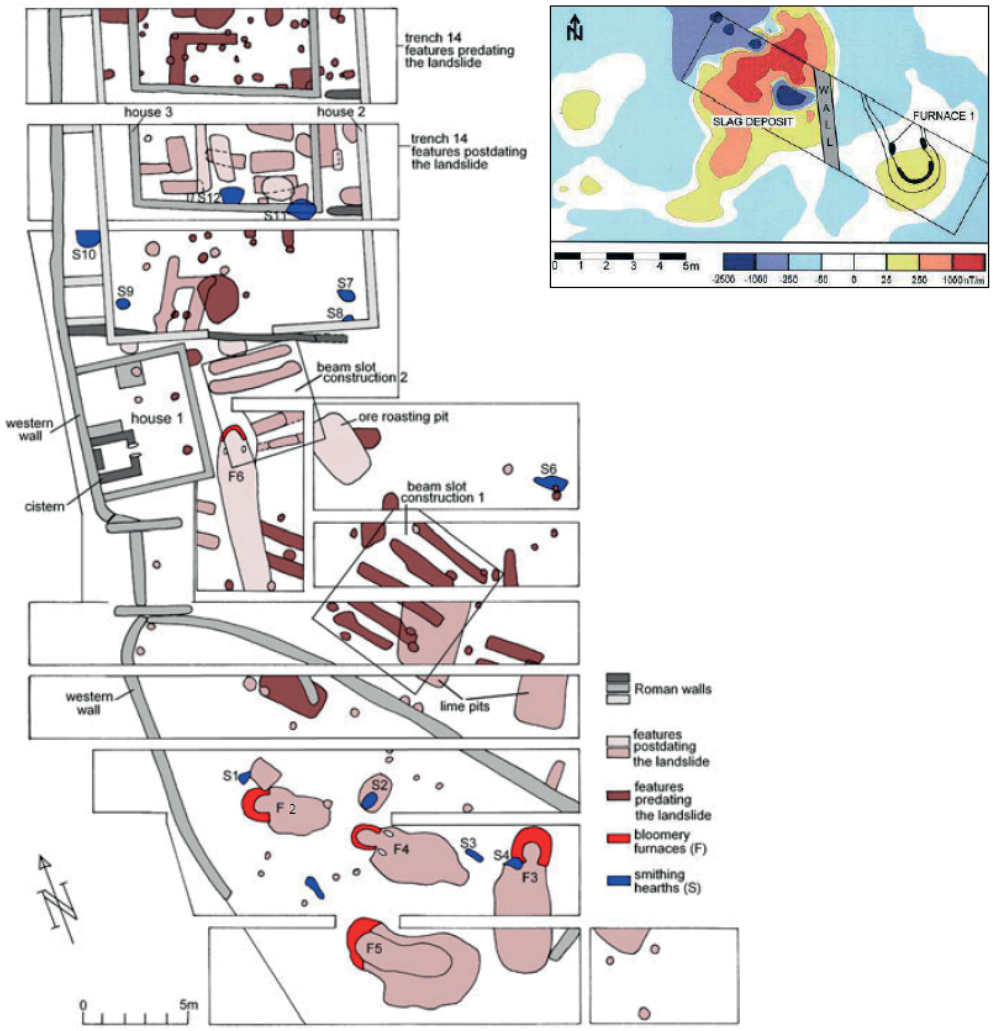

Figure 4.1.: Excavation plan of the Semlach/Eisner site. Trench S3, seen in the isanomalic map with furnace 1 visible is located north of the shown area of the excavation plan. (Cech, 2014; Walach et al., 2011)

divided into several chronological phases. The earliest features, postholes and beam slot construction 1, date back to the early 1^{st} century AD. A landslide at the transition of the 1^{st} to the 2^{nd} century lead to a reorganisation of the site. In the following time period new furnaces were build and older ones abandoned while the wooden structures were replaced by houses with stone foundations and mortar floors. The latest Roman feature seems to be furnace 1 that was dated to the 1^{st} half of the 4^{th} century. The site was levelled in the 12^{th}-13^{th} century and used as farmland from this point onwards (Cech, 2014).

Samples

In the years of 2004 and 2005 the furnaces 1 to 5, (figure 4.1) were sampled and their archaeomagnetic results were published in 2008 (Schnepp, 2008; Gruber and Schnepp, 2008). In the years from 2006 to 2009 another set of samples has been taken from the site. For this set, furnace 6, a roasting pit and four smithing hearths were sampled. Depending on the sampled materials, different methods, as described in Schnepp et al. (2008), were used for the sampling. Samples from unconsolidated material were taken as soft cores, spread over the oven surface as seen in figure 4.2, while samples from harder material were taken in form of blocks. All samples were oriented with a magnetic compass and an inclinometer.

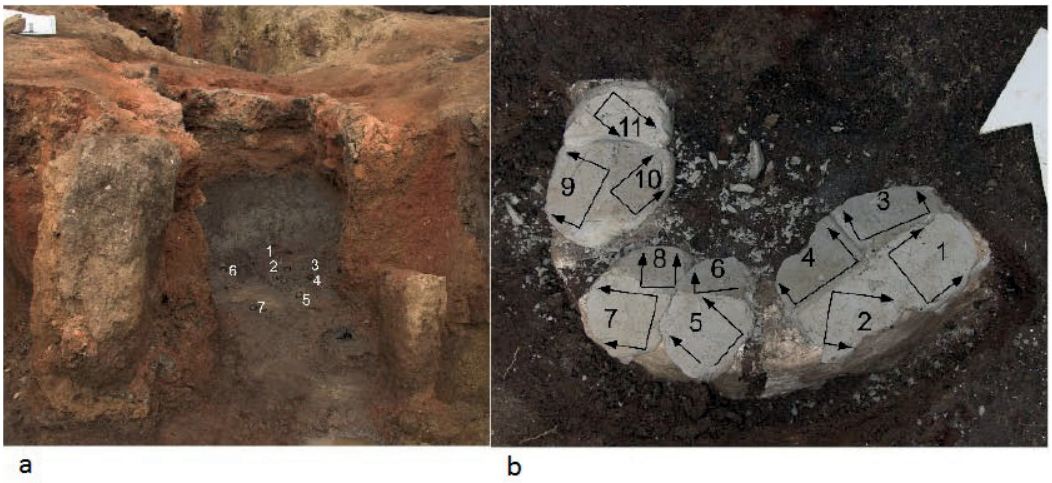

Figure 4.2.: a: Spatial dispersion of taken soft cores in oven F4; b: Example of block sampling method at hearth 10 (Schnepp, 2016).

The specimen used in this thesis come from three furnaces. The samples were blocks of the furnace walls or the furnace cupolas that had fallen down into the furnaces. Therefore, the blocks were collected as unoriented samples and kindly provided by the archaeologist (B. Cech) to be used for intensity determination and dating in combination with the data of the direction of the paleofield of the associated furnaces as published in Schnepp (2016). The furnaces are seen as F4 and F6 in figure 4.1, while furnace 1 was found North of this area and is shown in the isanomalic map in figure 4.1. Furnace 1 (samples labelled with (SE1) was dated to the mid 4^{th} century, F4 (SE4) was dated to the second half of the 2^{nd} century and F6 (SE6) to the second half of the 1^{st} century (see table 4.1) (Cech, 2008; Schnepp, 2016).

Figure 4.2b shows an example of a block taken from hearth 10 to show how plaster was applied to the samples for orientation purposes. Here, several planar surfaces were made with the help of acrylic glass plates and plaster on the block's surface to obtain several individually oriented samples from the block (Schnepp, 2016).

4.2. Thunau am Kamp

Archaeological context

The archaeological site of Thunau am Kamp (48.59°N, 15.65°E) is located in the north-western area of Lower Austria, about 35 km north of "Krems an der Donau". Although there is evidence of occupation of the area since the Late Neolithic, the main focus of the archaeological investigations lies on the Early Medieval time period. The site can be divided into two main parts, a valley settlement with a burial ground and a fortification on an adjacent hill. The relevant part for this thesis, the settlement, is located between the hills of "Schanzenberg" and its hillfort in the west and "Goldberg" in the north as well as a former meander bend of the river Kamp in the south (Szameit, 2015). At the end of the 10^{th} century, the burial ground was used on the southern slope of "Goldberg" as the first of three parts of the settlement (Friesinger and Friesinger, 1975). The other two parts consist of a residential and a production area, found south of the burial ground on an alluvial terrace of river Kamp in 1975 (Friesinger, 1976). Excavations have proven, that the production area was mainly used for textile and lumber industry as well as local pottery production. As there was not enough space for agriculture, the food production was sourced out to the hinterland. Merely flour and bread production was proven by the excavations of several mill stones (Obenaus, 2015).

Up to the year 2015, 25 pit houses of the residential area have been excavated by Obenaus (2015). They are divided into two chronological relevant phases from the 9^{th} to the beginning of the 11^{th} century. The houses belonging to the older phase contain almost no finds but they are characterised by their quadratic base areas and an oven with a cupola in one of the corners. These ovens are usually made out of stone, loam or mixtures of both materials. In contrast, the houses of the younger phase, which is dated to the 10^{th} century, have longer rectangular base areas. The ovens of these houses are also completely different from the ones of the older phase. Instead of being situated in a corner inside the house, there are

now one or two cupola ovens dug into the in-situ loam at the flanks of the houses. These houses also contain numerous finds like mill stones, loom weights and pottery. The end of this younger phase also marks the beginning of the discontinuation phase of the settlement (Obenaus, 2015). The distinction of the phases of the settlement was also supported by archaeomagnetic data from oven samples taken between 2009 and 2013 (Schnepp et al., 2015).

Samples

In September 2014, three ovens have been sampled at the site of the valley settlement. The sampled ovens can be seen in figure 4.3, labelled as THX (SE2810), THY (SE2861) and THZ (SE2941). The two ovens THY and THZ can be linked to a working area and THZ was located in the corner of the area whereas THY is an oven of the younger type in one flank of it. The oven THX was located in the flank of a pit house of the younger phase, which was build in superposition of the working area containing THY and THZ. Considering the combination of the different types of the ovens as well as the arrangement of pit house and working area, a stratigraphy is obvious which defines an age sequence from THZ as oldest to THX as youngest and THY in between. These three ovens were all sampled with the techniques from Schnepp et al. (2008). Furthermore, samples from the features THP, THT and THU, sampled and measured by Schnepp (2017), were used in this thesis for intensity measurements. In addition to the samples from the various ovens, ceramic shards found in ovens TH2, TH5, TH8 and TH9 were kindly provided by the archaeologist (M. Obenaus) for measurements.

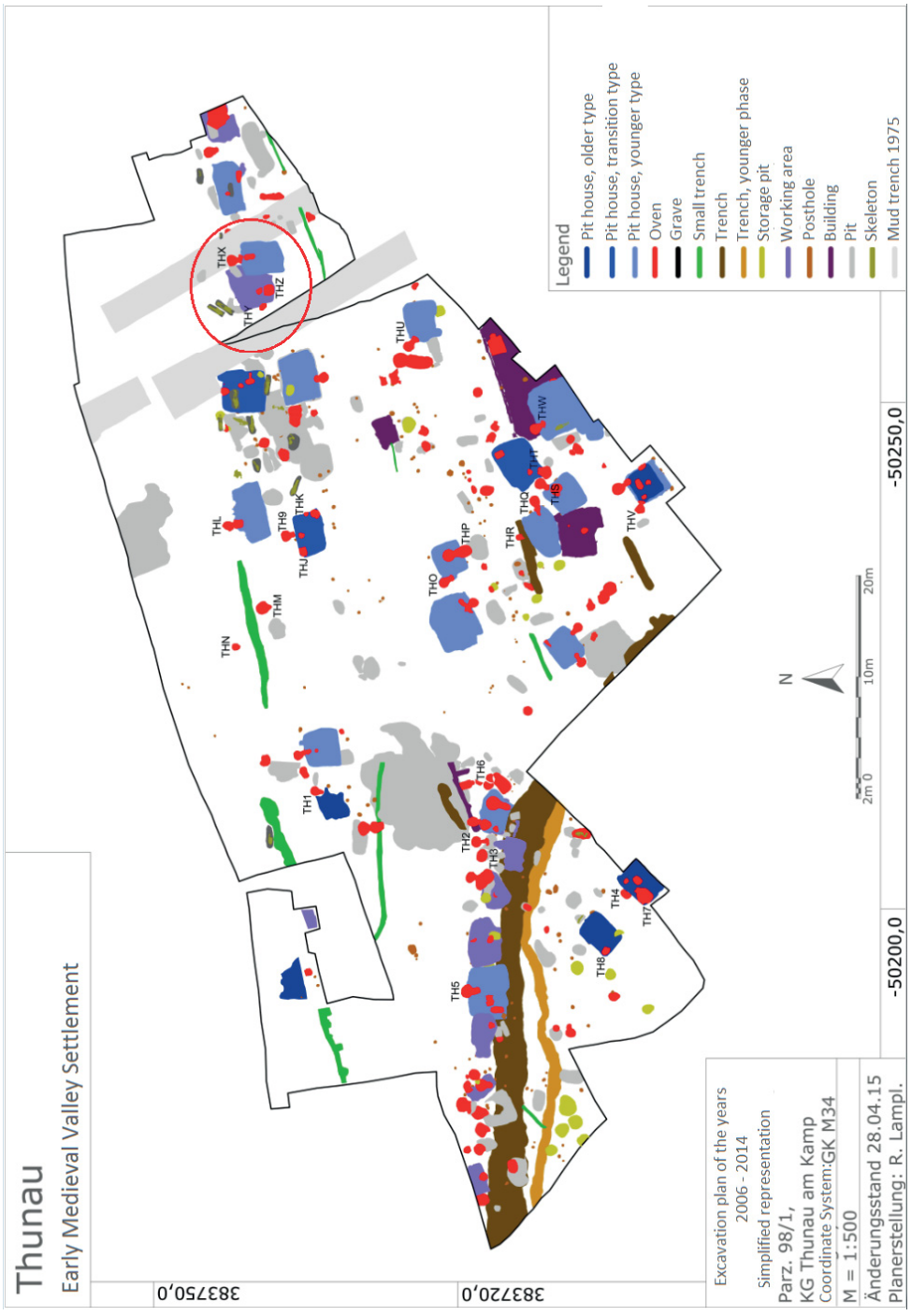

Figure 4.3.: Excavation plan of the site Thunau am Kamp. Sampled furnaces can be found inside the red circle. Modified from (Obenaus, 2015).

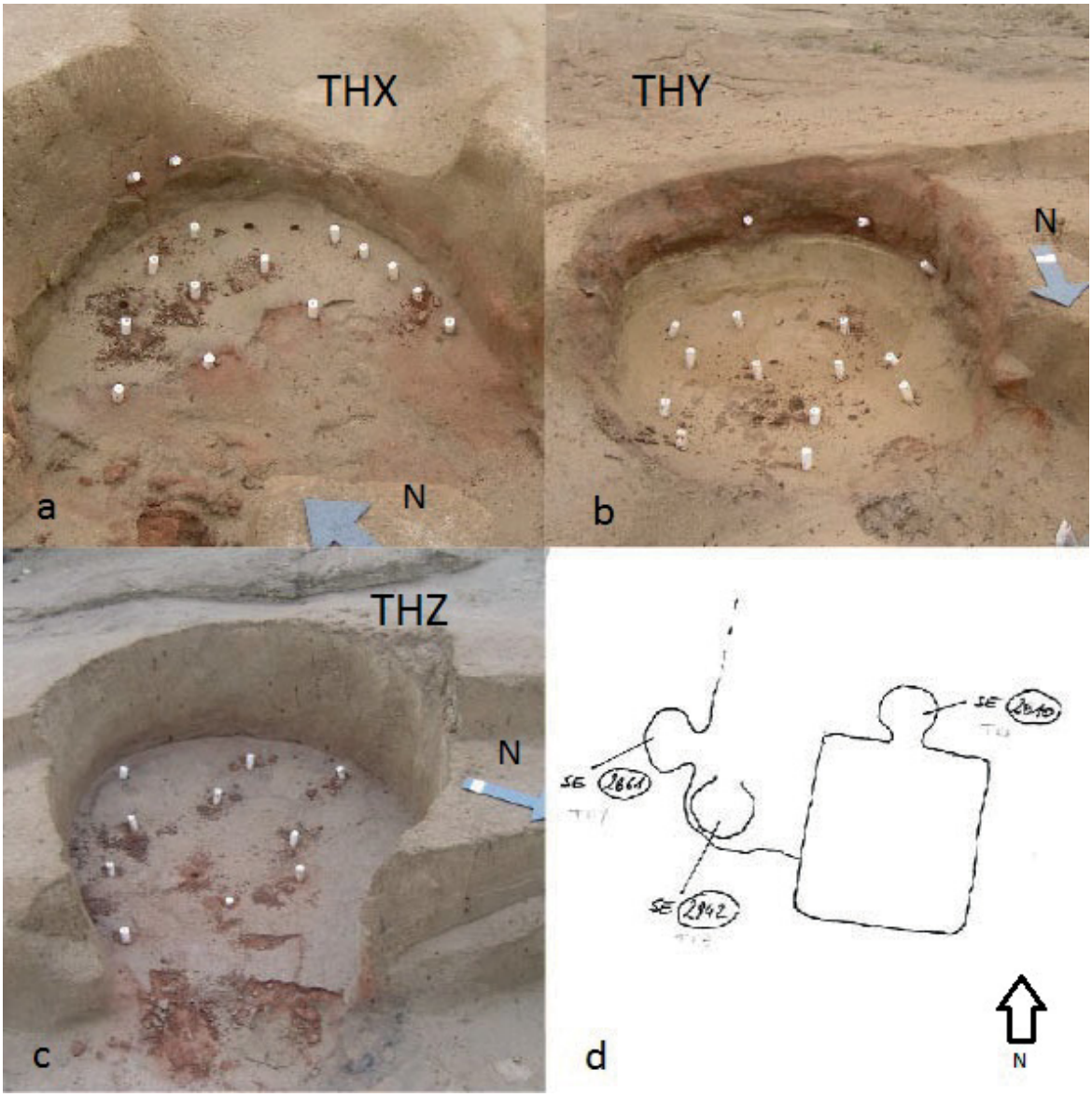

Figure 4.4.: Spatial distribution of soft cores in ovens THX (a), THY (b) and THZ (c). The reddish parts are the baked loam parts of the oven which are covered by a thin colluvial loam layer d) shows the arrangement of the three ovens

The floor of oven THX consists of reddish, slightly baked loam close to the surface and brown to grey loam in the deeper area. While most of the oven seemed to be intact, as seen in figure 4.4 a, there are areas at the front of the oven (front part in figure 4.4 c) showing cracked parts of the oven floor. Due to heavy rains in the days before the sampling, all of the ovens are covered by a 1 - 2 mm thick colluvial layer of loam, carried into the

oven from the vicinity by water. Oven THX was sampled by 15 soft cores, distributed over the baked bottom area. Unoriented block samples for intensity measurements were taken from the cracked parts of the oven floor.

Similar to THX, the oven THZ also consists of a layer of reddish baked but softer loam. THZ was completely undisturbed and was also sampled by 15 soft cores. 12 of these soft cores were taken from the bottom of the oven. As the lower parts of the oven walls were baked as well, three soft cores were also taken from the southern oven wall. No block samples were taken from this oven because of the small thickness of the layer of baked clay.

In many parts of the oven THY, the uppermost layer of the baked loam was consolidated to a hard plate. Three unoriented block samples were removed of this plate from the eastern part of the oven. The remaining area of the oven was sampled by 10 soft cores. A more extensive sampling of this oven was not possible because heavy rain progressively rendered the site unaccessible and the sampling had to be stopped.

Each of the soft cores was oriented by a magnetic compass and an inclinometer. The use of a sun compass for orientation was prevented by inopportune weather conditions.

The ceramic shards from the corpus of finds are fragments of ceramic pots of different sizes. They were named after the ovens in which they had been found. The shards of TH5 are made of a supposedly homogeneous black material and show wave mouldings which are either carved or cord imprints (Kern and Grömer, 2015). TH8 and TH9 also show similar ornamentations. However, their material is lighter than TH5's material. The colors range from dark grey to light brown-red. According to archaeologist Martin Obenaus, the shards originated all from Thunau or its vicinity, due to the used clay being from deposits in the radius of 15 - 20 km around Thunau. The markings on the ceramics are typical for the Slavic culture of the Early Middle Ages (Cech, 1991).

4.3. Preparation of Specimens

After the sampling, the soft cores and the block samples were dried for several days outside in a covered area. As soon as the samples were dry, they were dipped into and sprinkled by SILRES BS OH 100, a solventless product for the consolidation of building materials.

Figure 4.5.: Examples of ceramic shards of TH8 (a) and TH5 (b) on plaster bases before cutting.

The solution is based on ethyl silicate. With help of the capillary forces it penetrates the material. There it reacts, promoted by a catalyst, with water from air humidity and forms a glass-like silica gel binder while the by product ethanol evaporates. As the final hardness of the samples is only reached after two weeks, the samples were again dried for this amount of time.

Before the soft cores could be taken out of the plastic tubes, in which they had been transported, orientation marks were applied to the samples with a water resistant marker. For every soft core an arrow pointing in direction of the sample's X axis, as well as a second arrow, parallel to the dip direction of the cores are marked. Here, the arrows point in the direction of the dip. In the following step, the cores were taken out of the plastic tubes and trimmed by a buzzsaw with a non magnetic saw blade to lengths of 22 mm specimens (1-3 per sample). The prepared samples are then circular cylinders with a volume of approximately 10 cm^3.

To achieve a sufficient amount of samples from the block samples, they were trimmed according to size of the blocks. Large blocks were cut into cubes with 20 mm edge lengths while the smaller blocks were cut into cubes with 13 mm edge lengths. The oriented samples were cut with reference to the planar surface of the plaster as well as the marked X-axis.

The orientation markings were applied after the respective saw cuts so that every cube was marked with a X-axis arrow and the specimen name in the end.

Site	Feature	Age (year AD)	N (orient./unorient.)	n (orient./unorient.)
SE1	Furnace 1	300-350	0/5	0/47
SE4	Furnace 4	<200	0/5	0/44
SE6	Furnace 6	50-100	0/6	0/52
TH2	ceramic shards (SE612)	950-1000	0/2	0/6
TH5	ceramic shards (SE526)	950-1000	0/5	0/34
TH8	ceramic shards (SE847)	800-1000	0/7	0/55
TH9	ceramic shards (SE945)	900-1000	0/5	0/28
THP	Oven (SE2305)	850-950	0/2	0/13
THT	Oven (SE2349)	850-950	0/7	0/38
THU	Oven (SE2388)	900-1000	0/4	0/51
THX	Oven (SE2010)	850-950	15/3	43/16
THY	Oven (SE2861)	850-950	10/5	20/26
THZ	Oven (SE2942)	850-950	15/0	36/0

Table 4.1.: List of investigated features/ find collections: Site name; sampled feature; archaeological age (AD); N: number of statistically independent samples, oriented/unoriented; n: number of specimen, oriented/unoriented.

As the fragments of the ceramic jars had no planar surfaces that could have been used as reference surfaces, new planar reference surfaces were created by embedding the shards into plaster. The orientation lines were chosen randomly and applied to the shards. Following this, the shards were trimmed to squares with side lengths of 13 mm. To achieve a cubic form for the thinner shards, the shards were cast in plaster to a height of 13 mm.

The same procedure as for the shards was used for the unoriented sample blocks of Semlach as well. As there was plenty of sample material available for these samples, the samples of Semlach were cut into cubic specimens of 20 mm edge length. The prepared specimens were then covered with non magnetic aluminium cement so that they would not crumble at higher temperatures of heating. All the markings on the specimens were again applied with a pencil that does not fade at high temperatures as the permanent marker would. A list of specimens is presented in table 4.1. These preparations were conducted partly at University of Leoben and the Leibnitz Institute of for Applied Geophysics.

5. Rock Magnetic Measurements

All measurements have been carried out in the palaeomagnetic laboratory Gams of University of Leoben's chair of applied geophysics.

5.1. Mass, Bulk Susceptibility and NRM

As a first step, mass and bulk susceptibility of all specimen were measured. The masses were measured with a laboratory scale with a precision of 10^{-2}g while the bulk susceptibilities were measured with a Geofyzika minikappa bridge with a measurement range from 10^{-6} to 10^{-3}. As a second step for the archaeomagnetic evaluation, the natural remanent magnetisation was measured, using a 2G-Kryogenic magnetometer with a measurement range between 10^{-6} and 10^{3} A/m. During the measurements, the specimens were shielded from Earth's magnetic field passively by a μ-metal casing and actively by a Helmholtz-cage, consisting of three pairs of coils that generate a field, to compensate Earth's magnetic field. Remanences are measured with three SQUID (Superconducting QUantum Interference Device) systems in four measurement positions that cover all three Cartesian directions.

The distribution of measured and field corrected NRM directions for ovens THX, THY and THZ is shown in figure 5.1. While THX and THY show a relatively low scatter, there are several directions at the plot of THZ far away from the area in which most of the directions are concentrated. Also shown in figure 5.1 are plots of NRM versus bulk susceptibility together with lines of increasing Koenigsberger ratio Q = NRM/$\varkappa$/40 Am^{-1} in logarithmic intervals of 0.1, 1, 10 and 100. The values of all sites are distributed between Q values of 0.5 and 10. The low to medium ratios ($<$5) indicate, that the specimens may not have been imprinted with a complete TRM, but only with a pTRM during the last baking (Schnepp et al., 2004). This is in agreement with the optical colour scale of the sampled cores. They showed the typical reddish color of baked clay only on the first few centimetres below the

oven floors. The lower Q values of THX and THZ account for the higher scatter of the NRM directions compared to THY. The Koenigsberger ratios for the shards of Thunau can be seen in figure 5.2a). The Q values of the ceramic shards of TH5 and TH9 show high values in the area of 7 to 50 and indicate that the shards were well baked. No significant difference can be seen between the reddish shards and the black shards containing graphite. Both TH2 and TH8 shards show lower Q ratios and plot in the vicinity of Q = 5. Similar

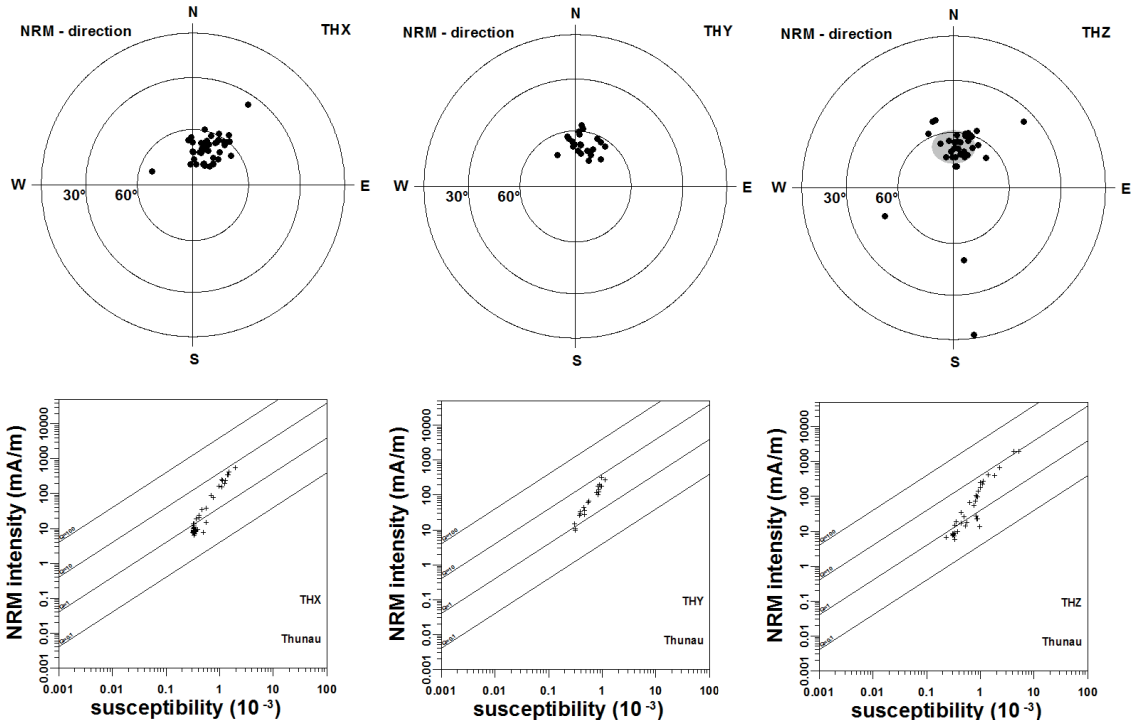

Figure 5.1.: Upper row: plots of NRM directions of sites THX, THY and THZ in stereographic projection; Lower row: plots of NRM versus bulk susceptibility with lines of constant Koenigsberger ratios between 0.1 and 100.

to the ovens THX, THY and THZ, the other ovens of Thunau, THP, THT and THU show Q values between 1 and 10 (5.2b)). The Koenigsberger ratios of the furnaces of Semlach are also shown in figure 5.2b). In contrast to the ovens of Thunau, the well baked material of all three Semlach furnaces shows high Q values that plot mostly between 10 and 100.

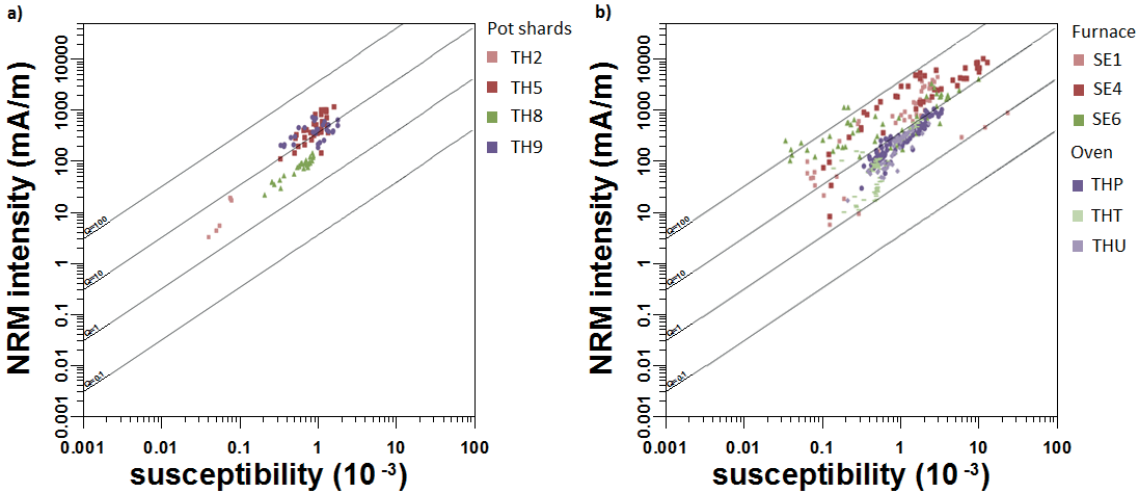

Figure 5.2.: Plots of NRM versus bulk susceptibility with lines of constant Koenigsberger ratios between 0.1 and 100 for a) Thunau ceramic shards TH2, TH5, TH8, TH9 and b) Semlach furnaces SE1, SE4, SE6 and Thunau ovens THP, THT and THU.

5.2. Temperature Dependent Susceptibility

An AGICO MFK-1A multifunction Kappabridge with a sensitivity of $5{\cdot}10^{-8}$ was used to measure the bulk susceptibility as function of (high) temperatures. Pieces of the samples of about 0.2 to 0.4 g were crushed and used for two types of thermal cycles. There were no criteria for the selection of the material for the specimen. The first thermal cycle determined the susceptibility during heating followed by cooling between 40 °C and 700 °C. In order to better determine the temperatures, where alterations in the minerals start, measurements with incremental steps of heating and cooling to an increasing maximum temperature were also executed for a second sister specimen. These steps were:

Step	T_{min} (°C)	T_{max} (°C)
I	60	250
II	60	350
III	60	450
IV	60	550
V	40	700

With these measurements, the susceptibilities as function of temperature were measured for specimens of all sites to find a suited temperature range for the palaeointensity experiments.

In general, the measured susceptibility curves can roughly be divided into four types as shown in figures 5.3 a) to d). However, for most features not all specimens showed curves of the same type, suggesting that the material of the sites is not homogeneous from a rock magnetic point of view.

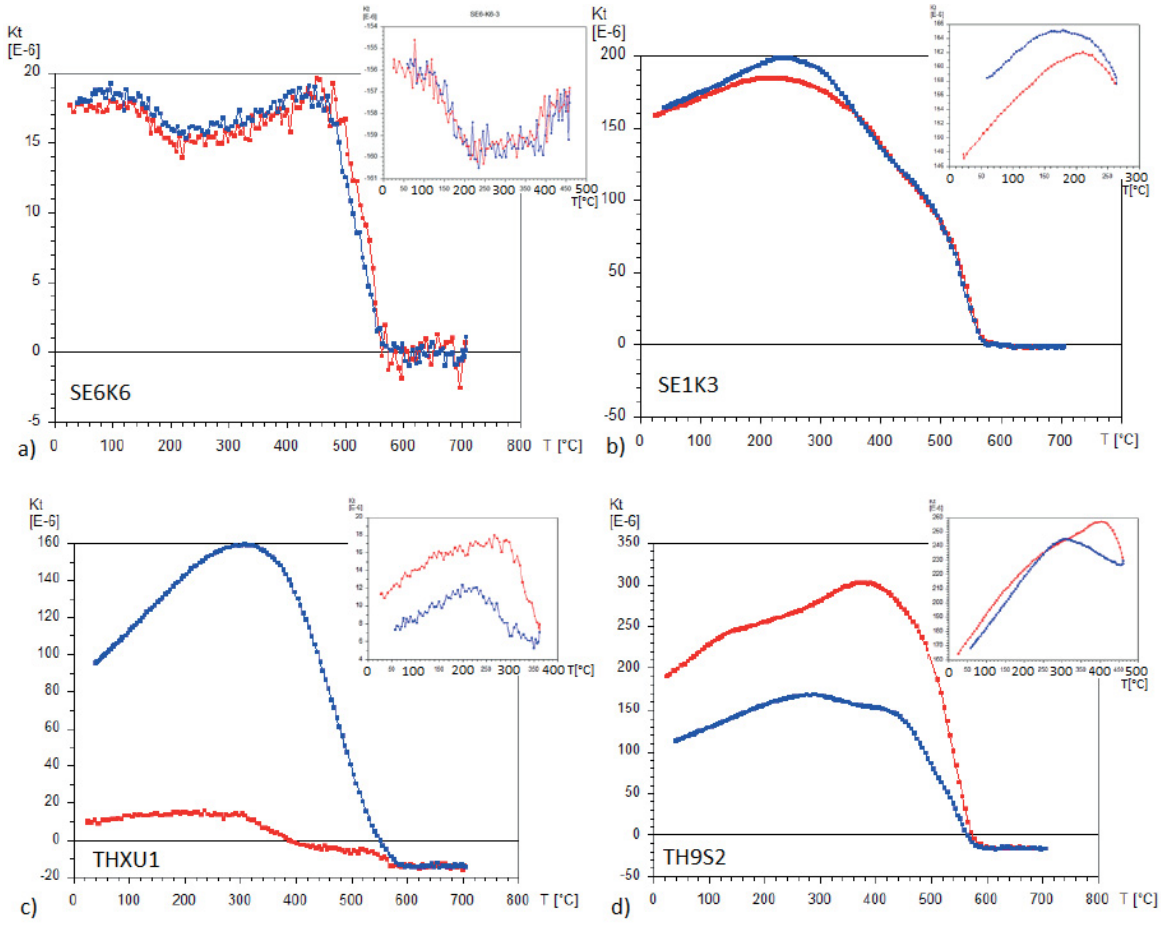

Figure 5.3.: Types of susceptibilities as function of temperature. Heating cycle is shown in red, cooling cycle in blue. a) Completely reversible; b)-d) High temperature measurement and lower temperature step, showing irreversible behaviour due to alterations.

Specimens with almost reversible susceptibilities in the temperature range between 40 °C and 700 °C (fig. 5.3 a) were mainly found in the material of furnaces of Semlach but also for oven THT. The type of curve seen in figure 5.3 b) was also measured for furnaces and ovens of Semlach and Thunau (THT and THP and THU), but also for some ceramic shards of TH5. These curves are almost reversible. However, a closer look at the lower temperature steps of the step measurements reveal obvious alterations starting already at

temperatures of less than 250 °C.

Completely different behaviour of susceptibilities is shown in figure 5.3 c) and d) where the susceptibility at the cooling cycle is either significantly higher (c) or lower (d) than in the heating cycle. Curves of type (c) were measured for the ovens THX and THY while for most of the ceramic shards either type (c) or (b) occurred. The curve in the upper right corner of figure 5.3c) shows a maximum of susceptibility at a temperature of 200 °C and irreversible behaviour due to alteration. In contrast to the high temperature measurement, the susceptibility of the cooling cycle is here smaller than the susceptibility of the heating cycle. A different behaviour can be seen in figure 5.3d), where the susceptibility increases after step heating. The step measurement in the upper right corner of figure 5.3d) shows inflection points at 200 °C and 400 °C and irreversible behaviour after the heating step. Overall, the Curie temperatures were measured in the vicinity of 560 °C to 600 °C. These measurements are the basis for the choice of temperature in the intensity experiments where the heating temperatures should not reach any alteration temperature.

5.3. Anhysteretic Remanent Magnetisation (ARM)

As described in section 3.2.2, it is necessary to be able to apply a laboratory field (anti)parallel to the specimen's NRM, which could deviate from the direction of the ancient geomagnetic field direction because of the specimen's magnetic anisotropy, especially for pottery (e.g. Veitch et al., 1984; Chauvin et al., 2000). Following Schnepp et al. (2016) for correcting the specimens' NRMs for anisotropy, anisotropies were determined by imprinting anhysteretic remanent magnetisation (ARM) on one sister specimen. The specimens were demagnetised with four AF steps of 10, 35, 100 and 250 mT in order to check for absence of secondary magnetisation components. The last step was done using a Magnon AFD300 demagnetiser while demagnetisation up to 100 mT was done using the in line AF device of the 2G magnetometer. Then the ARM was imprinted at a 150 mT demagnetising alternating field in the presence of a 50 μT constant field in 6 directions ($\pm$X, $\pm$Y, $\pm$Z) with the Magnon device. The ARM tensor and the anisotropy corrected NRM values were then calculated following Veitch et al. (1984) using the software RenArmag provided by P. Lanos.

6. Magnetic Directions Obtained From Archaeological Material

6.1. Thermal (TH) and Alternating Field (AF) Demagnetisation

In order to remove secondary components, several thermal and alternating field demagnetisations were conducted for the different sites.The demagnetisation experiments were used in order to analyse the specimen's NRM to find the ChRM of the primary TRM. The results of the analysis of palaeodirection that are presented in detail in this thesis are those of ovens THX, THY and THZ from Thunau am Kamp, while the directions of the other Thunau ovens were taken from Schnepp (2017) and are listed in table 6.1 (p.52). The directions of the sites TH2,TH5, TH8 and TH9 are those of the ovens associated to the unoriented shards. The directions for Semlach (Schnepp, 2016) are summarized in table 6.1 as well.

Because the Thunau oven floors showed a gradient from well baked in the upper part to weakly baked some centimetres below, the characteristic directions were determined from those specimens from the well baked parts, which provided the best chance of having a strong TRM imprinted. Because this was normally the case for only one specimen per sample, the sample set was divided into two groups. The specimens with even core numbers were used for alternating field demagnetisation, while the specimens with uneven numbers were used for thermal demagnetisation.

For the thermal demagnetisation of the specimens a MMTD80 furnace was used to heat and cool the specimens in a zero-field environment. The median destructive temperature (MDT) as well as the temperatures where 10% and 90% of the NRM are lost were determined

to find suited temperature intervals for the following MSP-DSC esperiments (see section 7.2). Starting at 100 °C, the temperature was increased in 50 °C steps up to a temperature of 600 °C. As soon as a specimen's NRM increased in two consecutive steps, then the demagnetisation process was stopped prematurely for this specimen because of obvious thermal alteration.

The 2G demagnetiser, in line with the magnetometer was used for the AF demagnetisation. In the demagnetiser, shielded as the magnetometer with a μ-metal case and the compensating field of the external coils, the specimens were demagnetised in all three spatial directions. The alternating field intensity was increased and applied in steps of 2, 3, 5, 7, 10, 15, 20, 25, 30, 35, 50, 75 and 100 mT. If the residual NRM of a specimen was still larger than 10 % of its initial value at the step of 75 mT, then a 120 mT step was executed instead of the 100 mT step. To analyse the NRM's stability, the median destructive fields (MDF) and median destructive temperature (MDT) were determined from the AF and TH demagnetisations. The values are plotted in figures 6.1 a) and b). All specimens show MDFs between 10 and 17 mT. There is no significant difference between the MDFs for the specimens of the three ovens. The same can be said for the shape of the demagnetisation curves. Most specimens reach their point of losing 90 % of NRM already at AF fields between 35 and 100 mT (figure 6.2e)).

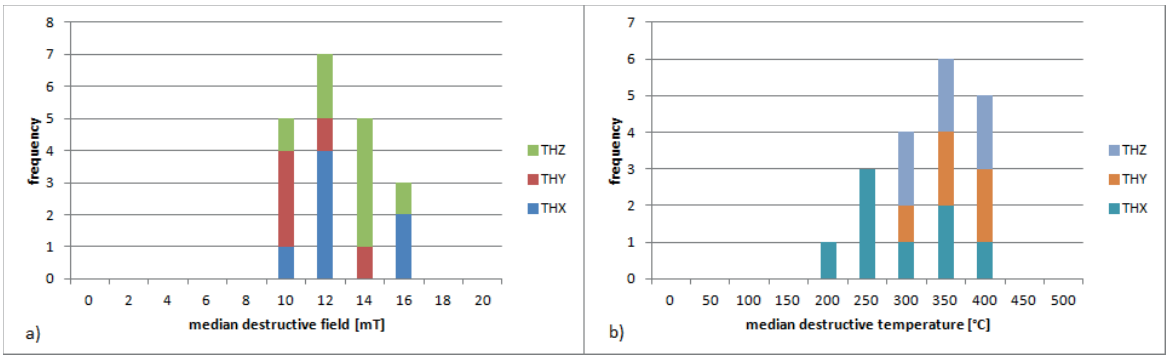

Figure 6.1.: a) Median destructive field for Thunau specimens from alternating field demagnetisation ;b) Median destructive temperature for Thunau specimens from thermal demagnetisation.

Opposite to the specimens' MDFs, their MDTs are generally relatively high. While the values of THY and THZ are all between 300 °C and 450 °C, the values of THX scatter over the range between 150 °C and 450 °C. In general, the specimens of THX gave less stable demagnetisation curves than THZ and THY. As all the MDT values of THY and

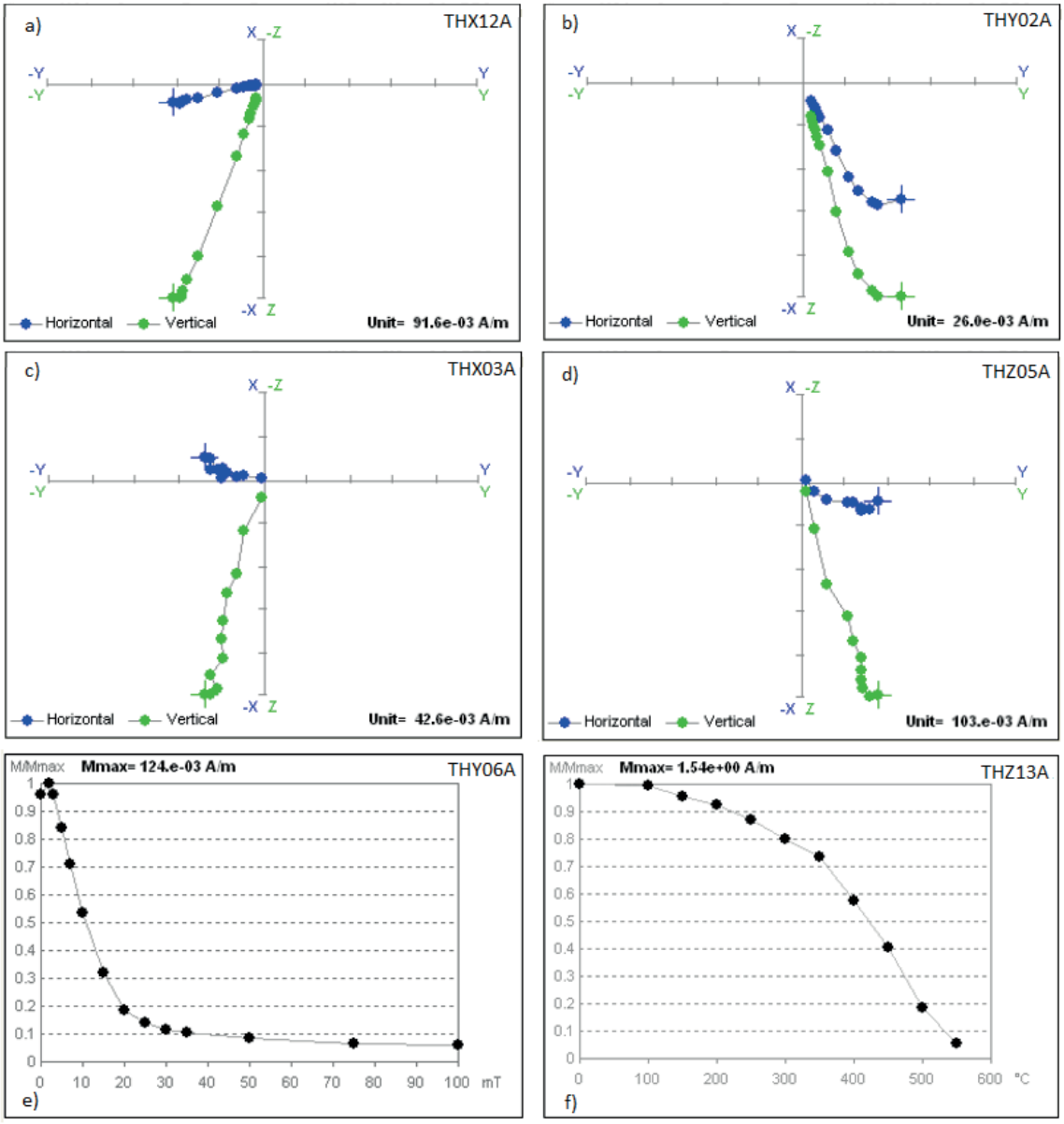

Figure 6.2.: Zijderveld diagrams (cf. figure 3.1) of alternating field (a and b) and thermal (c and d) demagnetisation. Exemplary NRM decay curves are shown for an AF (e) and a TH (f) demagnetisation.

THZ and half the MDT values of THX are higher than 300 °C, high blocking temperatures are indicated.

By analysing the NRM's directional change in Zijderveld diagrams, as shown in figure

6.2, the characteristic direction was determined. All AF demagnetisation experiments gave results as exemplified in figures 6.2a) and b). For specimen THX12A (figure 6.2a), the NRM decays in a straight line to the origin, indicating a single component NRM. This was the case for all THX specimens and for about two thirds of THY and THZ specimens. The other specimens showed a secondary component that was removed at very low field steps. These secondary components of the THZ specimens were removed at higher AF fields than those of the THY specimens. The decay of one of the THY specimens with a secondary component is shown in figure 6.2b). As the secondary components were removed at very low fields of < 10 mT, it can be assumed that they are a VRM overprint caused by Earth's magnetic field due to the low coercive force of a VRM (Soffel, 1991).

The data points of the thermal demagnetisation form less perfect straight lines to the origin than those of the AF demagnetisation as seen in figure 6.2. Two specimens of THX could not be used for the determination of the characteristic direction, because they did not show a stable directional behaviour along the entire thermal demagnetisation process. All secondary NRM components that were found for specimens of the three ovens could be removed at low temperatures of up to 200 °C. The low blocking temperatures of the secondary components support the conclusion that they were VRM overprints.

6.2. Characteristic Directions

The resulting ChRM directions of AF and TH demagnetisation were analysed together to find the hierarchical mean ChRM of each oven, as described in section 3.1. The ChRM directions were first averaged for every independently oriented sample and then these sample mean ChRM directions were averaged for each complete oven. The mean directions as well as the distribution of the sample ChRM directions, determined with the demagnetisation experiments of one specimen per sample, are shown in figure 6.3 a). In red, the oven mean direction and the α_{95} confidence circles are plotted while the sample directions are shown in black (THX), green (THY), and blue (THZ). The high precision parameters and small α_{95} radii (Fisher, 1953) of the three ovens indicate that the directions are reliable (see table 6.1). The larger α_{95} radius of THZ indicates clearly that the directions from the demagnetisation experiments show a much larger scatter than those of THX and THY. A reason could be a flattening of the oven during levelling of the area after the valley settlement was abandoned.

In the course of the ChRM determination, two directions of THZ specimens (indicated with pink circles in figure 6.3) were rejected in an outlier-test (McFadden, 1982).

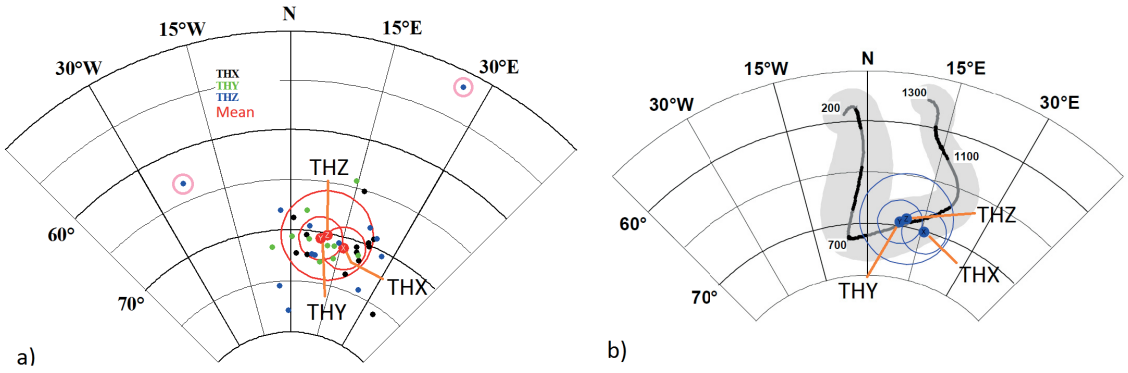

Figure 6.3.: a) Mean ChRM direction of the Thunau ovens plotted on sample and feature hierarchical level. For the feature means, α_{95} circles are shown in red. Pink circles mark two rejected outliers; b) Mean ChRM directions of Thunau ovens reduced to Radstadt in relation to Austrian reference curve in the range from 200 AD to 1300 AD. Modified after (Schnepp et al., 2015).

When comparing the mean ChRM directions to the Austrian reference curve (Schnepp et al., 2015), it can be seen that they plot along the curve. As delineated in chapter 4.2, the stratigraphy of the three ovens gives a chronological order: THX is the youngest, THZ the oldest and THY in between. In relation to THY and THZ, THX obviously plots on the younger part of the curve. However, the THZ mean direction plots right of THY, but due to the large α_{95} radius of THZ, it is not justified to claim a contradiction to the chronological order. A complete summary of the characteristic directions with the Fisher statistics parameters (Fisher, 1953) of the ovens THX, THY and THZ, as well as the other Thunau ovens from Schnepp (2017) and the three Semlach furnaces (Schnepp, 2016) is presented in table 6.1.

Feature	n	N	D(°)	I(°)	K	α_{95}
SE1	8	7	357.0	53.5	152	4.9
SE4	7	6	350.4	59.8	130	5.9
SE6	22	12	354.0	62.4	190	3.2
TH2	16	16	14.3	70.1	681	1.4
TH5	16	11	16.4	69.9	203	2.7
TH8	10	9	357.7	69.2	689	2.0
TH9	15	9	17.1	66.2	139	3.4
THP	15	15	15.6	72.2	466	1.8
THT	15	15	10.0	70.6	617	1.1
THU	15	15	12.5	69.3	228	2.5
THX	15	13	15.8	70.1	396	2.1
THY	10	10	8.8	69.6	516	2.1
THZ	14	13	10.4	69.2	90	4.4

Table 6.1.: Characteristic directions of all investigated sites. Directions of Semlach sites from Schnepp (2016), directions of sites TH2 to TH9 from Schnepp et al. (2015) and directions of sites THP to THU from Schnepp (2017); Feature name, number of independent samples, number independent ChRM directions, Declination and Inclination with Fisher precision parameter (Fisher, 1953) and α_{95}.

7. Palaeointensity Determination Using Archaeological Material

The palaeointensity of the geomagnetic field was measured with two different methods in the frame of this thesis. One series of the Thellier experiment (see section 3.2.1) was performed for selected specimens of 9 features as well as a series of the domain-state corrected multispecimen protocol method (see section 3.2.2) for each feature or shard set. An AF and/or a TH demagnetisation of a sister specimen was used to determine if the NRMs of a sample could be assumed as a stable magnetisation without a strong overprint of secondary components. This was taken as prerequisite for specimens chosen for the intensity experiments because the specimen's NRM had to be a presumably pure TRM. As for the thermal demagnetisations, a MMTD80 furnace was used to heat and cool the specimens in a zero-field environment. A DC field coil inside the furnace can be used to generate an axial field inside the furnace.

7.1. Thellier-Thellier Experiment

For the determination of palaeointensities, the Thellier experiments (Coe, 1967) were used with 6 pTRM checks, 4 additivity checks (Krása et al., 2003) and 5 pTRM-Tail-checks (Riisager and Riisager, 2001). In this experiment, the decay of NRM as well as the increasing fraction of artificially imprinted pTRM is measured at defined temperature steps and used to define the slope of a straight line, that gives the palaeointensity when multiplied with the intensity of H_{lab} (see section 3.2.1). The executed steps of the experiment are listed in table 7.1. For the heating, all specimens were put in a holder together in the same order for every step and a pTRM was imprinted in the specimens' Z-direction. For the specimens of THP, a 10 mT AF demagnetisation step was executed before every measurement step

Step	Temp. (°C)	Type	Field (μT)	Step	Temp. (°C)	Type	Field [μT]
1	20	NRM	0	22	400	PTRM	60
2	100	THD	0	23	300	AC	0
3	100	PTRM	60	24	440	THD	0
4	150	THD	0	25	440	PTRM	60
5	150	PTRM	60	26	440	TC	0
6	150	TC	0	27	480	THD	0
7	200	THD	0	28	400	PC	60
8	100	PC	60	29	480	PTRM	60
9	200	PTRM	60	30	400	AC	0
10	100	AC	0	31	510	THD	0
11	250	THD	0	32	510	PTRM	60
12	250	PTRM	60	33	150	TC	0
13	250	TC	0	34	540	THD	0
14	300	THD	0	35	480	PC	60
15	200	PC	60	36	540	PTRM	60
16	300	PTRM	60	37	480	AC	0
17	350	THD	0	38	570	THD	0
18	400	PTRM	60	39	570	PTRM	60
19	350	TC	0	40	600	THD	0
20	400	THD	0	41	540	PC	60
21	300	PC6	0	42	600	PTRM	60

Table 7.1.: Heating steps for the Thellier experiment. Abbreviations: THD: Thermal demagnetisation, PTRM: imprinting of a pTRM, PC: pTRM-check, TC: Tail check, AC: Additivity Check.

to remove a VRM component, because all specimens of this oven had small secondary components.

The resulting palaeointensity was calculated with the ThellierTool 4.0 (Leonhardt et al., 2004). This program is able to evaluate pTRM, tail and additivity checks as well as plotting orthogonal projections of NRM decay and directions. The results of the automatic determination of intensities by the ThellierTool were plotted in Arai-plots as well as in Zijderveld diagrams. The linear fit of the slope was determined by maximizing the quality factor q. The quality of the palaeointensity determinations can roughly be divided into

three groups, as seen in figure 7.1 a)-c). This subjective division into groups was based on the linearity of the curve and the amount of data points used to find the slope by the automatic selection of ThellierTool.

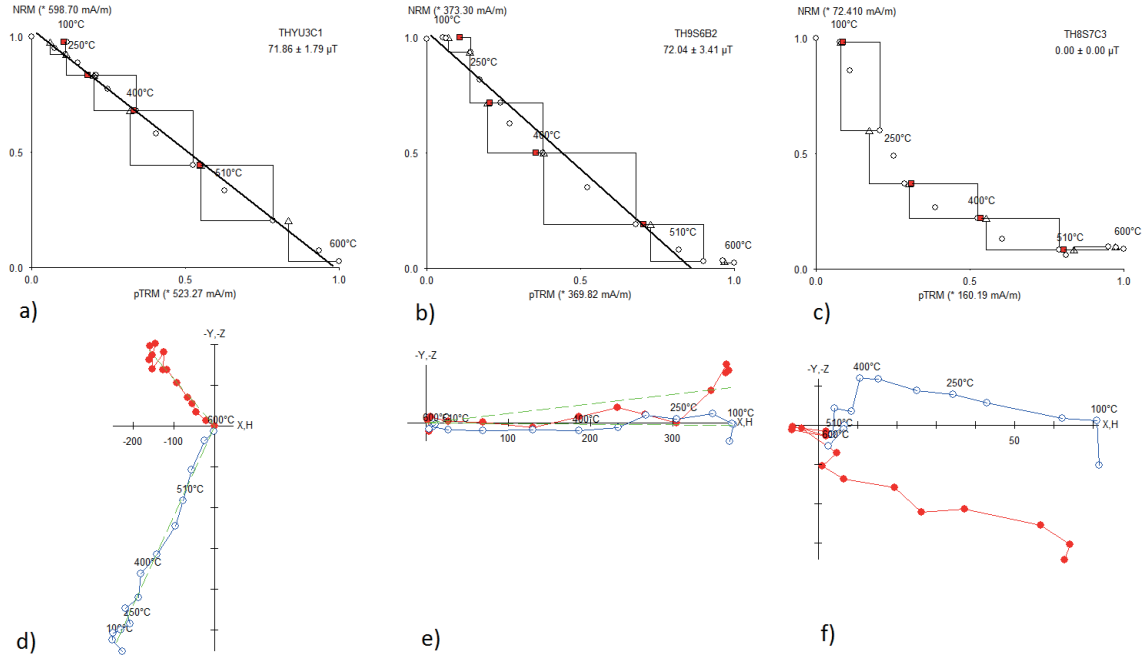

Figure 7.1.: a)-c): Arai plots with pTRM-checks (white triangles), additivity checks (red squares) and line of linear fit of automatic evaluation in black; d)-f), Zijderveld diagrams showing in red the horizontal (X,Y) and in blue the vertical components (Z,H) of the decay of NRM for different temperatures. Green lines show stable directions.

Figure 7.1 a) shows an example of an almost ideal result, representative for 6 specimens (table 7.3). The ratio of NRM to pTRM shows a linear trend with rising temperature and there are almost no secondary components visible in the Zijderveld diagram. All data points have been used find the slope. However, the domain state tests indicate PSD/MD character. Figure 7.1b), representative for 10 specimen, shows measurements that do not show a good linear trend in the Arai plots possibly due to MD behaviour of the specimen (Biggin and Poidras, 2006a), but can still be used to determine palaeointensities. Specimens showing this type of result often have small amounts of secondary components at low temperatures, larger alterations at high temperatures or both. Therefore, the amount of data points used to define the slope was here smaller than the total of 14, but still larger than 5. Most of the specimens measured in this thesis show behaviour like this. The third

Type	A	B
Linear fit criteria		
Number of Points (N) $\geqq$	5	5
Standard Deviation (Std) $\geqq$	0.1	0.15
Fraction of NRM (f) $\geqq$	0.5	0.3
Quality Factor (q) $\geqq$	5	0
Directional Criteria		
MAD (anchored) $\leqq$	6	15
MAD (not anchored) $\leqq$	999	999
Alpha $\leqq$	15	15
Alteration Criteria		
Relative check error d(CK) $\leqq$	5	7
Cumulative check diff. d(pal) $\leqq$	5	10
Difference ratio (DRAT $\leqq$)	999	999
Repeated demagnetisation steps		
Normalized tail of pTRM d(t) $\leqq$	3	99
Relative intensity diff. $\leqq$	10	15
Additivity checks		
Relative AC error d(AC) $\leqq$	5	10

Table 7.2.: Default criteria parameter for classification of results in the ThellierTool software.

type, representative for 3 specimens and shown in figure 7.1 c), does not exhibit any linear trend in the Arai plot and fails in determining a palaeointensity from specimens that show this type of result. Specimen are determined to be type c) if the standard acceptance criteria of the ThellierTool are not met. They are also not used for dating.

A classification, based on measurement data was the classification done by the ThellierTool. Three classes were determined based on the programme's default criteria parameters, shown in table 7.1. Class C does not have any criteria parameters, but is instead chosen if the data does not satisfy the criteria of classes A and B. However, the choice of selection criteria may lead to a systematical bias of the resulting intensity values (Leonhardt et al., 2004). A comparison between the ThellierTools classes and the subjective types can be seen in table 7.3.

Site	Spec.	T_{min} -	T_{max} (°C)	H_{Lab} (μT)	H_{Pal} (μT)	StD (μT)	N	f	g	q	MAD	T./C.
SE6	SE6K4Z11*	0	600	60.0	62.92	5.60	14	0.92	0.79	8.24	6.81	c/C
	SE6K6Z16	200	600	60.0	68.60	0.81	11	0.59	0.88	43.95	2.28	a/A
TH5	TH5T3B2	300	600	60.0	74.82	1.51	9	0.79	0.85	33.58	4.55	b/A
	TH5T5B2	350	600	60.0	52.97	1.07	8	0.65	0.82	26.39	4.29	b/B
TH8	TH8S07C3*	0	600	60.0	x	x	x	x	x	x	x	c/-
	TH8S10B2*	0	600	60.0	28.47	3.78	5	0.39	0.74	2.18	15.85	c/B
TH9	TH9S3C2	200	600	60.0	41.83	4.09	11	0.97	0.88	8.68	6.53	b/B
	TH9S6B2	0	540	60.0	72.03	3.41	12	0.98	0.88	18.3	8.21	b/B
THP	THP01C13	150	570	60.0	61.64	4.94	11	0.96	0.89	10.7	3.36	b/B
	THP02A12	250	600	60.0	61.49	0.76	10	0.83	0.88	59.3	1.79	b/A
THT	THT23A3	300	540	60.0	65.55	0.71	7	0.56	0.82	42.0	4.14	b/B
	THT25B3	0	600	60.0	69.58	1.47	14	0.97	0.91	41.7	4.97	a/A
THU	THU16B15	250	570	60.0	60.80	1.29	9	0.72	0.87	29.6	5.13	b/B
	THU16G13	0	600	60.0	67.50	1.83	14	0.99	0.92	33.6	4.39	a/B
	THU18C15	0	600	60.0	59.78	2.10	14	0.99	0.91	25.7	3.16	a/B
THX	THXU2A2	0	540	60.0	63.71	2.72	12	0.83	0.89	17.4	4.07	b/B
	THXU2B2	100	540	60.0	69.36	2.68	11	0.75	0.88	17.1	5.21	b/A
THY	THYU3B1	0	600	60.0	67.84	0.86	14	0.99	0.91	70.5	3.98	a/B
	THYU3C1	0	600	60.0	71.85	1.78	14	0.98	0.89	35.3	4.74	a/B

Table 7.3.: Archaeointensity results from Thellier-Thellier experiments. Site, specimen name, Minimum and maximum temperature used to determine intensity, used laboratory field, resulting palaeofield, standard deviation, N: data points for slope, f: NRM fraction, g: gap factor, q: quality factor (Coe et al., 1978), MAD: maximum angular deviation (anchored), Curve type (T.) as in figure 7.1a)-c)/ class (C.) determined from ThellierTool with standard criteria parameters. Specimens marked with (*) were not used for dating.

Very good results, as seen in figure 7.1a), are observed for both specimens of THY and two specimens of THU (THU16B15 and THU18C15) as well as one of THT (THT25B3). In contrast, the specimens of TH8 and SE6K4Z11 give very poor results as in figure 7.1c) and it was only possible to tentatively determine the archaeointensity for two of the three specimens. Due to several warnings of the ThellierTool because of a high MAD and a low quality factor, these results were rejected and not used for dating. The specimens from all other features show results similar to figure 7.1b). Of these specimens, the ones taken from ovens like THX and THP as well as specimen SE6K6Z16 from furnace SE6 show more linear behaviour than the ones taken from ceramic shards, such as TH5 or TH9. Both specimens of TH5 seem to have stronger secondary NRM components and therefore the temperature range up to 300/350 °C could not be used for the determination of archaeointensity. The specimens of THX as well as the specimens of THU and THT show non linear behaviour in the temperature interval above 540 °C due to mineral alterations but well defined straight lines for lower temperatures. The resulting palaeointensities for all 9 features can be found in table 7.3 and the corresponding plots can be found in appendix A.

7.2. Multispecimen Protocol Method

As second method of determining palaeointensity, the MSP-DSC version (Fabian and Leonhardt, 2010) of the multispecimen protocol method (Dekkers and Böhnel, 2006) was used. The executed series of steps is described in section 3.2.2. To be able to imprint H_{lab} (anti-)parallel to the anisotropy-corrected NRM of the specimens, they were mounted in a holder made in the institute's workshop (Schnepp et al., 2015) as seen in figure 7.2. With this device, it is possible to heat series of up to 8 specimens simultaneously in the same field H_{lab} while they were all individually oriented according to their anisotropy-corrected NRM directions.

As it is preferable to distribute the data points defining the line for PI determination evenly, the intensities of H_{lab} were chosen between fields of 24.8 and 86.8 μT, which were generated by the oven's DC field coil with corresponding currents between 80 and 280 mA. Starting with 80 mA, the fields for the experiments were generated with currents in 20 mA steps up to the maximum current. When finding the composition of specimens for the measurement series, the goal was to get one measurement per field for every feature of Thunau am Kamp

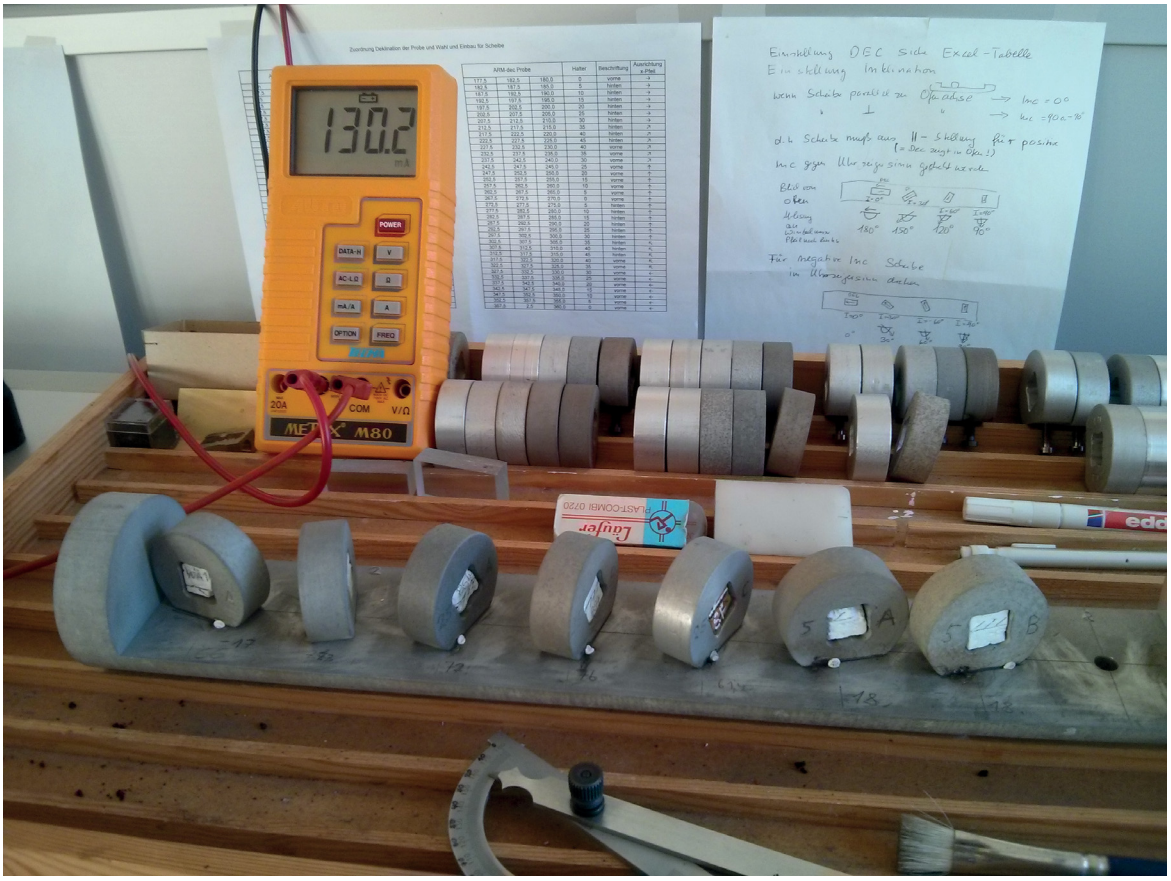

Figure 7.2.: Specimen holder for MSP-DSC experiments in the front. Seven of eight possible specimen are visible. An Amperemeter to control the field H_{Lab} can be seen in the background as well as different specimen holders for different NRM declinations of the specimen.

and two measurements per field for every feature of Semlach because there was much more sample material available from Semlach than from Thunau.

As mentioned in section 6.1, the temperatures for the heating steps were chosen according to the sister-specimen's behaviour in TH demagnetisation as well as during temperature dependent susceptibility measurements. Two constraints had to be met during the MSP-DSC measurement: The temperature had to be below the specimen's alteration temperature and high enough that a significant NRM fraction could be reached. Therefore, the upper temperature limit was the alteration temperature, determined by the temperature dependent susceptibility measurements. As a lower limit, the specimen's MDT was determined from a thermal demagnetisation of a sister specimen. To avoid alterations, the measurements temperatures were chosen closer to the lower limit. If the specimen's MDT was significantly

higher than its alteration temperature, then the specimen was not used for the measurement. If the specimen's MDT was only a little higher than the alteration temperature, then the specimens were used but the used temperature was below the lower limit to avoid alterations. Because the heating steps were performed for up to eight specimen from up to eight different sites, the temperature restrictions were not met for every specimen at every series with certain temperature and field values. After evaluation of the NRM fractions after a measurement, the temperature level for the sister specimen was changed if the specimen's NRM fraction was too low or too high.

The evaluation of the experiments was done with the software MSP-tool provided by R. Leonhardt (https://github.com/leonro/MSPTool). Measurements were only accepted if following MSP-Tool criteria parameters were met:

Criteria	Value
NRM fraction	
Lower limit	0.2
Upper limit	0.8
Angular difference	15°
Thresholds	
m3-m1	-0.01
m3-m4	-0.01

Results of Dekkers-Böhnel MSP, fraction corrected MSP and domain state corrected MSP were calculated, plotted by the program and are presented in table 7.4 on page 61. The domain state corrected MSP plots of all sites are shown in figure 7.3. The fraction corrected MSP plots as well as plots of the NRM fraction distribution and the angular deciations can be found in appendix B.

SE1: 25 specimens out of the 30 specimens prepared from from 4 unoriented block samples of furnace SE1, have been accepted. The domain state corrected result and the fraction corrected result both give a lower palaeointensity estimate than the Dekkers-Böhnel method. Most accepted specimens had relatively low fractions of 0.2 to 0.35 (for distributions of NRM fractions see appendix B). Figure 7.3 pictures a well defined line having a coefficient of determination of 0.96 (cf. table 7.4). Although some data points obviously lie far from this line, a small error of the estimate is obtained. This is due to the small scatter of the data points at low fields which have a high linear relationship. At fields higher than 60 μT,

data points are much more scattered and the error bars of the single measurements are generally larger than at the lower fields. Therefore those data points contribute less to the definition of the line.

Site	N/n	n_{acc}	MSP-DB (μT)	MSP-FC (μT)	MSP-DSC (μT)	$Error_{DSC}$ (μT)	r^2_{DSC}	Q_{DSC}
SE1	4/30	25	59.84	56.72	57.97	2.07	0.96	39.62
SE4	5/24	33	82.55	83.06	74.81	4.11	0.92	84.26
SE6	5/31	23	64.51	63.09	64.34	1.03	0.71	23.41
TH2	2/7	4	61.28	60.71	59.60	6.24	0.96	27.45
TH5	5/21	12	58.15	55.65	55.48	9.24	0.83	21.86
TH8	6/24	10	4.42*	22.05*	37.65*	1.02	0.99	33.22
TH9	5/19	6	48.44	32.53	42.9	8.37	0.66	6.84
THP	2/9	6	79.15	78.26	78.22	7.52	0.88	69.91
THT	4/17	11	58.62	53.20	53.48	5.56	0.98	70.99
THU	2/24	17	62.99	60.11	60.60	2.60	0.93	71.69
THX	2/11	10	67.12	65.56	62.21	7.28	0.98	74.43
THY	3/19	18	61.95	59.64	57.52	3.32	0.98	61.59

Table 7.4.: Results of MSP-experiments; Site, Number of independently oriented samples/ Number of used specimens, Number of accepted specimens, Results of Dekkers-Böhnel, Fraction corrected and domain state corrected versions of the MSP, correlation coefficient of MSP-DSC result, quality factor. Results marked with (*) are only shown for the sake of completeness, but were not used for dating.

SE4: 24 specimen measurements were accepted of the 33 initial specimens of five blocks. Six measurement values were rejected due to low fractions and three specimens were removed manually because of alignment errors while mounting the specimens in the holder. The intensity result of the MSP-DSC is 74.81 μT ($\pm$4.11) (see table 7.4). This value is much lower than the MSP-DB and MSP-FC results. Due to the low scatter of most data points and the small error bars of the single measurements, especially at small fields, the error of the intensity is small.

SE6: The 23 accepted specimens of the initial 31 specimens give almost identical results for MSP-DB, MSP-FC and MSP-DSC (table 7.4). Two outliers can be seen at 34 μT and 70 μT. They were kept in the analysis because there was no indication for any measurement errors or alterations in the measurement data.

TH2: For oven TH2 little material was left from the study of Schnepp et al. (2015) for palaeointensity determination and only 7 specimen could be prepared. Almost all of the measured specimens were rejected. The specimens were very sensitive to alteration already at temperatures of 360°C and also seemed to be quite inhomogeneous regarding their alteration temperatures. Therefore, three of the initial seven measurements were rejected due to alterations. Due to the low number of specimens, the error margin of the MSP-DSC result is quite large, but the line has a high regression coefficient and is well defined. The results of MSP-DB and MSP-FC are similar to the MSP-DSC result and are within the error margin of MSP-DSC.

TH5: 12 specimens out of 21 were accepted. Here, the different pieces of the ceramic reacted very differently to the temperature during the experiment. While the measurements of the specimens of the gray shard TH5T1 were all successful at a temperature of 360 °C, the reddish specimens of TH5T3, TH5T4 and TH5T5 had only a few successful measurements because high temperatures of 400 °C and 480 °C were necessary to achieve a sufficiently high fraction. Overall, the size of the error bars of the measurement values increased with increasing H_{Lab}. The large error bars in combination with the scatter of the data points result in a large error for the MSP-DSC result. The fraction corrected result was close to MSP-DSC, while the value of MSP-DB was higher.

TH8: Although 10 of 24 specimens were accepted for the shards TH8, the result of the experiment seems to be unreliable. As seen in the plot of MSP-DSC in figure 7.3, the data looks like there would be two independent data sets and two different regression lines would be possible. This hypothesis is not valid, because the two possible data sets consist of sister specimens of the same ceramic shards. Three data points lying above the regression line have very large error bars, indicating that strong alterations occured. The fitted line is finally defined by only two data points with very small error bars, while the others hardly contributed. This leads to a very high correlation coefficient and small a intensity error, which seem unreliable in representing the data. Therefore, the result of the MSP experiment will not be used for the dating of the ceramic shards of TH8.

TH9: The ceramic shards associated with oven TH9 had a very high rejection rate for the MSP measurements. Only 6 out of 19 specimens were accepted for the intensity determination. Almost half of the specimens were rejected due to low NRM fractions. Again, this is the result of inhomogeneous distribution of blocking temperatures over sister specimens. The MSP-tool suggests to reject the measurement.

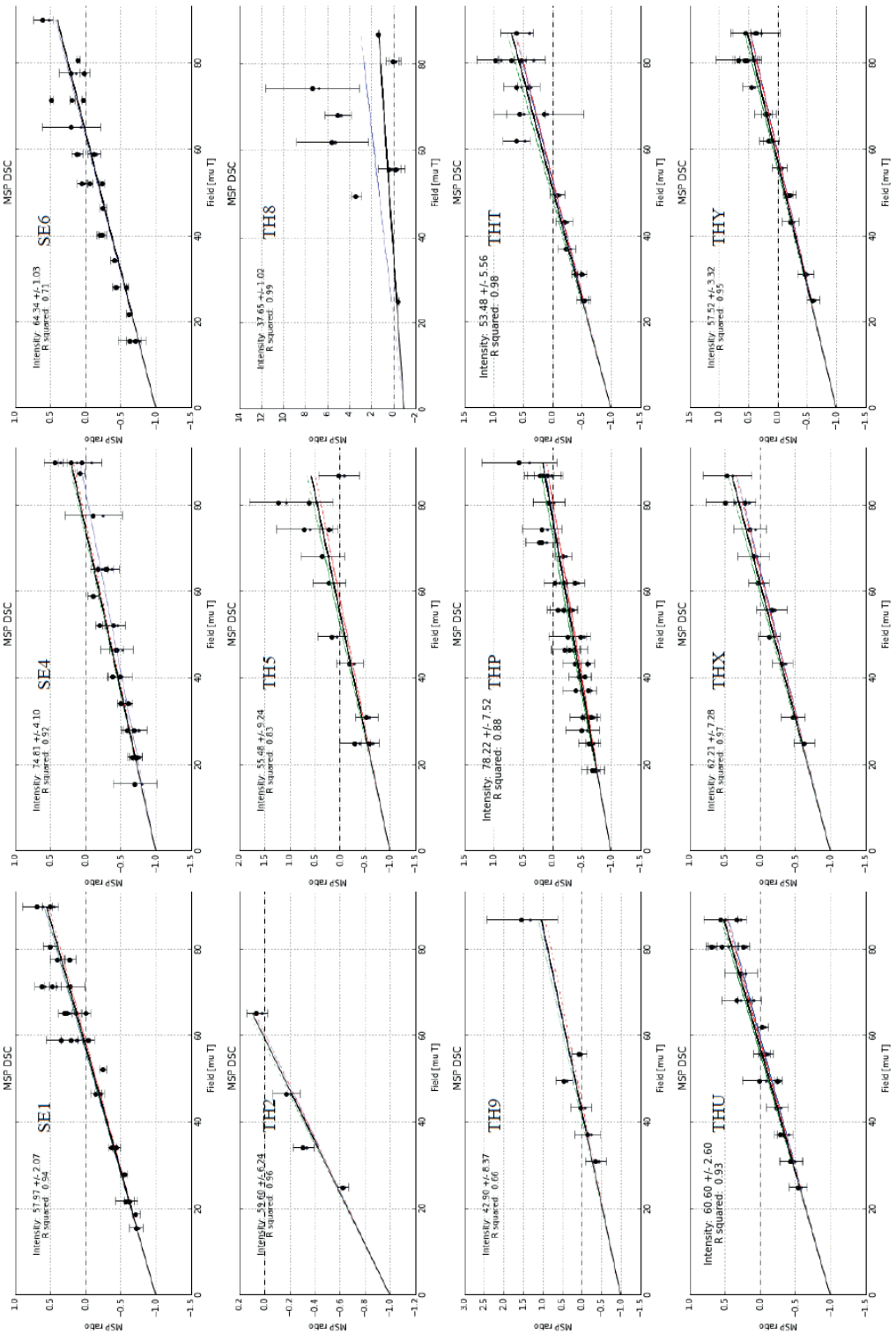

Figure 7.3.: Results of domain state corrected multispecimen protocol method of all investigated sites. Plotted are domain state corrected data points with associated error bars and the regression line in black.

As the plot of the data points does not look too bad, the result of MSP-DSC will be used in a dating attempt, keeping in mind that it may be not reliable.

THP: All nine measured specimens were accepted for THP. As the number of specimens was very low, the data was used in combination with MSP data of THP provided by E. Schnepp. Therefore, the total number of used specimens was 32. The results of the complete set of specimens is shown in table 7.4 and in figure 7.2. MSP-DB, MSP-FC and MSP-DSC have similar results and a large error margin due to large error bars of the single measurements.

THT: Of the 17 specimens of THT, 6 were rejected due to low NRM fractions. The accepted specimens plot with relatively low scatter around the regression line. Here, MSP-DB and MSP-FC results are both higher than the MSP-DSC result.

THU: 17 of 24 specimens were accepted. Four specimens were rejected due to high differences between NRM and m1 values, the rest due to low fractions because of too low temperatures. MSP-DB and MSP-FC result in similar values as MDP-DSC and are both in the range of the error margin of MSP-DSC.

THX: For this oven, only one specimen was rejected because of a low NRM fraction. Again, the result of MSP-DSC is lower than both MSP-DB and MSP-FC which are inside the range of the error margin of MSP-DSC.

THY: Similar to THX, only one of 19 specimens was rejected for THY. This time, an angle difference due to a specimen alignment error was the reason for the rejection. In contrast to the experiments of most other sites, here MSP-DSC gives a lower result than both MSP-DB and MSP-FC.

8. Discussion of Archaeomagnetic Results

To use the measured archaeomagnetic data for dating purposes, it has to be certain that the field data represents the palaeomagnetic field. To confirm that, a short discussion about the reliability of both archaeomagnetic directions and intensity data is necessary.

8.1. Direction of Palaeomagnetic Field

The low median destructive fields of the three ovens THX, THY and THZ from the rock magnetic measurements in section 6.1 suggest that a low coercive phase is present. The median destructive temperature of 300°C and higher as well as Curie temperatures of about 580°C indicate that the main carrier of magnetisation is magnetite (Soffel, 1991). With the exception of two specimen (THX01A,THX05A), all demagnetised specimen show linear behaviour of the NRM decay and only small secondary components. The high Q values indicate that the material was well baked. It can therefore be assumed that the main fraction of magnetisation is a TRM.

In order to evaluate the validity of the archaeomagnetic directions further, they are plotted together with the PSV reference curve as already done in section 6.2. In figure 8.1, they are plotted together with all other directions obtained from features of Thunau (Schnepp, 2017) to check if the directions are reasonable. Figure 8.1 shows that the directions of all three features plot to a reasonable position of the curve and are right in the middle of the directions of the other sites. Despite THZ having a lower precision parameter and a higher α_{95} radius than THX and THY (see table 6.1) probably due to flattening of the oven during levelling of the area, the precision parameters of all three ovens are far larger than 50 and the directions can therefore be considered to be reliable (Tarling and Dobson, 1995).

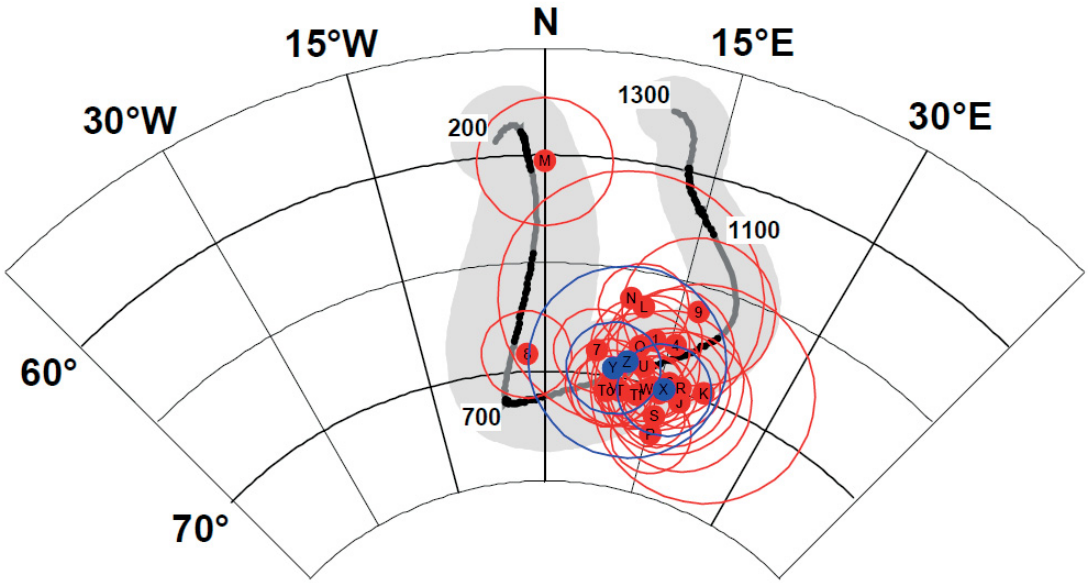

Figure 8.1.: Mean ChRM direction of Thunau features analysed in this thesis (blue) in comparison to the PSV reference curve (black) and the ChRM directions of all other Thunau features (red). Modified after Schnepp (2017).

As the mean directions of the three features plot closely to each other, an F-test (McFadden and Lowes, 1981) was conducted to check if the three sites are statistically significantly different. The results of this test are shown in table 8.1. It shows that all sites are not significantly different from each other at the 95 % confidence level. As expected, the three

Combination	f_1	f_2	Different?
THX & THY	0.109194	0.153331	No
THX & THZ	0.024855	0.132947	No
THY & THZ	0.003280	0.153331	No

Table 8.1.: Results of an F-test (McFadden and Lowes, 1981): combination of tested directional results and parameters of f-distribution. Distributions are significantly different, if $f_1 > f_2$.

features are not statistically different, which is not unusual for features that are dated that closely together. Despite the three features not being statistically different, the directions were not merged so it would be possible to date the features with the measured values in section 9.

8.2. Palaeointensity of Geomagnetic Field

To check if the intensities are reliable, the results of the Thellier experiments (see appendix A and table 7.3, page 57) have to be reviewed. For furnace SE6, specimen SE6K6Z16 shows linear behaviour in both Zijderveld and Arai plots as well as a high quality factor, while the specimen SE6K4Z11 with its high fraction and low quality factor was classified as class C by the ThellierTool. The data points of this specimen show a straight behaviour in the Zijderveld plot, but a concave-up Arai plot. The additivity and pTRM checks are both not good and the specimen was therefore rejected, while the resulting intensity of SE6K6Z16 was considered to be reliable.

Both specimens of TH5 show linear behaviour in the Zijderveld diagrams and also in the Arai plots above temperatures of 250-300°C. Therefore, only data points above 300°C were used to fit the slope in the Arai plot. The q and f values are high for both specimen and ThellierTool classifies them to be class A and B. The intensity results of both specimen are about 20 μT apart from each other and a mean value could be used. However, as the value of TH5T5B2 is almost exactly the same as the intensity value of the MSP-DSC series of TH5, both values will be used separately for dating as there are no indications that one of the two values would not be reliable but it is possible, that the different ceramic shards do not origin from exactly the same time.

The two specimen of TH8 are considered to be not reliable because they do not show straight behaviour in the Zijderveld diagrams or the Arai plots. The data points of the specimens of TH9 show straight behaviour in the Zijderveld diagrams, but are slightly curved in the Arai plots. Due to the high f and medium q value, they are both classified as B by ThellierTool. The pTRM checks of TH9S3C2 are good up to temperatures of about 500°C. TH9S6B2 has better checks and than TH9S3C2. Although the result of TH9S6B2 looks more reliable and has a higher q value, the result of TH9S3C2 matches with the result of the MSP-DSC experiment. As both specimens origin from different ceramic shards, it is possible that they are somewhat different in age. Therefore, both values are again used separately.

For oven THP, both specimens show linear behaviour in the Zijderveld diagrams and high f values. Due to the higher quality factor, specimen THP02A12 is classified as A, while TH9S3C2 as B. Additivity and pTRM checks are good for both specimens but get worse above 550°C for THP01C13. THP01C13 is also slightly curved in the Arai plot and the

high temperature data points are not used to define the slope. In contrast, the data points of THP02A12 show linear behaviour in the Arai plot only for temperatures above 250°C. Nevertheless, both results are very good and the intensities match each other.

The same can be said for the specimens of THT. Their intensities are similar to each other. Both show straight behaviour in Zijderveld diagrams and Arai plots as well as high quality factors. Although THT23A3 has bad pTRM checks above temperatures above 550°C, both results were considered to be reliable.

All three experiments for specimens of oven THU result in similar intensities, show linear behaviour in the Zijderveld diagram as well as high f and q values and are all classified as class B by ThellierTool. THU16G13 and THU18C15 also show straight behaviour in the Arai plot and good additivity and pTRM checks and all data points have been used to define the slope. THU16B15 shows linear behaviour only above 250°. Still, all three intensities were reliable and have been used for dating.

THXU2A2 and THXU2B2 are both linear in the Zijderveld diagrams but slightly curved in the Arai plots. Both additivity and pTRM checks are not perfect for both specimens, but the f and q values are high and Thellier Tool classifies them to classes A and B. The resulting intensities of both experiments are again similar to each other and have been considered reliable.

Both results for oven THY are reliable and similar to each other as they show good linear behaviour in the plots as well as good checks and very high q and f values.

As some of the results show some degree of curvature in their Arai plots, this has to be discussed as well. Such concave-up lines can originate from MD behaviour, or it can be caused by CRMs due to mineral alterations. Hervé et al. (2011) showed that such alterations can occur and remain undetected when the pTRM checks are positive. Such a masking of alteration occurs, when the specimen's NRM is approximately parallel to H_{Lab} during the Thellier experiment. So the directions of the specimens' NRMs have been checked. While the laboratory field was applied in $\pm$Z direction (inclination of $\pm$90°) the inclinations of the specimens used in the Thellier experiment ranged from $\pm$69° to 0°. Although their NRM directions are all closer to being parallel to H_{Lab} than being perpendicular to it, the specimens with small inclinations do not show a trend in direction of H_{Lab}. Therefore it seems that concave-up plots originate rather from MD behaviour than from alterations and

the results were accepted if the evaluation software showed no check failures or high errors (see appendix A).

A similar review for the MSP-DSC results is also necessary. As already stated in chapter 5, the resulting intensity of the measurement series of oven TH8 is unreliable. The MSP plots of TH8, looking like intensity results of two independent specimen, however raised the question if the ceramic shards actually originated from the same pottery item. A closer look at the data revealed, that the two supposedly different intensities were generated from sister specimen of the same shard samples. Therefore they had to be from the same pottery item and the bad intensity result seemed to originate from alterations. None of the plots of the other features showed any indication of a similar kind. For all experiments, the distribution of angular deviations between NRM and demagnetisation was mostly below 10°, for the ovens THP, THT, THU, THX and THY even below 5°. Most features show low fractions. For the ovens THT, THU, THX and THY there were so many fractions between 0.1 and 0.2 that the lower limit for these features was lowered to 0.1 from 0.2. All results have already been corrected for anisotropy. Three of the ovens (TH2, THP and THU) had the low number of 2 independently oriented samples that were used. The results of THP and THU have therefore been combined with more intensity data of these features, provided by E. Schnepp. The specimens of the other features origin from 3 to 6 independently oriented samples per feature. The correlation coefficients of the experiments are mostly very high even though the amount of used specimen ranges from 6 to 30. In published MSP results from Monster et al. (2015), 6 to 9 data points result in correlation coefficients of about 0.95, while the correlation coefficients in this thesis range from 0.66 (TH9) to 0.98 (THT, THX and THY), cf. table 7.4, p.61. With these factors considered, all MSP-DSC results, except the result of TH8, were considered to be reliable.

In the last step to verify the validity of the intensity data, the results of the MSP-DSC results are compared to the results of the Thellier experiment to see if systematic deviations are present. This is shown in figure 8.2, where the intensity values of the MSP-DSC experiments of all features that were evaluated with both methods are plotted against the intensity values obtained from the Thellier experiments. Correlating intensity values of both methods should plot and scatter evenly around the straight line with a slope of 1 that represents MSP-DSC intensity equals Thellier intensity. The resulting regression line, as seen in figure 8.2 as red line, suggest a slight but acceptable overestimation of intensities measured with the Thellier experiment in comparison to the MSP-DSC intensities. Nevertheless, there is a large dispersion between Thellier experiments of the same features as well as with respect

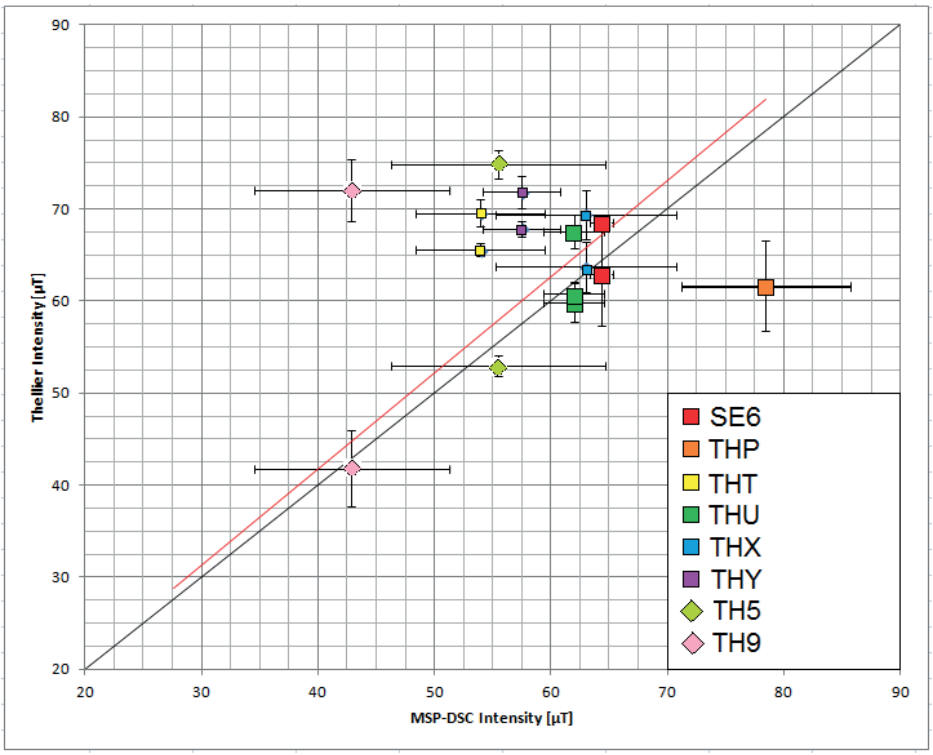

Figure 8.2.: Measured intensity values from Thellier experiment plotted versus measured intensity values of MSP-DSC experiments. The black line represents x=y, the red line represents the regression line anchored at the origin, squares represent specimens from ovens or furnaces and diamonds represent specimens from ceramic shards.

to the MSP-DSC results. This is seen especially for the results of the ceramic shards TH5 and TH9 (table 8.2).

The different intensity values for most of the features raised the question of which values to use for the dating. The intensity determinations themselves did not give any clue about if any of the values are more reliable than others and the scatter of the intensity values for the features seemed to be the result of inhomogeneous material and/or the different parts of the ovens/pottery not being baked homogeneously. If the intensity values of one feature showed small differences, then a mean value was used for dating. If the intensity values showed larger differences, then the site was dated two times, using each intensity value separately. Of the 12 features, there were intensity measurements conducted for 11. Three of them only had MSP-DSC data. The other eight sites had results for both MSP-DSC and Thellier-Thellier experiments. Of these eight, it was only possible for three sites (SE6, THU and THX) to calculate a mean intensity for both Thellier and MSP-DSC intensities because

Site	Type	Intensity (μT)	Error (μT)	Dating Intensity (μT)	Error (μT)
SE1	MSP-DSC	57.97	2.07	57.97	2.07
SE4	MSP-DSC	74.81	4.11	74.81	4.11
SE6	MSP-DSC	64.34	1.03	66.47	0.93
	Thellier	68.6	0.81		
TH2	MSP-DSC	59.6	6.24	59.60	6.24
TH5	MSP-DSC	55.48	9.24	54.23	6.58
	Thellier	52.97	1.07		
	Thellier	74.82	1.51	74.82	1.51
TH9	MSP-DSC	42.90	8.37	42.27	6.42
	Thellier	41.83	4.09		
	Thellier	72.03	3.41	72.03	3.41
THP	MSP-DSC	78.22	7.52	78.22	7.52
	Thellier	61.64	4.94	61.57	3.22
	Thellier	61.49	0.76		
THT	MSP-DSC	53.48	5.56	53.48	5.56
	Thellier	65.55	0.71	67.57	1.16
	Thellier	69.58	1.47		
THU	MSP-DSC	60.60	2.60	62.04	2.0
	Thellier	60.80	1.29		
	Thellier	67.50	1.83		
	Thellier	59.78	2.10		
THX	MSP-DSC	62.21	7.28	65.35	5.0
	Thellier	63.71	2.72		
	Thellier	69.36	2.68		
THY	MSP-DSC	57.52	3.32	57.52	3.32
	Thellier	67.84	0.86	69.86	1.4
	Thellier	71.85	1.78		

Table 8.2.: Measured intensities and intensities used for dating. Name of feature, experiment type, measured intensity and error, (mean) intensity and error used for dating.

their results were similar enough. This leaves five sites, where the intensity measurements of MSP-DSC and Thellier-Thellier experiments are so different, that two dating attempts had to be conducted because it was not possible to eliminate intensities due to a lack of observations of bad intensity results. The used intensities can be found in table 8.2. Mean intensities have been calculated as unweighed arithmetic mean and the errors were calculated with error propagation.

9. Results of Archaeomagnetic Dating

Archaeomagnetic dating for the sites was done in two steps. First, only the direction of the palaeofield was used to date the features and compare these results with the archaeological dating intervals, respectively. In a second step, the measured palaeointensities were used in combination with the field directions for dating in order to examine, if the additional data would lead to an improvement of the results.

The sites were dated with two different softwares. The first software used was RenDateModel v5523 (Lanos, 2004). The reference curve used for dating with palaeodirections was Austria2014 (Schnepp et al., 2015). For dating in combination with intensity data, no reference curve is yet available for Austria. Therefore the only available intensity reference curve, a curve from Western Europe, was used instead. It was provided by P. Lanos and is based on the data of Hervé et al. (2013) and Gómez-Paccard et al. (2012). As this reference curve's data mainly origins from sites in France and therefore far from the observed sites of this thesis, the results have to be reviewed critically even though the distance is smaller than the commonly accepted 1000 km (Casas and Incoronato, 2007). The input data were reduced to the appropriate reference sites, Radstadt (47.380 °N, 13.450 °E) for directions and Paris (48.859 °N, 2.340 °E) for intensities.

The second software was the Matlab tool archaeo_dating (Pavón-Carrasco et al., 2011). The input data for this tool do not need to be relocated to a reference site as this is done by the program. For the dating with the field direction data, the Austrian reference curve (Schnepp and Lanos, 2006) was used while the Western European reference curve (Gómez-Paccard et al., 2008) was used for dating with both directions and intensities.

After the detailed evaluation of each feature, all dating results are recapped in table 9.1 at the end of this chapter. For the dating with directional data only, the results of RenDateModel are given, because it provides the probabilities as percentages instead of just plotting the probability density functions like the Matlab tool. The results of archaeo_dating

differed only up to 3 years compared to RenDateModel and are therefore not shown. All features were dated over the complete time interval of 0 AD to 1800 AD to avoid the introduction of a bias of the results by limiting the interval to expected values. In this section, dating results are considered as "good" if they agree with the archaeological age.

The archaeological age of furnace SE1 lies in the range of the first half of the 4^{th} century AD (Cech, 2008; Schnepp, 2016). This age is supported by dendrochronological dating. With directional data only, the site was dated to the age interval of 160 AD - 349 AD with 95 % confidence as shown on the left side in figure 9.1. This time interval is considerably longer than the archaeological age estimate, but includes it. Trying to refine the result, the furnace was dated with both directions and intensity using the MSP-DSC intensity which is available (cf. table 8.2). The results of dating with declination, inclination and intensity with archaeo_dating and RenDateModel can be seen in figure 9.2 and on the right side of figure 9.1.

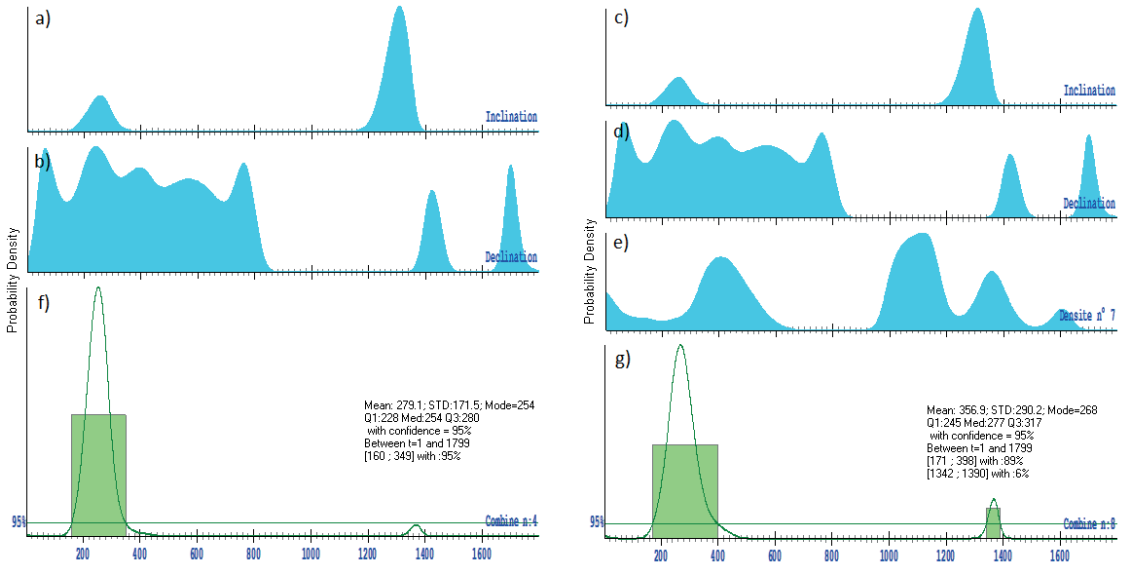

Figure 9.1.: Dating results of SE1 with RenDateModel using direction only (left) and full vector (right). Plotted versus time are probability densities of declination (a,c), inclination (b,d) and intensity (e) in arbitrary scale in blue and curves of combined probability densities for direction (f) and full vector (g) with corresponding time intervals in green.

Both softwares give similar but not exactly the same age intervals in regard to the probability density distribution (see table 9.1). While archaeo_dating's probability density function gives the interval 201 AD - 441 AD and a much smaller probability for the interval of 1322

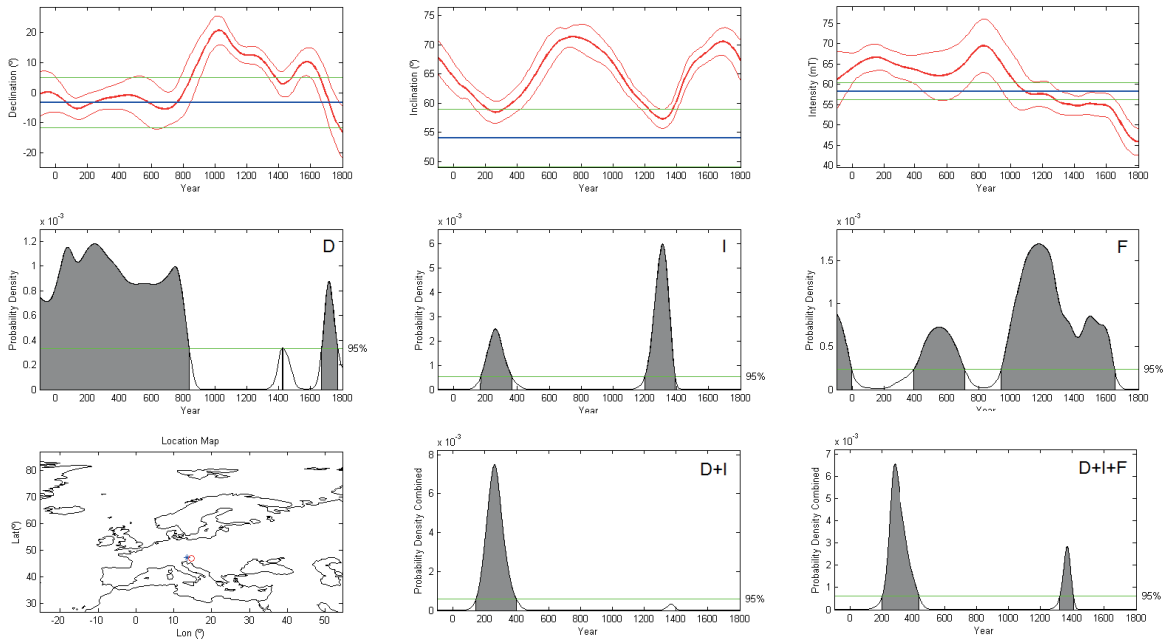

Figure 9.2.: Dating of SE1 with archaeo_dating. Upper row: Reference curves (see text) and error bands for declination, inclination and intensity versus time in red. Measured value in blue and 95% error margin in green. Middle row: Probability densities versus time of declination (D), inclination (I) and intensity (F). Lower row: Location of site on the left, combined probability densities of directional probability densities in the middle and combined probability density of directional and intensity probability densities on the right.

AD - 1407 AD, RendateModel dates the site to the interval of 171 AD - 398 AD with 98% confidence and the interval of 1342 AD - 1390 AD with 6%. There are also no big differences for the probability density distributions if they are compared to the result of archaeo_dating if the spherical model (Pavón-Carrasco et al., 2009) SHA.DIF.3k was used as a reference curve. The French intensity curve used with RenDateModel seems to result in almost the same values as the Western European curve of archaeo_dating.

Furnace SE4 was archaeologically dated to the period from the end of the 2^{nd} century to the beginning of the 3^{rd} century (Cech, 2008). The archaeomagnetic dating with directional data results provided three time intervals from 35 AD-493 AD with 91.8% confidence, as well as the intervals of 1401 AD - 1523 AD (1.2%) with rather low probability. Similar to the SE1 result, these two intervals show the ambiguity of archaeomagnetic dating and are caused by the fact that the directional curve has loops as well as ranges of declination and inclination, which can occur again centuries or even millenia later. For archaeological reasons, the medieval time interval can be excluded because the site was levelled already in the

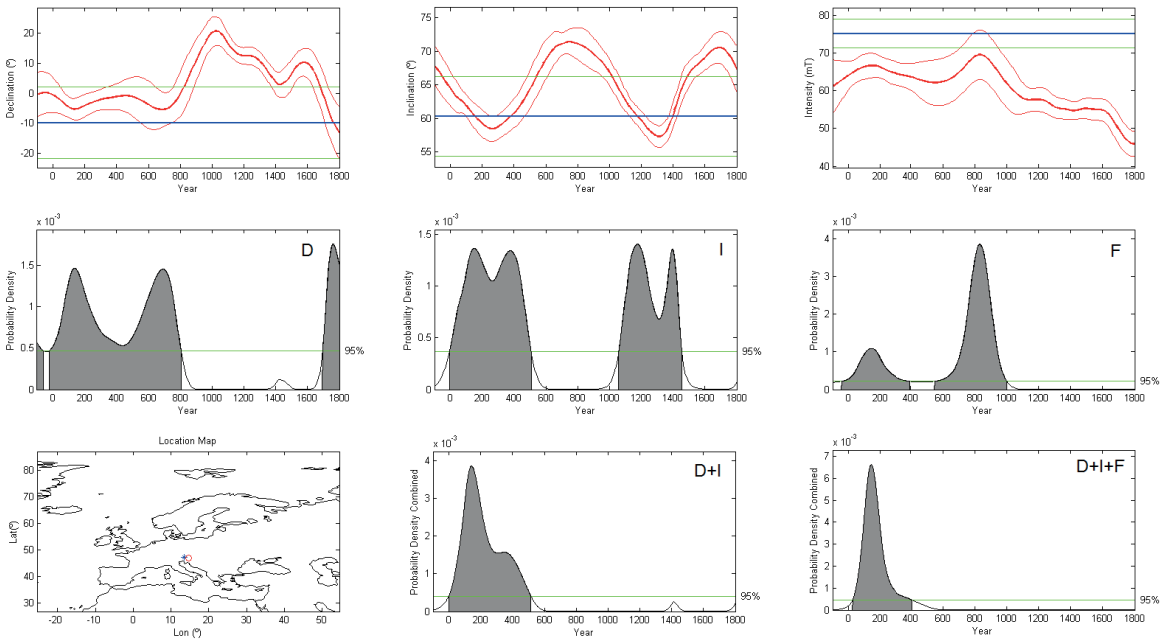

Figure 9.3.: Dating of SE4 with archaeo_dating. For explanation see figure 9.2.

12^{th}-13^{th} century (Cech, 2014). Due to the smoothing in the modelling process, compared to the modelled PSV curve, the measured intensity seems rather high (see figure 9.3, upper right diagram) but it has to be kept in mind, that the amplitude of variations could be considerably higher. The error bands shown in the figure give only the 95% probability confidence range. However, in combination with the directional data, the intensity data slightly improves the dating results to a dating interval of 26 AD - 480 AD gained from archaeo_dating (see figure 9.3) and a much shorter interval of 42 AD - 336 AD with 95% confidence gained from RenDateModel. For this feature, both programmes give similar results and there also seem to be no differences in the distribution of probability density.

As the oldest feature used in this thesis, furnace SE6 was archaeologically dated to the period from the 2^{nd} half of the 1^{st} century to the beginning of the 2^{nd} century (Cech, 2008). Using RenDateModel and the palaeofield direction, three dating intervals were found. The largest peak of the probability density function is associated with an interval of 29 AD - 188 AD (65.7%). However, two younger dating intervals of 337 AD - 536 AD with 26.3% confidence and 1408 AD - 1442 AD with 3% confidence are results, of which the latter can be excluded for the same archaeological reason as mentioned above. For SE6, intensities both from MSP-DSC and Thellier-Thellier experiments were available. As both experiments result in similar intensity values, an arithmetic mean intensity value of the both experiments

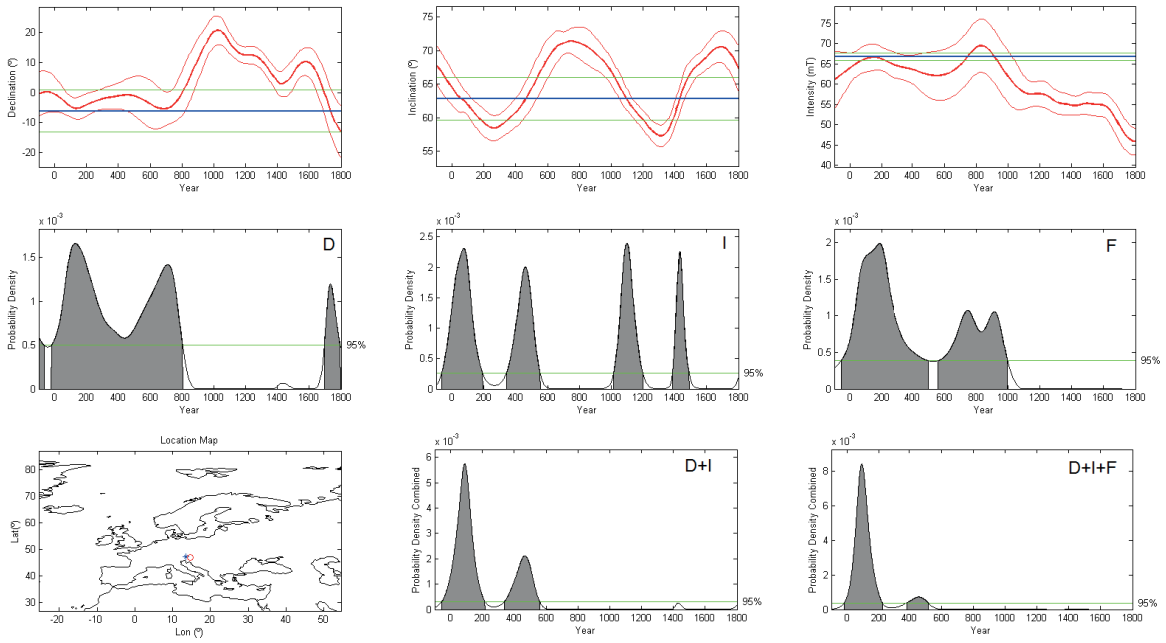

Figure 9.4.: Dating of SE6 with archaeo_dating. For explanation see figure 9.2.

was used for the dating (table 9.1). The error of the mean intensity was calculated with error propagation assuming a Gaussian distribution of the errors. Using this value, the probability density could be improved in both RenDateModel and archaeo_dating. The only significant probability density peak is now found at the dating interval of 20 BC - 221 AD with archaeo_dating as shown in figure 9.4 and 25 AD - 205 AD with 88% confidence with RenDateModel. A second dating interval was given by archaeo_dating in the range of 383 AD - 518 AD and in RenDateModel with 451 AD - 545 AD (6.2%).

The first feature of Thunau addressed here in this thesis were the ceramic shards found in oven TH2. According to them, the archaeological age of the associated oven is 950 AD - 1000 AD (Obenaus, 2015). A similar, but wider interval of 859 AD - 979 AD with 66.3% confidence as well as a second interval of 1585 AD - 1640 AD with 28.9% confidence were the results of dating with the palaeofield direction (table 9.1). The younger interval around the beginning of the 17^{th} century is found for all Thunau features. From the reference curves for declination and inclination in figure 9.5, it can clearly be seen that the reason for this is the similarity of declinations and inclinations during the 9^{th} and 17^{th} century. For archaeological reasons in all cases these younger intervals (table 9.1) can be excluded and they are not discussed further. In contrast, the intensity reference curve shows different values for these time periods and therefore, the use of the measured intensities was expected

to refine the dating results. Despite the large error margin of the MSP-DSC experiment due to the small specimen number, it was possible to refine the dating results. The software archaeo_dating resulted in intervals of 860 AD - 975 AD and 1552 AD - 1653 AD with the probability density being slightly larger for the older interval. RenDateModel resulted in the intervals of 906 AD - 982 AD with 38.2% and 1579 AD - 1644 AD with 56.8%.

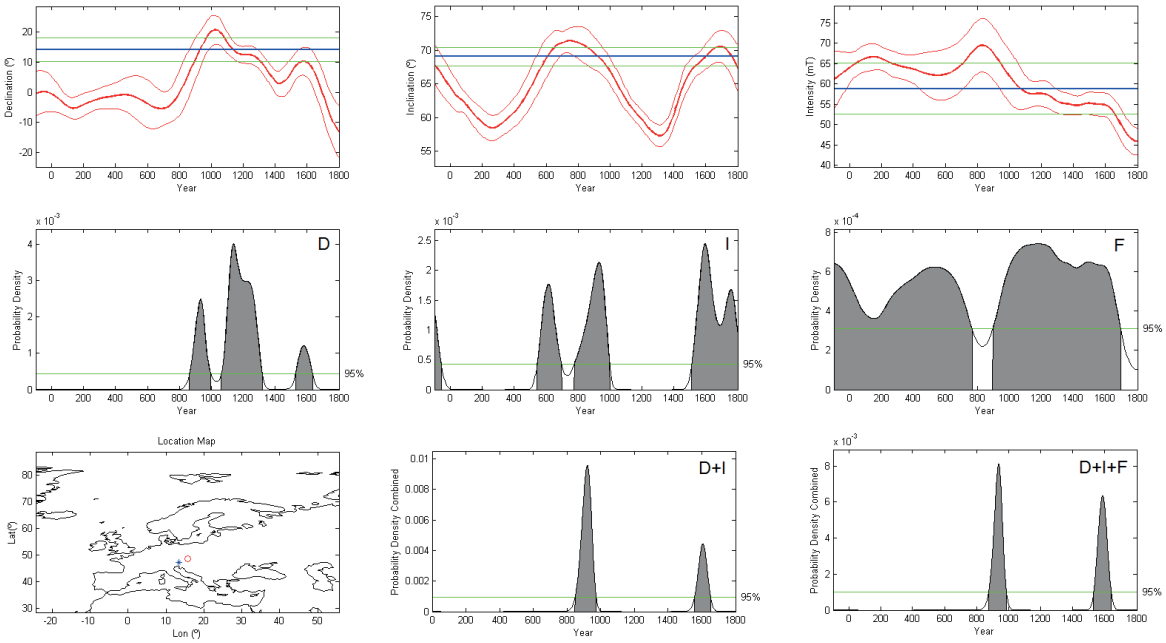

Figure 9.5.: Dating of TH2 with archaeo_dating. For explanation see figure 9.2.

The ceramic shards associated with oven TH5 have been archaeologically dated to 950 AD - 1000 AD (Obenaus, 2015). Again, dating with directional data resulted in two dating intervals of 859 AD - 1006 AD (76.8%) and 1566 AD - 1639 AD (18.2%). For this feature, the results of MSP-DSC and Thellier experiments differed too much to allow the calculation of a mean value. Instead two dating attempts were conducted. One of the two TH5 specimens (TH5T5B2) showed a Thellier intensity similar to the intensity from the MSP-DSC experiment. Therefore a mean value of these two was used in a dating attempt (see table 9.1). The second TH5 specimen used in the Thellier experiment (TH5TH3B2) gave a better quality result than the first and was therefore used for an alternative dating attempt. Both dating results vary significantly. This can be seen clearly at the probability densities plotted by RenDateModel in figure 9.6. The mean value of the MSP-DSC and the Thellier intensity was 54.225μT ($\pm$ 6.577μT). The resulting dating intervals of 930

AD - 1008 AD (24.4 %) and 1542 AD - 1650 AD (70.6%) are again very similar to the intervals of 882 AD - 1004 AD and 1526 AD - 1664 AD gained from archaeo_dating. In contrast, the resulting dating intervals of 858 AD - 941 AD (95.2%) by RenDateModel and 835 AD - 959 AD by archaeo_dating were significantly refined when using the intensity value of the second intensity result of the Thellier-Thellier experiment, but do not overlap with the archaeological age interval any more.

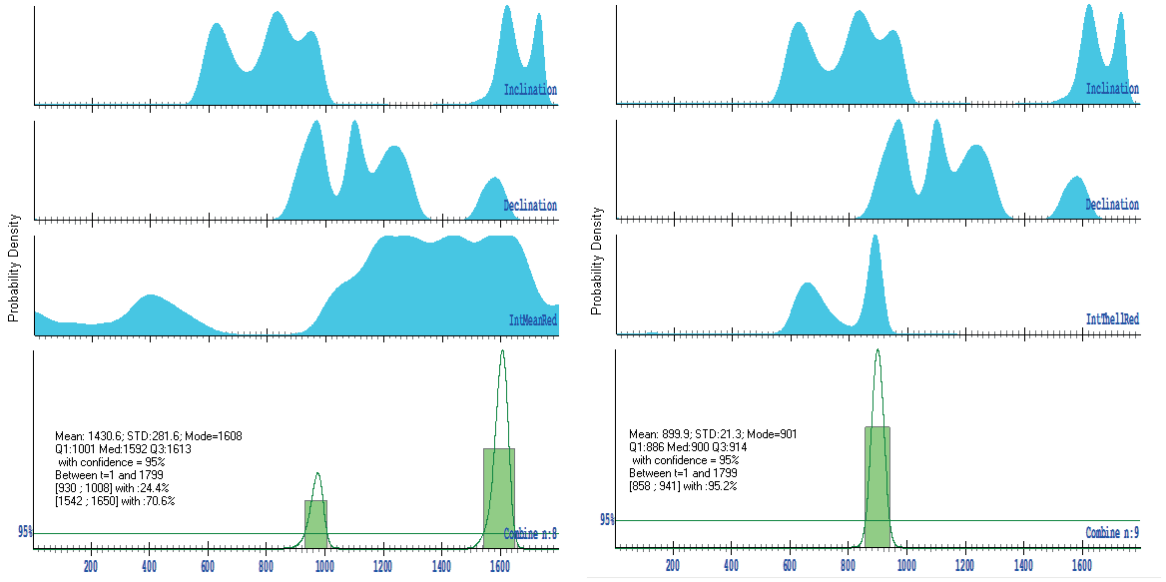

Figure 9.6.: Dating of ceramic shards TH5 with a mean value of a Thellier experiment and the MSP-DSC measurement (left) and a single Thellier intensity result (right) Probability densities of declination, inclination and intensity are shown in blue and the combined probability density as a green curve. Corresponding time intervals are also shown in green.

The shards found in oven TH9 were archaeologically dated to the interval of 900 AD - 1000 AD (Obenaus, 2015). Dating of the oven with directional data led to a similar but wider interval of 887 AD - 1097 AD with 72.7% confidence and a second interval of 1507 AD - 1600 AD with 22.3%. The behaviour of the specimens from the shards of this feature during the intensity experiments was the same as the behaviour of those of TH5. Again, one Thellier experiment and the MSP-DSC experiment resulted in similar values and the mean intensity of 42.27μT ($\pm$ 6.42μT) was used to date the feature. Dating with this intensity value results in the dating intervals of 1038 AD - 1077 AD (with 3.3%) and 1484 AD - 1615 AD (with 91.8%) with RenDateModel. On the contrary, the use of archaeo_dating still resulted in a slightly higher probability density for the dating interval of 954 AD - 1113

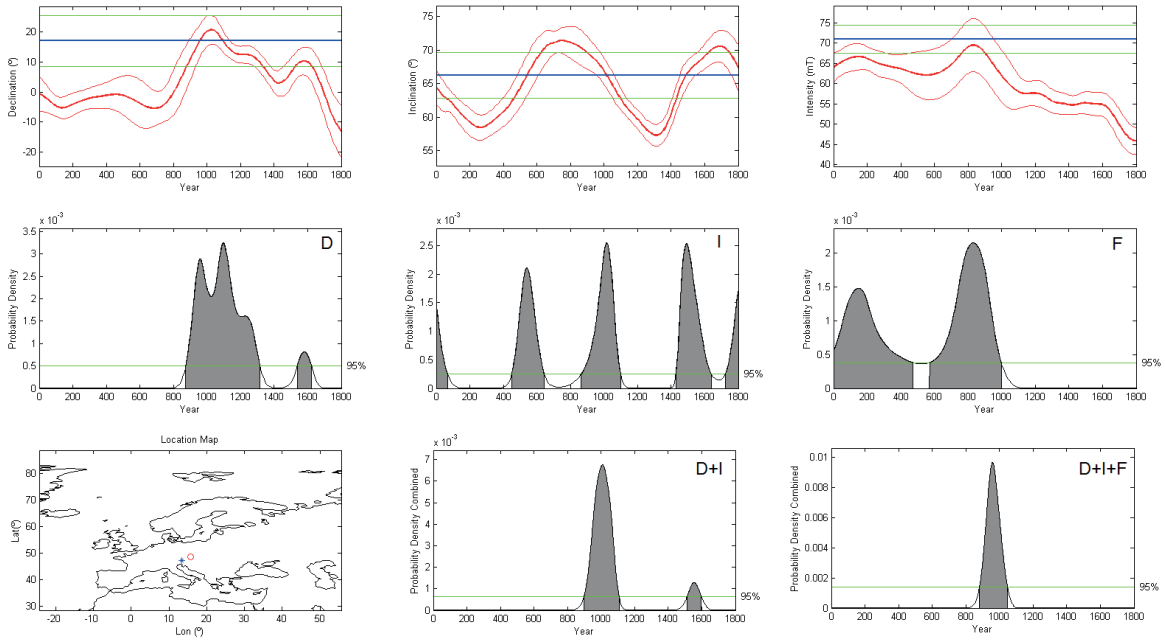

Figure 9.7.: Dating of TH9 with archaeo_dating. For explanation see figure 9.2.

AD than for the interval of 1486 AD - 1631 AD. However, as for feature TH5 the dating with directional data was again improved when using the single value gained in the Thellier experiment of the specimen TH9S6B2. Here, the resulting dating intervals are 881 AD - 1048 AD from archaeo_dating, shown in figure 9.7, and 873 AD - 1037 AD with 95.1% confidence from RenDateModel. In this case it seems that one Thellier experiment and the MSP-DSC experiment underestimate the ancient field considerably. The Thellier experiment showed a strongly concave-up line and deviated pTRM-checks (see appendix A) while the MSP intensity was only based on 6 data points, one indicating strong alteration and the result has a low quality. The tentative dating approach leading to obviously wrong results support the view that such Thellier as well as MSP data are unreliable.

For oven THP, archaeologically dated to the period between 850 AD and 950 AD (Obenaus, 2015), dating with the direction of the field vector resulted in a dating interval of 1595 AD - 1673 AD with 86% and another interval of 819 AD - 891 AD with 8.3%. Here, both intensity results of the Thellier experiment show very similar values and a mean intensity of 61.45μT ($\pm$ 3.22μT) was used as well as the higher intensity value from the MSP-DSC experiment. Both intensity values improve the dating results significantly with archaeo_dating, while RenDateModel only improves the dating with the MSP-DSC intensity. With the MSP-DSC intensity, RenDateModel gives a dating interval of 803 AD - 966 AD

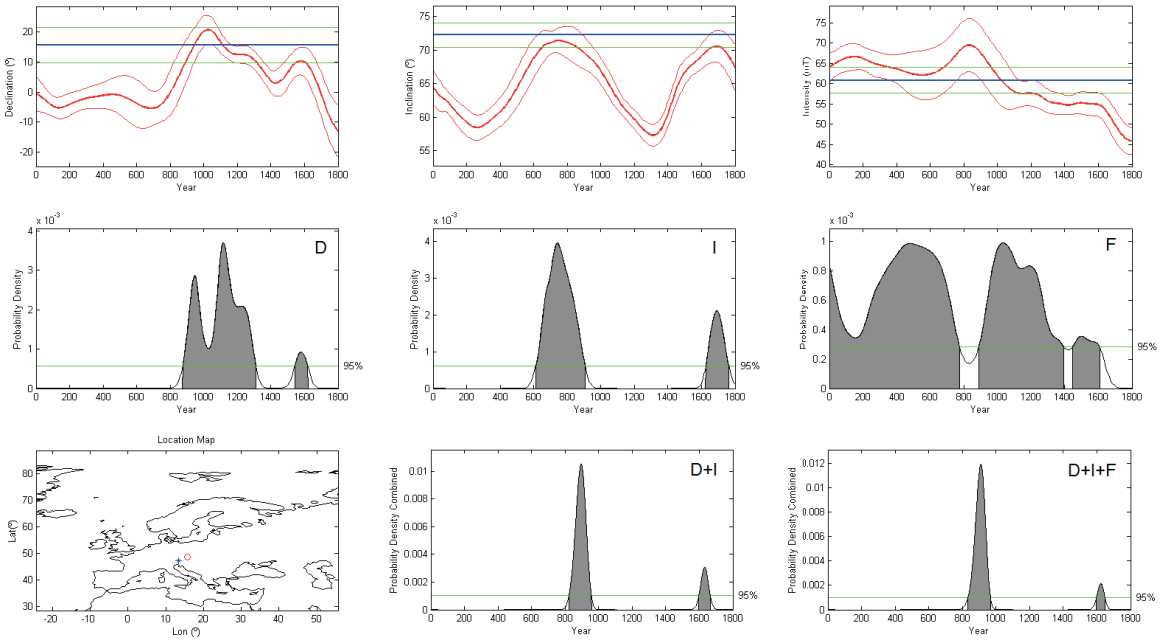

Figure 9.8.: Dating of THP with archaeo_dating. For explanation see figure 9.2.

(95.1%) while archaeo_dating dates the site to 826 AD - 944 AD. With the Thellier intensity, the resulting intervals are 833 AD - 967 AD and 1598 AD - 1648 AD for archaeo_dating, as shown in figure 9.8, and 956 AD - 976 AD (3.9%) as well as 1597 AD - 1659 AD (91.2%) with RenDateModel. The use of the French intensity curve with RenDateModel seems to be less beneficial for this feature in comparison to the Western Europe curve. Furthermore, the dating attempt shows, that it would be useful to do the dating taking a priori archaeological information into account. Due to the spectrum of finds (Obenaus, 2015) the settlement was abandoned already in the 13^{th} - 14^{th} century. Accordingly, the modern age intervals provided by the dating procedure would not be present when the interval would be restricted to e.g. 0 - 1300 AD.

The dating attempt of oven THT with only directional data and the resulting intervals of 820 AD - 866 AD (23.8%) and 1598 AD - 1663 AD (71.3%) differed from the archaeological dating interval of 900 AD - 1000 AD (Obenaus, 2015). The intensities were again similar for both specimens of the Thellier experiment and MSP-DSC gave a different, in this case a smaller, intensity value. Therefore, for THT there were again two dating attempts with both the intensity of the MSP-DSC experiment and the mean Thellier intensity of 67.57μT ($\pm$ 1.16μT). Here, the dating with the MSP-DSC intensity resulted in dating intervals of 1603 AD - 1658 AD (95.3%) for RenDateModel and 879 AD - 917 AD as well as 1557 AD

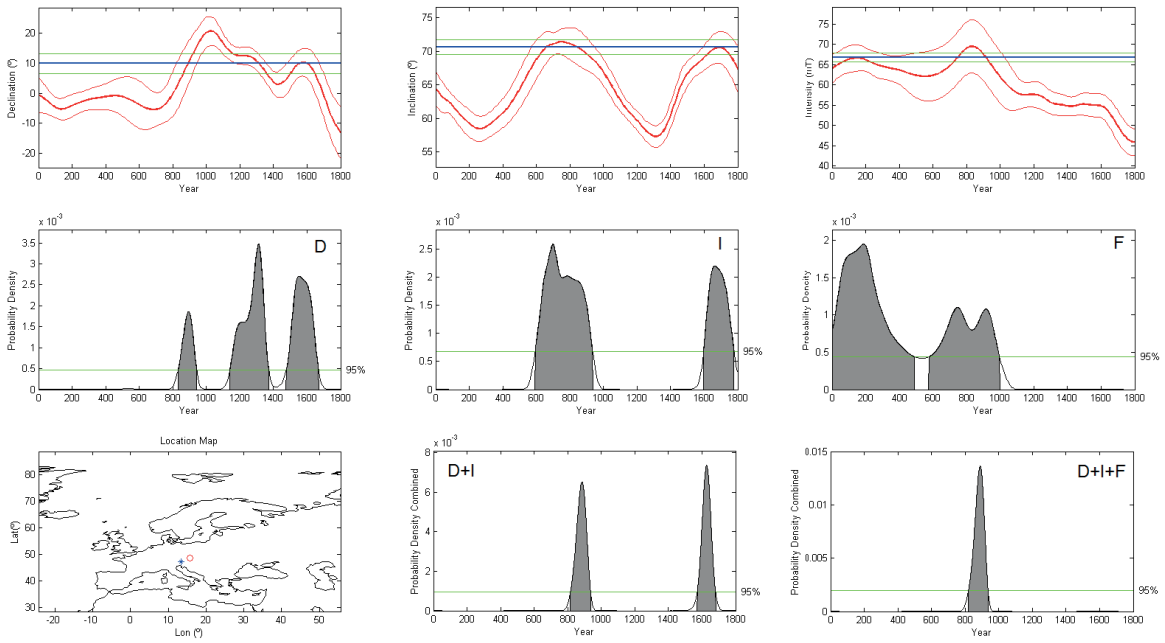

Figure 9.9.: Dating of THT with archaeo_dating. For explanation see figure 9.2.

- 1692 AD for archaeo_dating. While the older interval obtained from the Matlab tool fitted well to the archaeological age, the main fraction of the probability density distribution was found at the younger interval. A much improved result was gained from the mean intensity of the Thellier experiments. While RenDateModel gave the dating intervals 558 AD - 609 AD (15.5%) and 901 AD - 968 AD (79.7%), archaeo_dating gave the dating interval of 820 AD - 936 AD as result (see figure 9.9).

Oven THU, with an archaeological dating interval of 900 AD - 1000 AD (Obenaus, 2015), could be relatively well dated with directional data to intervals of 837 AD - 986 AD (with 62.2%) and 1543 AD - 1644 AD (with 32.8%). Unlike the ovens of THP and THT, the intensity values of both experiments are similar for THU. Therefore the mean intensity value of 62.0μT ($\pm$ 2.0μT) was used. Dating with this intensity improved the result when using archaeo_dating to dating intervals of 852 AD - 1005 AD and 1530 AD - 1625 AD, as seen in figure 9.10. The French intensity reference curve and RenDateModel resulted in an even smaller interval of 941 AD - 1013 AD (95.1%). This demonstrates that a well defined intensity value supported by two methods can help to improve dating considerably.

Like oven THU, oven THX was well dated with the direction of the field vector and resulting dating intervals of 861 AD - 995 AD (with 76.6%) and 1579 AD - 1637 AD (with 18.5%)

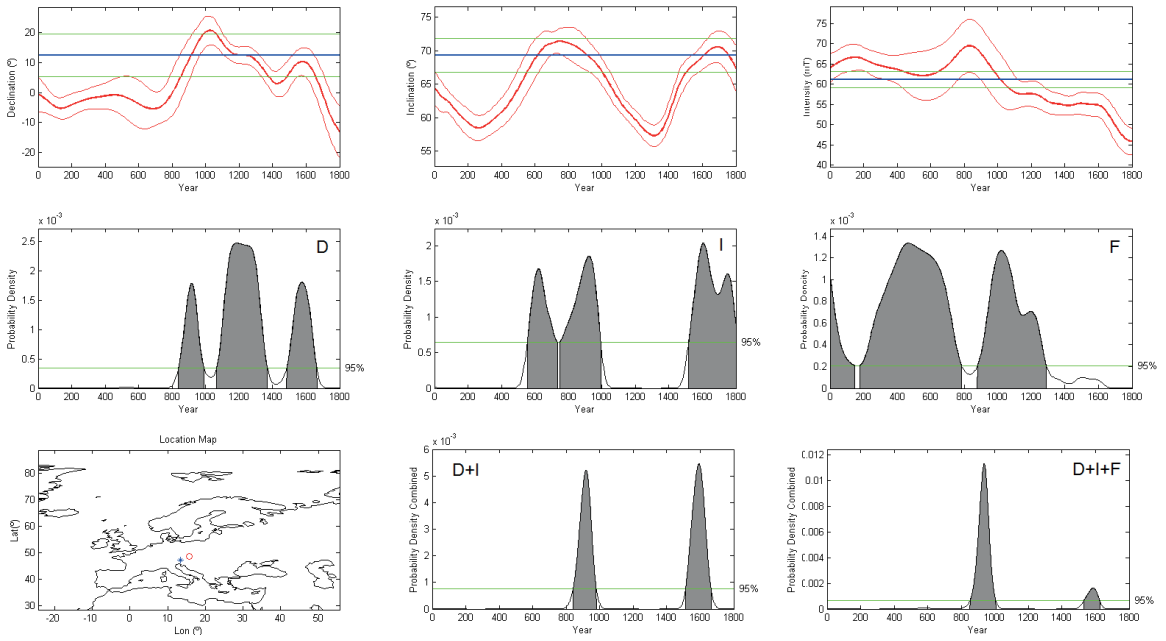

Figure 9.10.: Dating of THU with archaeo_dating. For explanation see figure 9.2.

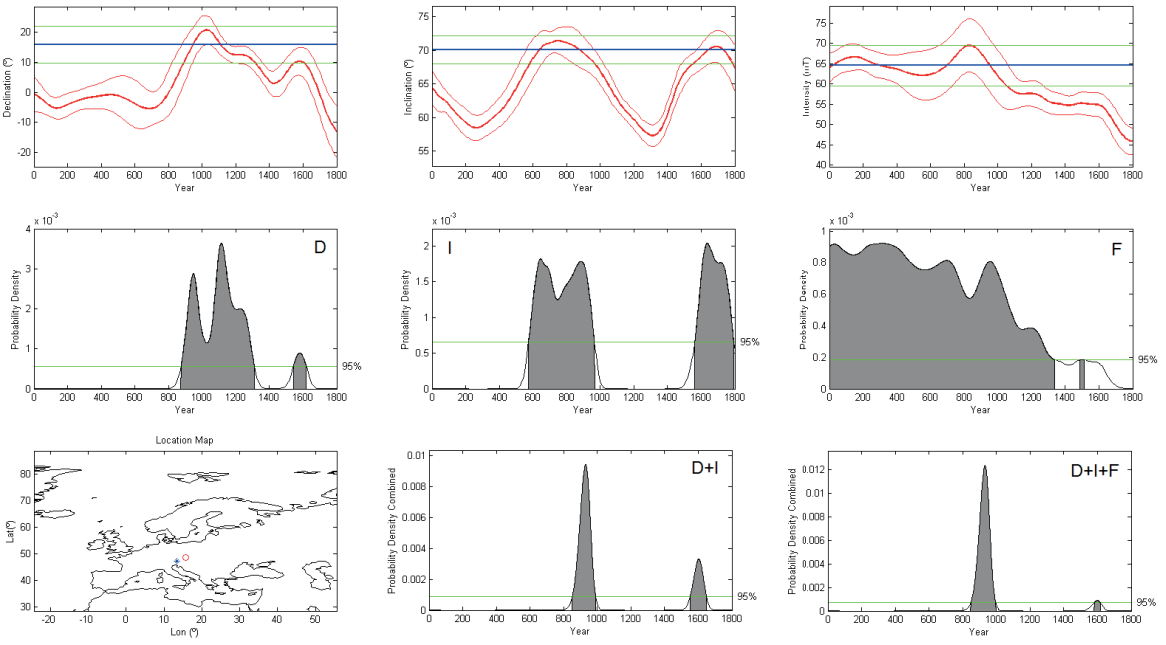

Figure 9.11.: Dating of THX with archaeo_dating. For explanation see figure 9.2.

in comparison to the archaeological dating interval of 850 AD - 950 AD (Obenaus, 2015). Again, it was possible to calculate a mean intensity value from the intensities gained from

both experiments. This mean intensity of 65.4μT ($\pm$ 5.0μT) has a large error margin due to the large error of the MSP-DSC intensity. However, RenDateModel and archaeo_dating both gave different intervals and distributions of probability density. While the resulting intervals were 848 AD - 996 AD and 1581 AD - 1617 AD for archaeo_dating, as shown in figure 9.11, the intervals of RenDate Model were 885 AD - 1002 AD (with 94.7%) and 1609 AD - 1612 AD (with 0.3%).

The archaeological dating interval of oven THY is the same as the interval of oven THX (Obenaus, 2015), while the stratigraphy suggests THY to be older than THX. Dating with directional data resulted in dating intervals of 806 AD - 946 AD (with 54.2%) and 1564 AD - 1664 AD (with 10.9%). These intervals are about the same size as the ones of THX and are shifted by roughly -50 years as expected from the stratigraphic position. Here, MSP-DSC and the both Thellier intensities were again different. A mean intensity of 69.86μT ($\pm$ 1.4μT) could be calculated for the two Thellier intensities. The dating intervals for the dating with the MSP-DSC intensity were 1569 AD - 1657 AD (with 95.2%) for RenDateModel, and 906 AD - 921 AD and 1497 AD - 1617 AD for archaeo_dating with only a very low probability density for the older interval. A different result was obtained using the mean value of the Thellier intensities. The resulting intervals were 875 AD - 972 AD (with 95.1%) for RenDateModel and 809 AD - 940 AD for archaeo_dating, shown in figure 9.12. Comparing these intervals with the intervals of THX, the age sequence of the ovens as suggested by stratigraphy seems to be met by the measurements.

Only the direction of the palaeofield was available to date oven THZ. Its archaeological dating interval is again 850 AD - 950 AD (Obenaus, 2015) and it should be older than THY, according to the stratigraphy. The resulting archaeomagnetic dating intervals were 791 AD - 1005 AD (with 52.3%) and 1483 AD - 1679 AD (with 42.7%). Although the dating interval starts earlier, it is not possible to confine the dating with this data alone. The sequence THX, THY and THZ is an example of the benefits of using archaeointensities in combination with the direction of the field vector to gain better results.

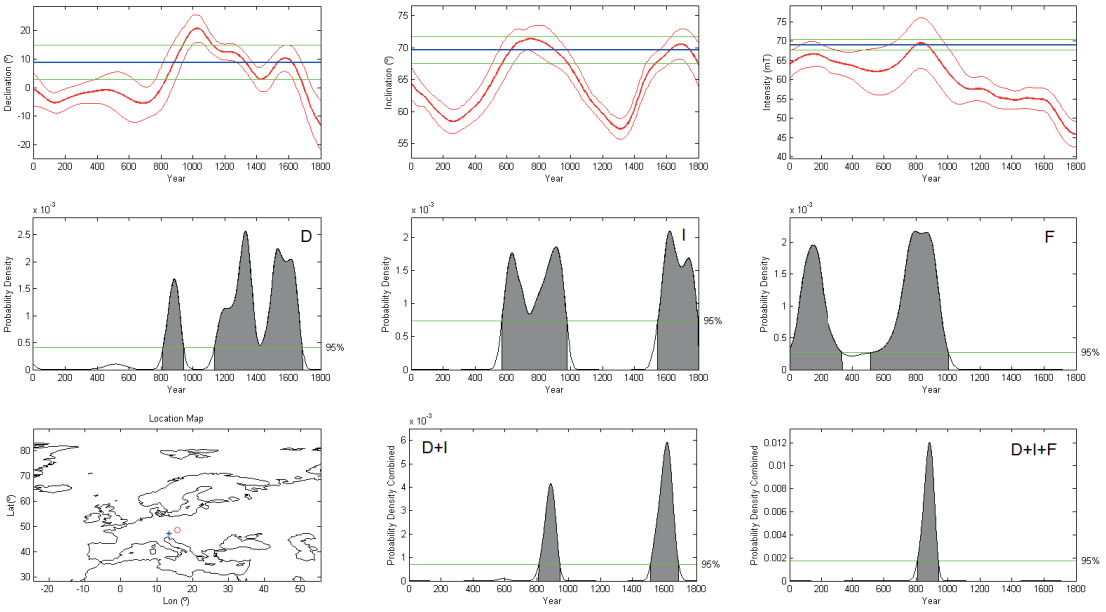

Figure 9.12.: Dating of THY with archaeo_dating. For explanation see figure 9.2.

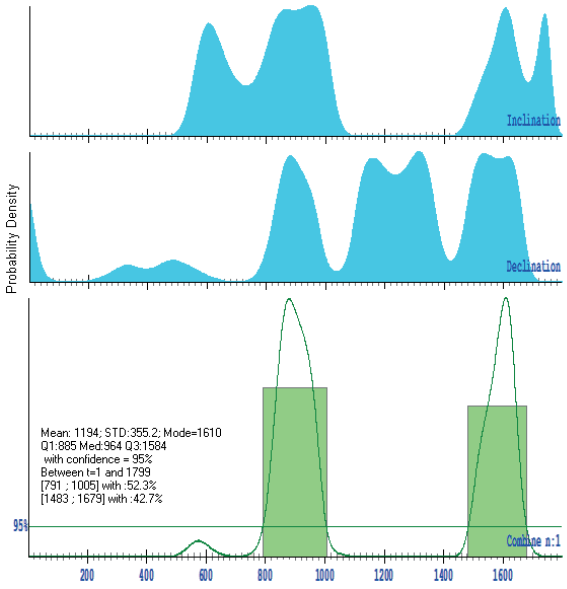

Figure 9.13.: Dating of THZ. Probability densities of declination and inclination in blue and combined probability density as green line. Corresponding time intervals are shown in green.

Site	$Age_{arch.}$ (years AD)	$Age_{dir.}$ (years AD)	Intensity Type	Age_{MT} (years AD)	Age_{RD} (years AD)
SE1	300-350	**[160-349]**,95.1%	MSP-DSC	**[201-441]**; *[1322-1407]*	**[171-398]**,89%; *[1342-1390]*,6%
SE4	170-230	**[35-493]**,91.8% *[1401-1523]*,1.2%	MSP-DSC	**[26-480]**	**[42-336]**,95%
SE6	50-115	**[29-188]**,65.7% *[337-536]*,26.3%	$Mean_{M-T}$	**[-20-221]**; *[383-518]*	**[25-205]**,88%; *[451-545]*,6.2%
TH2	950-1000	**[859-979]**,66.3% *[1585-1640]*,28.9%	MSP-DSC	**[860-975]**; *[1552-1653]*	**[906-982]**,38.2%; *[1579-1644]*,56.8%
TH5	950-1000	**[859-1006]**,76.8%	$Mean_{M-T}$	*[882-1004]*; *[1526-1664]*	*[930-1008]*,24.4%; *[1542-1650]*,70,6%
		[1566-1639],18.2%	Thellier	**[835-959]**	**[858-941]**,95.2%
TH9	900-1000	**[887-1097]**,72.7%	$Mean_{M-T}$	*[954-1113]*; *[1486-1631]*	*[1038-1077]*,3.3%; *[1484-1615]*,91.8%
		[1507-1600],22.3%	Thellier	**[881-1048]**	**[873-1037]**,95.1%
THP	850-950	**[819-891]**,8.3%	MSP-DSC	**[826-944]**	**[803-966]**,95.1%
		[1595-1673],86%	$Mean_{T-T}$	*[833-967]*; *[1598-1648]*	*[956-976]*,3.9; *[1597-1659]*,91.2% %
THT	850-950	**[820-866]**,23.8%	MSP-DSC	*[879-917]*; *[1557-1692]*	*[1603-1658]*,95.3%
		[1598-1663],71.3%	$Mean_{T-T}$	**[820-936]**	*[558-609]*,15.5%; **[901-968]**,79.7%
THU	900-1000	**[837-986]**,62.2% *[1543-1644]*,32.8%	$Mean_{M-T}$	**[852-1005]**; *[1530-1625]*	**[941-1013]**,95.1%

Table 9.1.: Dating results, part 1. Site; archaeological age; age determined with directional data only (RenDateModel); intensity types: MSP-DSC or Thellier intensity or mean intensities of M-T (MSP-DSC & Thellier value) and T (Thellier & Thellier value); Age determined with Matlab Tool archaeo_dating; Age determined with RenDateModel. Bold values are the preferred results.

Site	$Age_{arch.}$ (years AD)	$Age_{dir.}$ (years AD)	Intensity Type	Age_{MT} (years AD)	Age_{RD} (years AD)
THX	850-950	**[861-995]**,76.6% *[1579-1637]*,18.5%	$Mean_{M-T}$	**[848-996]**; *[1581-1617]*	**[885-1002]**,94.7%; *[1609-1612]*,0.3%
THY	850-950	**[806-946]**,54.2%	MSP-DSC	*[906-921]*; *[1497-1617]*	*[1569-1657]*,95.2%
		[1564-1664],40.9%	$Mean_{T-T}$	**[809-940]**	**[875-972]**,95.1%
THZ	850-950	**[791-1005]**,52.3% *[1483-1679]*,42.7%	x	x	x

Table 9.2.: Dating results, part 2. Site; archaeological age; age determined with directional data only (RenDateModel); intensity types: MSP-DSC or Thellier intensity or mean intensities of M-T (MSP-DSC & Thellier value) and T-T (Thellier & Thellier value); Age determined with Matlab Tool archaeo_dating; Age determined with RenDateModel. Bold values are the preferred results.

Site	Mean Age$_{Arch}$ (years AD)	±error (years)	Mean Age$_{Dir}$ (years AD)	±error MT/RD (years)	Mean Age$_{FullVec}$ (years AD)	±error MT/RD (years)
SE1	325	25	254.5	94.5	321/284.5	120/113.5
SE4	200	30	264	229	253/189	227/147
SE6	82.5	32.5	108.5	79.5	100.5/115	120.5/90
TH2	975	25	919	60	943/944	61/38
TH5	975	25	932.5	73.5	897/899.5	62/41.5
TH9	950	50	992	105	964.5/955	83.5/82
THP	900	50	955	36	885/884.5	59/81.5
THT	900	50	943	23	878/934.5	58/33.5
THU	950	50	911.5	74.5	928.5/977	76.5/36
THX	900	50	928	67	922/943.5	74/58.5
THY	900	50	876	70	874.5/923.5	65.5/48.5
THZ	900	50	898	107	x /x	x/x

Table 9.3.: Comparison of archaeological and archaeomagnetic age intervals; Feature name, mean age of archaeological dating interval (Cech, 2008; Obenaus, 2015) and error, mean age of dating with directions only and error, mean age of dating with full vector information with archeo_dating/RenDateModel and error.

10. Discussion of Dating Results

With the exception of TH8, where no acceptable intensities could be determined, the dating results of all features support the archaeological age (table 9.1). As two softwares and different PSV reference curves were used for dating, the results are discussed in this section under this point of view.

As a first step, the results of dating with only directional data with archaeo_dating and the directional reference curve Austria2006 (Schnepp and Lanos, 2006) was compared to the results of dating with directional data and RenDateModel with the same reference curve to compare the results of both softwares. The directions used for dating had to be relocated manually to Radstadt for the use in RenDateModel, while archaeo_dating relocated all data points automatically. As shown with the yellow dots in figure 10.1, both softwares give the same dating periods with small differences of up to 3 years.

Because a newer directional curve for Austria (Schnepp et al., 2015) was also available for RenDateModel, the results of using this curve (and RenDateMmodel) have been compared to the results when the curve Austria2006 was used with archaeo_dating (blue diamonds in figure 10.1). The results are very similar and plot close to a regression line with a slope 1. However, the results of both curves are not exactly the same. The reason for this are differences between the curves of Austria2006 and Austria2014. An improved algorithm was used for Austria2014 as well as new data points obtained from Thunau am Kamp. Therefore, the error band is smaller as for Austria2006 and deviations between results are large in the early medieval period.

Another comparison was done for both softwares, dating with the combination of directions and intensities. As described in chapter 9, for archaeo_dating the Western European reference curve was used, containing curves for directions (Schnepp and Lanos, 2006) and intensities (Gómez-Paccard et al., 2008), while RenDateModel used the newer Austria2014 directionsl reference curve and the intensity curve, provided by P. Lanos and based on the data of

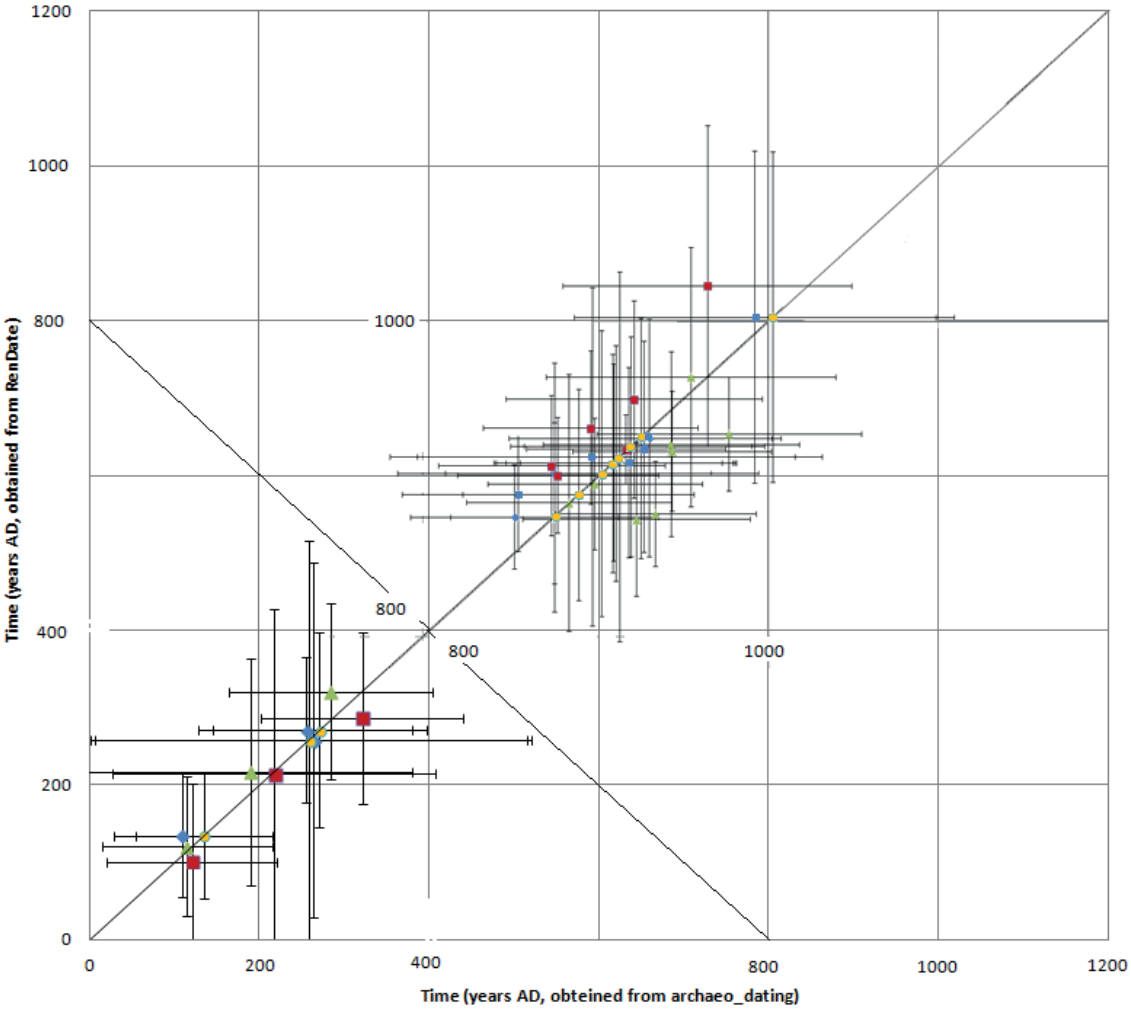

	x-axis			y-axis		
Symbol	Software	Curve	Param.	Software	Curve	Param.
●	RenDateModel	AUT2006	D+I	RenDateModel	AUT2006	D+I
◆	RenDateModel	AUT2006	D+I	archaeo_dating	AUT2014	D+I
▲	archaeo_dating	W-EU	D+I+F	RenDateModel	W-EU+SL2005	D+I+F
■	archaeo_dating	ShaDif3k	D+I+F	archaeo_dating	W-EU	D+I+F

Figure 10.1.: Plot of resulting age intervals of both analysis tools against each other. The straight line symbolises x=y.

Hervé et al. (2013) and Gómez-Paccard et al. (2012), calculated with the same newer algorithm as Schnepp et al. (2015). The measured values of directions were relocated to Radstadt and the values of intensities to Paris for the use with RenDateModel, while archaeo_dating again used the internal relocation. As shown with green triangles in figure 10.1, the comparison of these results show a small systematic deviation and scatter around

the trendline of x equals y. For the features of Semlach, they plot above the trendline, while some of the features of Thunau plot below.

To further discuss the resulting age intervals, a third comparison was conducted. This time the results of using the Western Europe reference curve and archaeo_dating were compared to the results of archaeo_dating using the spherical cap model SHA.DIF.3k. The results are plotted in figure 10.1 as red squares. Again, small systematic deviations could be found and the scatter of the data points was larger than the scatter of data from the other comparisons of the tools and curves. This time, values of Thunau plot above the trendline. The differences here can be explained by the different PSV models the curves are based on. Contrary to the other curves used above, data does not need to be relocated manually or internally when the curve SHA.DIF.3k is used. However, this curve is also based on an older database from Pavón-Carrasco et al. (2009).

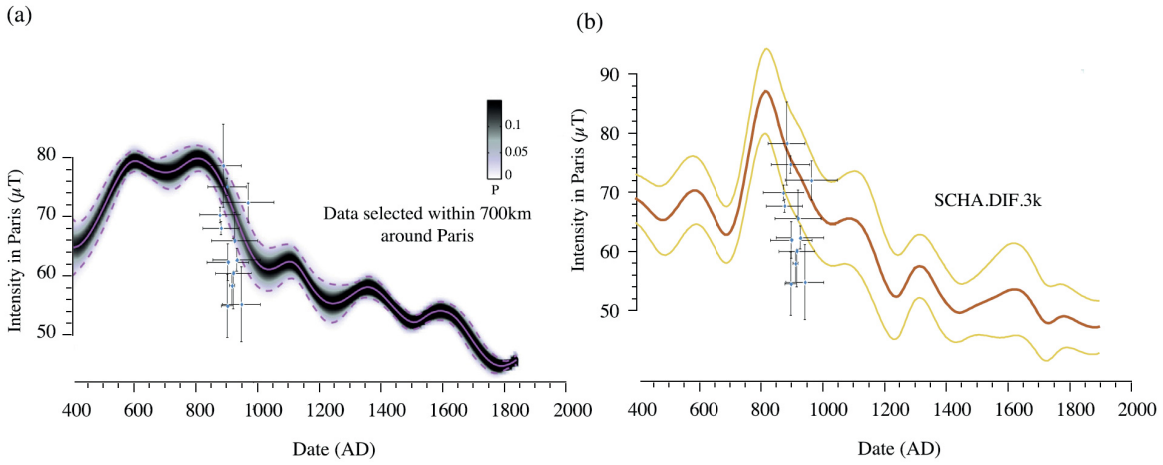

Figure 10.2.: Plot of intensity data of Thunau features in comparison to (a) the newest version of the French intensity reference curve (Genevey et al., 2016) and (b) the SHA.DIF.3k reference curve (Pavón-Carrasco et al., 2009). Modified after (Genevey et al., 2016).

Finally, figure 10.2 shows the intensity results plotted versus the newest version of the French intensity PSV curve (Genevey et al., 2016) and versus SCHA.DIF.3k (Pavón-Carrasco et al., 2009). As Genevey et al. (2016) published this curve only for the time interval between 400 AD and 1850 AD, only the intensities from the Thunau features are plotted here because the Semlach features would not fit to this curve due to their higher age. Although the curves are considerably different, they agree in a strong decrease of the intensity between

800 and 1000 AD. The results from Thunau follow this trend. Some of the results lie below the curve. Still, they might not be underestimated and only differ from the curve due to the curve's smoothing.

11. Conclusion

Three new archaeomagnetic directions could be determined for the ovens THX, THY and THZ from Thunau am Kamp. Although the direction of oven THZ shows a smaller precision parameter and a larger α_{95} radius as THX and THY, which was probably caused by flattening of the oven due to levelling of the area after the village was abandoned, all three directions can be considered to be reliable. All three directions plot to a reasonable time interval of the PSV reference curve and the stratigraphical sequence of the features can be supported for THX and THY, while the α_{95} radius of THZ is too large to confirm the oven's spot in the stratigraphic sequence of the three ovens. The directions are in very good agreement with the archaeomagnetic secular variation reference curve.

In addition to the three directions, it was possible to determine 11 new intensities from 19 Thellier experiments and 12 MSP-DSC measurement series from 13 features, including three furnaces from Semlach/Eisner as well as five ovens and three sets of ceramic shards associated to ovens from Thunau am Kamp. For the ceramic shards of oven TH8, it was neither possible to obtain intensities from the Thellier experiments, nor from the MSP-DSC series. There is also no intensity from the oven THZ because there was not enough material left to use for intensity measurements after the determination of the field direction. Comparisons with other published results of MSP-DSC experiments (e.g. Monster et al., 2015) show, that the successful MSP-DSC experiments of this thesis show good correlation coefficients and a high number of used specimens. The Thellier experiments show good results for specimens of the features THY, THU, THT as well as one specimen of SE6. Acceptable results of the Thellier experiments were found for the features TH5, TH9, THP and THX, while the measurements of both specimens of feature TH8 as well as one specimen of SE6 did not satisfy the criteria set in the ThellierTool and were refused. The obtained archaeointensities agree well with the intensity reference curve from France (Genevey et al., 2016).

The new data were used to date the features. The features of THX, THY and THZ were dated once with directional data only and another time with full vector information. The already published directional data for all other features (Schnepp, 2016; Schnepp et al., 2015; Schnepp, 2017) were also used to date these features as well as the full vector information containing these directions and the intensities determined in this thesis. The datings were carried out with the Western European PSV curve (Gómez-Paccard et al., 2008) and the software archeo_dating (Pavón-Carrasco et al., 2009) as well as the directional PSV curve of Austria (Schnepp et al., 2015) and the intensity reference curve provided by P. Lanos, based on Hervé et al. (2013) and Gómez-Paccard et al. (2012) with the software RenDateModel (Lanos, 2004).

It was possible to refine the age intervals from dating with directional data for the features SE4, TH2, TH5, TH9, THU, THX and THY when full vector information was used. All obtained age intervals overlap with the age intervals, that were archaeologically dated, but only for features THT, THU and THX the archaeological intervals were refined. The interval lengths for the other features, dated with full vector information, are a bit larger than the intervals of the archaeological age intervals. The archaeomagnetic ages can confirm the archaeological ages as an independent approach. As the new archaeomagnetic data origins from archaeologically well dated features, they can be used together with other archaeomagnetic data from the area for the improvement of existing directional PSV curves and provide important data for an intensity PSV curve of central Europe.

Acknowledgements

This Thesis was funded by the Austrian Science Fund (FWF): P23295_N21. I would like to extend my gratitude to Brigitte Cech and Martin Obenaus for kindly providing the samples of the furnaces of Semlach and the pottery shards of Thunau. Further, I thankfully acknowledge the support of Yvonne Fleischhacker, who accompanied and assisted me during the sampling trip to Thunau. I would also like to thank Roman Leonhardt for providing the MSP-tool as well as Philippe Lanos for providing an intensity reference curve. Finally, I would like to express my sincerest gratitude to my supervisor Elisabeth Schnepp for providing rock magnetic, directional data and MSP-DSC data for THP and THU, various images as well as the interesting and challenging assignment, her supervision and help in the field as well as in the lab and many interesting and helpful discussions.

Bibliography

Y. Arai, T. Nagata, and K. Momose. Secular variation of the geomagnetic total force during the last 5000 years. *Journal of Geophysical Research*, (68):5277–5281, 1963.

C.M. Batt. The British Archaeomagnetic Calibration Curve. An Objective Treatment. *Archaeometry*, (39):153–168, 1997.

A.J. Biggin and T. Poidras. First-order symmetry of weak-field partial thermoremanence in multi-domain ferromagnetic grains. 1. Experimental evidence and physical implications. *Earth and Planetary Science Letters*, (245):438–453, 2006a.

A.J. Biggin and T. Poidras. First-order symmetry of weak-field partial thermoremanence in multi-domain (MD) ferromagnetic grains. 2. Implications for Thellier-type palaeointensity determination. *Earth and Planetary Science Letters*, (245):438–453, 2006b.

R.F. Butler. *Paleomagnetism: Magnetic Domains to Geologic Terranes*. Blackwell Scientific Publications, 1992.

L. Casas and A. Incoronato. Distribution analysis of errors due to relocation of geomagnetic data using the 'conversion via pole' (cvp) method: implications on archaeomagnetic data. *Geophysical Journal International*, (169):448–454, 2007.

B. Cech. *Die keramischen Funde der slawischen Wallanlage in Thunau am Kamp (NÖ) (Ein Beitrag zur Gliederung slawischer Keramik)*. Sonderdruck Zalai Muzeum 3, 1991, 1991.

B. Cech. *Die Produktion von Ferrum Noricum am Hüttenberger Erzberg: die Ergebnisse der interdisziplinären Forschungen auf der Fundstelle Semlach/Eisner in den Jahren 2003-2005*. Austria Antiqua, 2008.

B Cech. The production of ferrum Noricum at Hüttenberg, Austria - the results of archaeological excavations carried out from 2003 to 2010 at the site Semlach/Eisner. *Monographies Instrumentum*, (50):11–20, 2014.

Bibliography

A. Chauvin, Y. Garcia, P. Lanos, and F. Laubenheimer. Paleointensity of the geomagnetic field recovered on archaeomagnetic sites from France. *Physics of the Earth and Planetary Interiors*, (120):111–136, 2000.

U. Christensen, J. Aubert, and G. Hulot. Conditions for earth-like geodynamo models. *Earth and Planetary Science Letters*, (296):487–496, 2010.

R.S. Coe. Paleo-intensities of the earth's magnetic field determined from tertiary and quaternary rocks. *Journal of geophysical research*, (72):3247–3262, 1967.

R.S. Coe, S. Gromme, and E.A. Mankinen. Geomagnetic palaeointensities from radiocarbon-dated lava flows on hawaii and the question of the pacific non-dipole low. *Journal of geophysical research*, (83):1740–1756, 1978.

C.G. Constable, C.L. Johnson, and S.P. Lund. Global Geomagnetic Field Models for the Past 3000 Years: Transient or Permanent Flux Lobes? *Philosophical transactions of the Royal Society of London. Series A*, (358):991–1008, 2000.

A. Cox and R. Doell. Review of paleomagnetism. *Bulletin of the Geological Society of America*, (71):645–768, 1960.

K. Creer, E. Irving, and S. Runcorn. The direction of the geomagnetic field in remote epochs in great britain. *Journal of geomagnetism and geoelectricity*, (6):163–168, 1954.

L. Daly and M. Le Goff. An updated and homogenous world secular variation data base. 1. smoothing of the archaeomagnetic results. *Physics of the Earth and Planetary Interiors*, (93):159–190, 1996.

C. Davies and C. Constable. Insights from geodynamo simulations into long term geomagnetic field behaviour. *Earth and Planetary Science Letters*, (404):238–249, 2014.

M.J. Dekkers and H.N. Böhnel. Reliable absolute palaeointensities independent of magnetic domain state. *Earth and Planetary Science Letters*, (248):508–517, 2006.

G. Dobesch. Die Okkupation des Regnum Noricum durch Rom. *Studien zu den Militärgrenzen Roms*, (III):308–315, 1983.

D.J. Dunlop. Thermal enhancement of magnetic susceptibility. *Geophysical Journal International*, (40):439–451, 1974.

S. Ech-Chakrouni, J. Hus, and S. Spassov. Constraints of archaeomagnetic dating and field intensity determinations in three ancient tile kilns in Belgium. *Studia Geophysica et Geodaetica*, (57):585–604, 2013.

M. Evans and F. Heller. *Environmental magnetism: principles and applications of enviromagnetics*. International geophysics series, 2003.

K. Fabian. A theoretical treatment of paleointensity determination experiments on rocks containing pseudo-single or multi domain magnetic particles. *Earth and Planetary Science Letters*, (188):45–58, 2001.

K. Fabian and R. Leonhardt. Multiple-specimen absolute palaeointensity determination: An optimal protocol including pTRM normalization, domain-state correction, and alteration test. *Earth and Planetary Science Letters*, (297):84–94, 2010.

R.A. Fisher. Dispersion on a sphere. *Proceedings of the Royal Society*, (217):295–305, 1953.

H. Friesinger. Thunau am Kamp. *Fundberichte aus Österreich*, (14):179–180, 1976.

H. Friesinger and L. Friesinger. *Die Befestigungsanlagen in Thunau. 5000 Jahre Siedlung im Garser Raum.* Katalogreihe des Krahuletz-Museums Eggenburg 3, 1975.

Y. Gallet, A. Genevey, and M. Le Geoff. Three millennia of directional variation of the earth's magnetic field in western europe as revealed by archeological artefacts. *Physics of the Earth and Planetary Interiors*, (131):81–89, 2002.

A. Genevey, Y. Gallet, S. Jesset, E. Thébault, J. Bouillon, and A. Lef'evre. New archeointensity data from french early medieval pottery production (6th-10th century ad). tracing 1500 years of geomagnetic field intensity variations in western europe. *Physics of the Earth and Planetary Interiors*, (257):205–219, 2016.

M. Gómez-Paccard, A. Chauvin, P. Lanos, and J. Thiriot. New archeointensity data from spain and the geomagnetic dipole moment in western europe over the past 2000 years. *Journal of Geophysical Research*, (113), 2008.

M. Gómez-Paccard, A. Chauvin, P. Lanos, P. Dufresne, M. Kovacheva, M. Hill, E. Beamud, E. Blain, A. Bouvier, P. Guibert, and Archaeological Working Team. Improving our knowledge of rapid geomagnetic field intensity changes observed in europe between 200 and 1400 ad. *Earth and Planetary Science Letters*, (355):131–143, 2012.

K. Gruber and E. Schnepp. *Archaeodirection recorded in metamorphic rocks with magnetic anisotropy used for construction of combustion chambers: Two examples from Carinthia, Austria*, pages 82–82. 2008.

D. Gubbins and E. Herrero-Bervera. *Encyclopedia of Geomagnetism and Paleomagnetism*. Springer, 2007.

M. Hanesch, H. Stanjek, and N. Petersen. Thermomagnetic measurements of soil iron minerals: the role of organic carbon. *Geophysical Journal International*, (165):53–61, 2006.

G. Hervé, E. Schnepp, A. Chauvin, Lanos P., and N. Nowaczyk. Archaeomagnetic results on three Early Iron Age salt-kilns from Moyenvic (France). *Geophysical Journal International*, (185):144–156, 2011.

G. Hervé, A. Chauvin, and Lanos P. Geomagnetic field variations in Western Europe from 1500 BC to 200 AD. Part II: New intensity secular variation curve. *Physics of the Earth and Planetary Interiors*, (218):51–56, 2013.

E. Irving. *Paleomagnetism and its Application to Geological and Geophysical Problems*. Wiley, New York, 1964.

A. Jackson, R.T. Jonkers, and M.R. Walker. Four centuries of geomagnetic secular variation from historical records. *Philosophical Transactions of the Royal Society A*, (358):957–990, 2000.

D. Jault and P. Cardin. On dynamic geodynamo models with imposed velocity as energy source. *Physics of the Earth and Planetary Interiors*, (111):75–81, 1999.

D. Kern and K. Grömer. Abdrücke im Schnur-Design. *Archäologie Österreichs*, (26/1): 27–33, 2015.

J.I. Kirschvink. The least-squares line and plane ond the analysis of palaeomagnetic data. *Geophysical Journal, Royal Astronomical Society*, (62):699–718, 1980.

M. Korte, C.G. Genevey, C.G. Constable, U. Frank, and E. Schnepp. Continuous geomagnetic field models for the past 7 millennia: 1. a new global data compilation. *Geochemistry, Geophysics, Geosystems*, (6), 2005.

M. Korte, F. Donadini, and C.G. Constable. Geomagnetic field for 0-3 ka: 2. A new series of time varying global models. *Geochemistry, Geophysics, Geosystems*, (10):1–24, 2009.

M. Kovacheva. Archaeomagnetic database from bulgaria: the last 8000 years. *Physics of the Earth and Planetary Interiors*, (102):145–151, 1997.

D. Krása, C. Heunemann, R. Leonhardt, and N. Petersen. Experimental procedure to detect multidomain remanence during thellier-thellier experiments. *Physics and Chemistry of the Earth, Parts A/B/C*, (28):681–687, 2003.

P. Lanos, M. LeGoff, M. Kovachva, and Em Schnepp. Hierarchical modelling of archaeomagnetic data and curve estimation by moving average technique. *Geophysical Journal International*, (160):440–476, 2005.

Ph. Lanos. *Bayesian inference of calibration curves: application to archaeomagnetism*. Springer Verlag, London, 2004.

M Le Goff. Lissage et limites d'incertitude des courbes de migration polaire: pondération des données et extension de la statistique de fisher. *C:R:Acad.Sci., Sér II*, (311):1191–1198, 1990.

M. Le Goff, Y. Gallet, A. Genevey, and N. Warmé. On archaeomagnetic secular variation curves and archeomagnetic dating. *Physics of the Earth and Planetary Interiors*, (134): 134–211, 2002.

R. Leonhardt, C. Heunemann, and D. Krása. Analyzing absolute paleointensity determinations: Acceptance criteria and the software ThellierTool4.0. *Geochemistry, Geophysics, Geosystems*, (5):1–10, 2004.

P.L. McFadden. Rejection of palaeomagnetic observations. *Earth and Planetary Science Letters*, (61):392–395, 1982.

P.L. McFadden and F.J. Lowes. The discrimination of mean directions drawn from fisher distribution. *Geophys. J.*, (67):19–33, 1981.

G. McIntosh and G. Catanzariti. An introduction to archaeomagnetic dating. *Geochronometria*, (25):11–18, 2006.

J. Meert, E. Tamrat, and J. Spearman. Non-dipole fields and inclination bias: insights from a random walk analysis. *Earth and Planetary Science Letters*, (214):395–408, 2003.

R. Merill and P. McFadden. The geomagnetic axial dipole field assumption. *Physics of the Earth and Planetary Interiors*, (139):171–185, 2003.

R.T. Merill, M.W. MacElhinny, and P.L. MacFadden. *The magnetic field of the earth: paleomagnetism, the core, and the deep mantle*. Acad. Press, 1998.

M. Monster, L. de Groot, and M. Dekkers. MSP-Tool: A VBA-Based Software Tool for the Analysis of Multispecimen Palaeointensity Data. *Front. Earth Sci.*, (3:86):1–9, 2015.

T. Nagata. *Rock magnetism*. Maruzen Comp. Ltd., 1961.

M.L. Néel. Nouvelle théorie du champ coercitif. *Physica*, (1-2):225–234, 1949.

H. Nelson, L. Hurwitz, and D. Knapp. *Magnetism of the Earth*. United States Government Printing Office, 1962.

M. Obenaus. Die frühmittelalterliche Talsiedlung von Thunau am Kamp. Grabungen 2004 bis 2014. *Archäologie Österreichs*, (26/1):9–21, 2015.

F.J. Pavón-Carrasco, M.L. Osete, J.M. Torta, and L.R. Gaya-Piqué. A regional archeomagnetic model for Europe for the last 3000 years, SCHA.DIF.3K: Applications to archeomagnetic dating. *Geochemistry, Geophysics, Geosystems*, (10):1–22, 2009.

F.J. Pavón-Carrasco, M.L. Rodriguez-Gonzalez, J. ans Osete, and J.M. Torta. A Matlab tool for archaeomagnetic dating. *Journal of Archaeological Science*, (38):408–419, 2011.

P. Riisager and J. Riisager. Detecting multidomain magnetic grains in Thellier palaeointensity experiments. *Physics of the Earth and Planetary Interiors*, (125):111–117, 2001.

E. Schnepp. *Die erdmagnetische Paläointensität im quartären Vulkanfeld der Westeifel*. Hochschulschriften Bd.31, Münster, 1991.

E. Schnepp. Archäomagnetische Datierung in Deutschland und Österreich. *Archäologisches Korrespondenzblatt*, (37):313–320, 2007.

E. Schnepp. *Archäomagnetische Datierung der Schmelzöfen 1 bis 5*. Austria Antiqua, 2008.

E. Schnepp. *Archäomagnetische Datierungen auf der Grabung Semlach/Eisner bei Knappenberg (Kärnten)*. Austria Antiqua - in press, 2016.

E. Schnepp. *Archäomagnetische Messungen an den Öfen der Talsiedlung in Thunau am Kamp (Niederösterreich)*. Archäologische Forschungen in Niederösterreich (AFNÖ) - accepted, 2017.

E. Schnepp and P. Lanos. Archaeomagnetic secular variation in germany during the past 2500 years. *Geophysical Journal International*, (163):479–490, 2005.

E. Schnepp and P. Lanos. A preliminary secular variation reference curve for archaeomagnetic dating in austria. *Geophysical Journal International*, (166):91–96, 2006.

E. Schnepp, R. Pucher, C. Goedicke, A. Manzano, U. Müller, and P. Lanos. Paleomagnetic directions and Thermoluminescence dating from a bread oven-floor sequence in Lübeck (Germany): a record of 450 years of geomagnetic secular variation. *Journal of Geophysical Research*, (108):53–66, 2003.

E. Schnepp, R. Pucher, J. Reinders, U. Hambach, H. Soffel, and I. Hedley. A german catalogue of archaeomagnetic data. *Geophysical Journal International*, (157):64–78, 2004.

E. Schnepp, K. Worm, and R. Scholger. Improved sampling techniques for baked clay and soft sediments. *Physics and Chemistry of the Earth*, (33):407–413, 2008.

E. Schnepp, M. Obenaus, and P. Lanos. Posterior archaeomagnetic dating: an example from the Early Medieval site Thunau am Kamp, Austria. *Journal of Archaeological Science: Reports*, (2):688–698, 2015.

E. Schnepp, R. Leonhardt, M. Korte, and J. Klett-Drechsel. Validity of archaeomagnetic field recording: an experimental pottery kiln at Coppengrave, Germany. *Geophysical Journal International*, (205):622–635, 2016.

U. Schwertmann and R.M. Taylor. *Iron oxides*. SSSA Book Series no. 1, 1989.

J. Shaw. A new method of determining the magnitude of the palaeomagnetic field: Application to five historic lavas and five archaeological samples. *Geophysical Journal International*, (39):133–141, 1974.

H. Soffel. *Paläomagnetismus und Archäomagnetismus*. Springer-Verlag, Berlin, 1991.

U. Stieglitz, R. amd Müller. Experimental demonstration of a homogeneous two scale dynamo. *Phys. Fluids*, (13):561–564, 2001.

P. Stückler. *Geophysikalische Prospektion im Raum der heimgesagten Sideritlagerstätte am Hüttenberger Erzberg*. Published Master thesis, Montanuniversität Leoben, 2010.

E. Szameit. 50 Jahre Ausgrabungen in Gars-Thunau. Anmerkungen zu einem immer aktuellen archäologischen Großprojekt. *Archäologie Österreichs*, (26/1):2–8, 2015.

D. Tarling and M. Dobson. Archaeomagnetism: An error assessment of fired material observations in the british directional database. *Journal of Geomagnetism and Geoelectricity*, (47):5–18, 1995.

L. Tauxe. Inclination flattening and the geocentric axial dipole hypothesis. *Earth and Planetary Science Letters*, (233):247–261, 2005.

E. Tema, A. Morales, J. Goguitchaichvili, and P. Camps. New archaeointensity data from Italy and geomagnetic field intensity variation in the Italian Peninsula. *Geophysical Journal International*, (193):603–614, 2013.

E. Thellier. Sur l'aimantation des terres cuites et ses applications géophysiques. *Ann. Inst. Geophys. Globe Univ. Paris*, (16):157–302, 1938.

E. Thellier. Sur la direction du champ magnétique terrestre, en france, durant les deux derniers millénaires. *Physics of the Earth and Planetary Interiors*, (24):89–132, 1981.

E. Thellier and O. Thellier. Sur l'intensité du shamp magnetique terrestre dans le passé historique et geologique. *Ann. Geophys.*, (15):285–376, 1959.

P.A. Tipler. *Physics for Scientists and Engineers, Thirs Edition*. Freeman, New York, 1994.

R.J. Veitch, G. Hedley, and J.J. Wagner. An investigation of the intensity of the geomagnetic field during roman times using magnetically anisotropic bricks and tiles. *Arch. Sc. Geneve*, (37):359–373, 1984.

G. Walach, R. Scholger, and B. Cech. Geomagnetic and Geoelectric Prospection on a Roman Iron Production Facility in Hüttenberg, Austria (Ferrum Noricum). *Archaeological Prospection*, (18):149–158, 2011.

I. Zananiri, C.M. Batt, P. Lanos, D.H. Tarling, and P. Linford. Archaeomagnetic secular variation in the uk during the past 4000 years and its application to archaeomagnetic dating. *Physics of the Earth and Planetary Interiors*, (160):97–107, 2007.

J.D.A. Zijderveld. *A.C. demagnetization of rocks: analysis of results*. Elsevier, Amsterdam, 609p, 1967.

Appendix

Appendix A.

Thellier Results

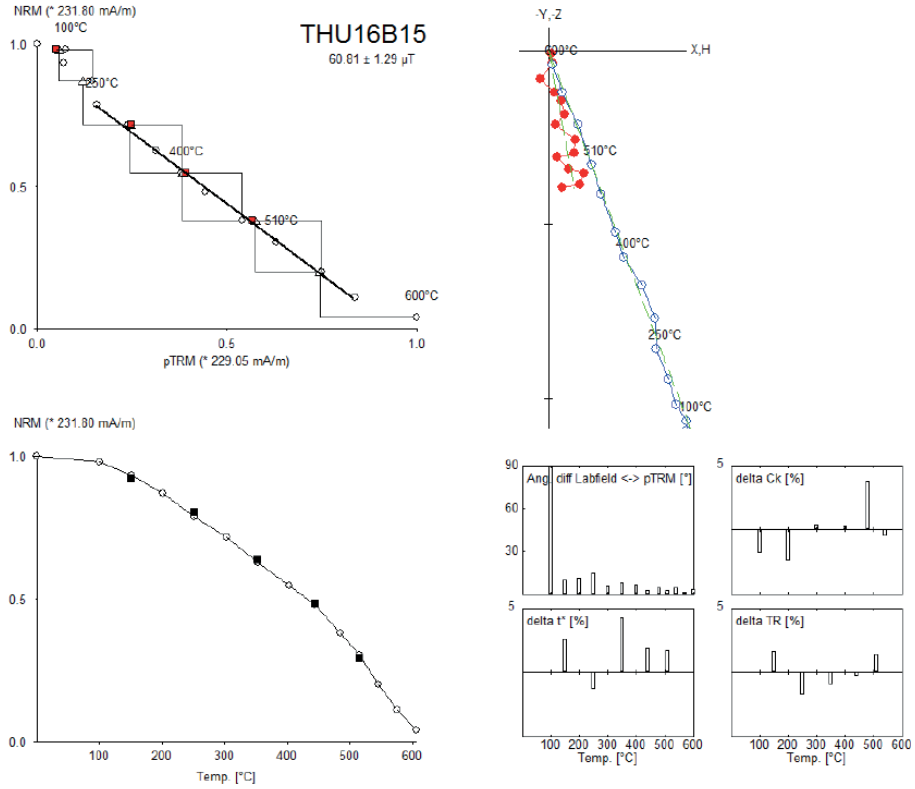

Figure A.1.: Result of Thellier experiment of THU16B15. Shown are Arai plot (upper left), Zijderveld diagram (upper right), NRM decay curve (lower left) and plots of angular difference of H_{Lab} - pTRM, δ CK (relative check error), δ t* (normalized tail of pTRM and δ TR (difference between first and repeatet demagnetisation) (lower right).

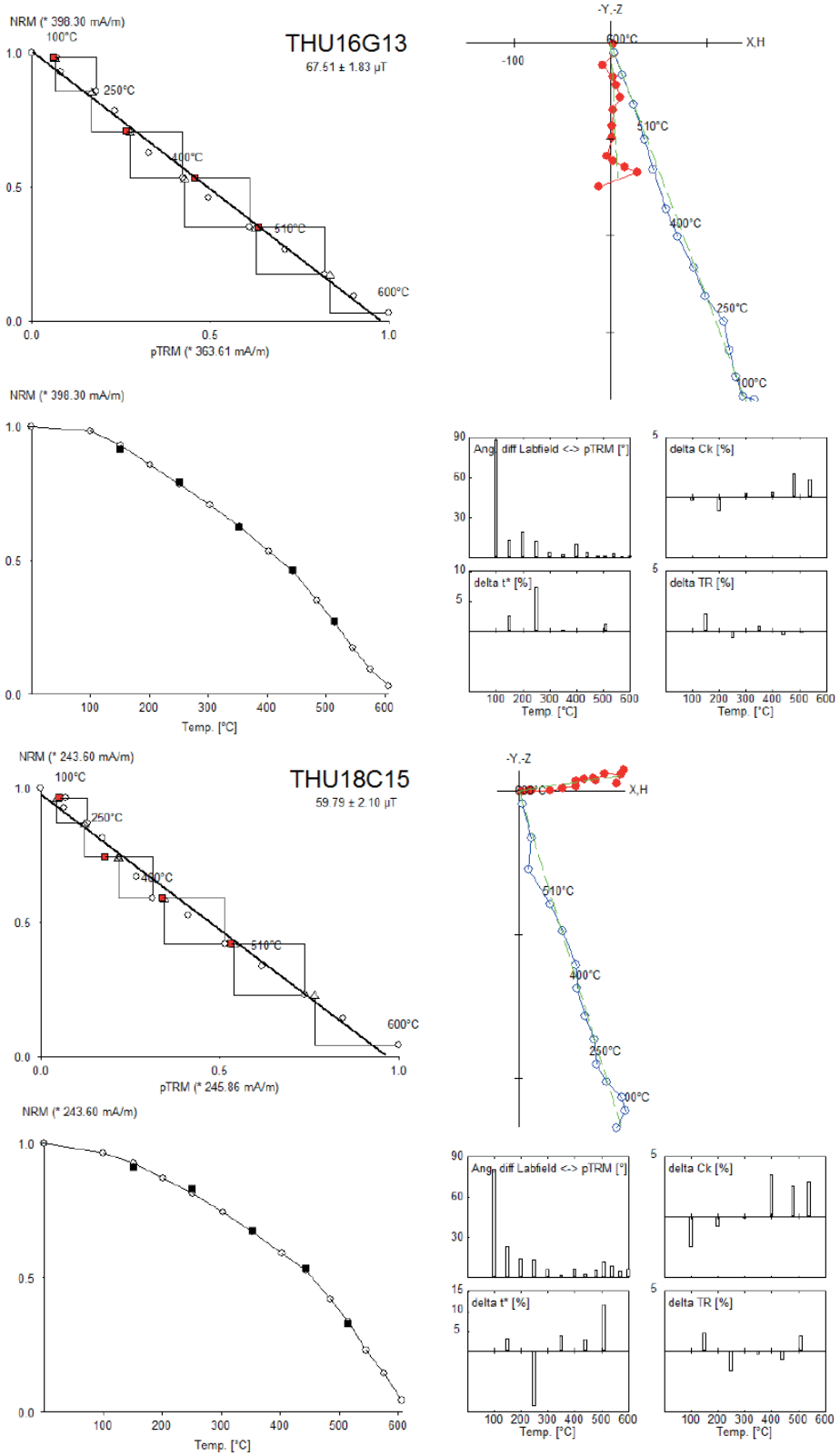

Figure A.2.: Result of Thellier experiments of THU16G13 and THU18C15. For explanations see figure A.1.

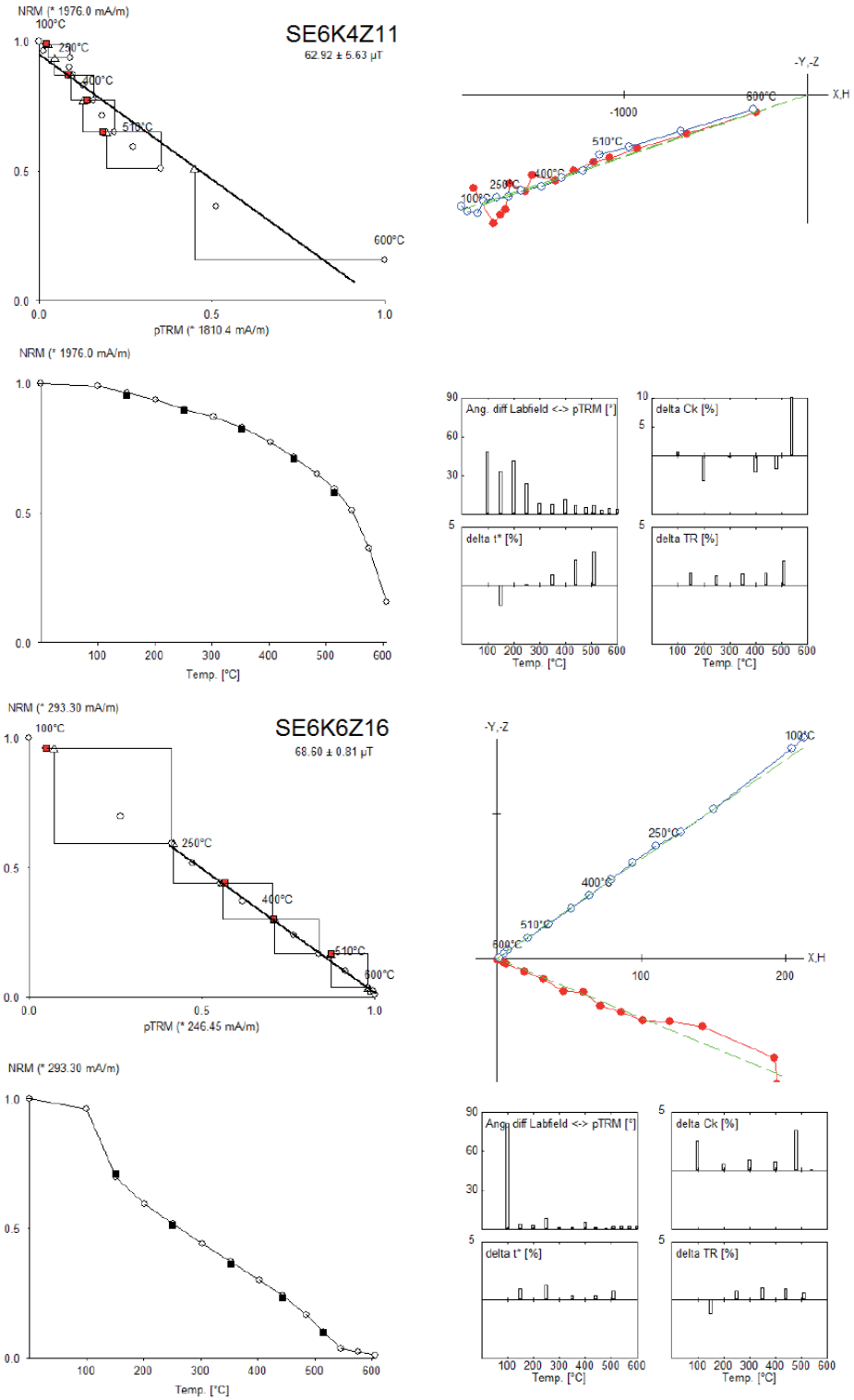

Figure A.3.: Result of Thellier experiments of SE6K4Z11 and SE6K6Z16. For explanations see figure A.1.

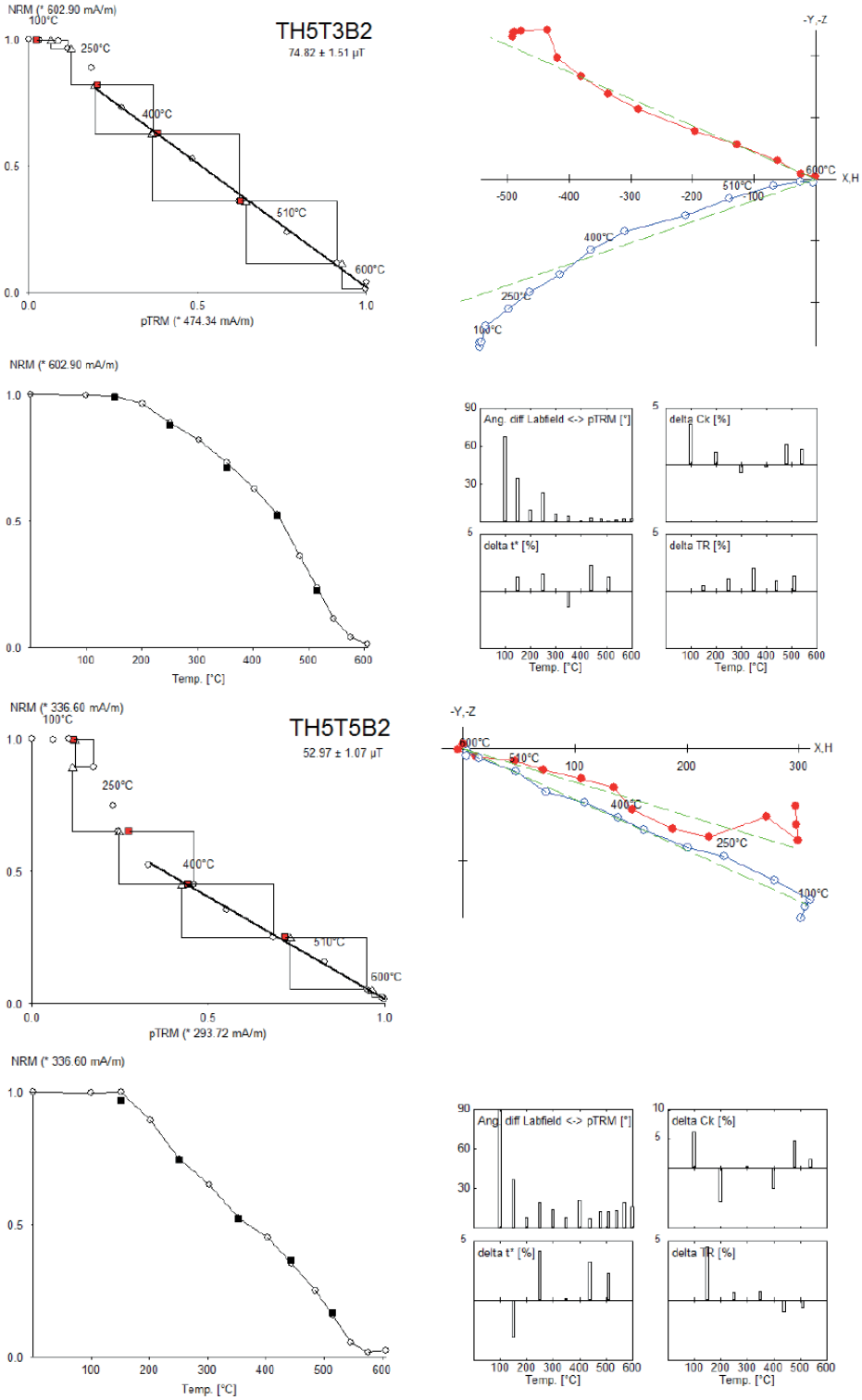

Figure A.4.: Result of Thellier experiments of TH5T3B2 and THU5T5B2. For explanations see figure A.1.

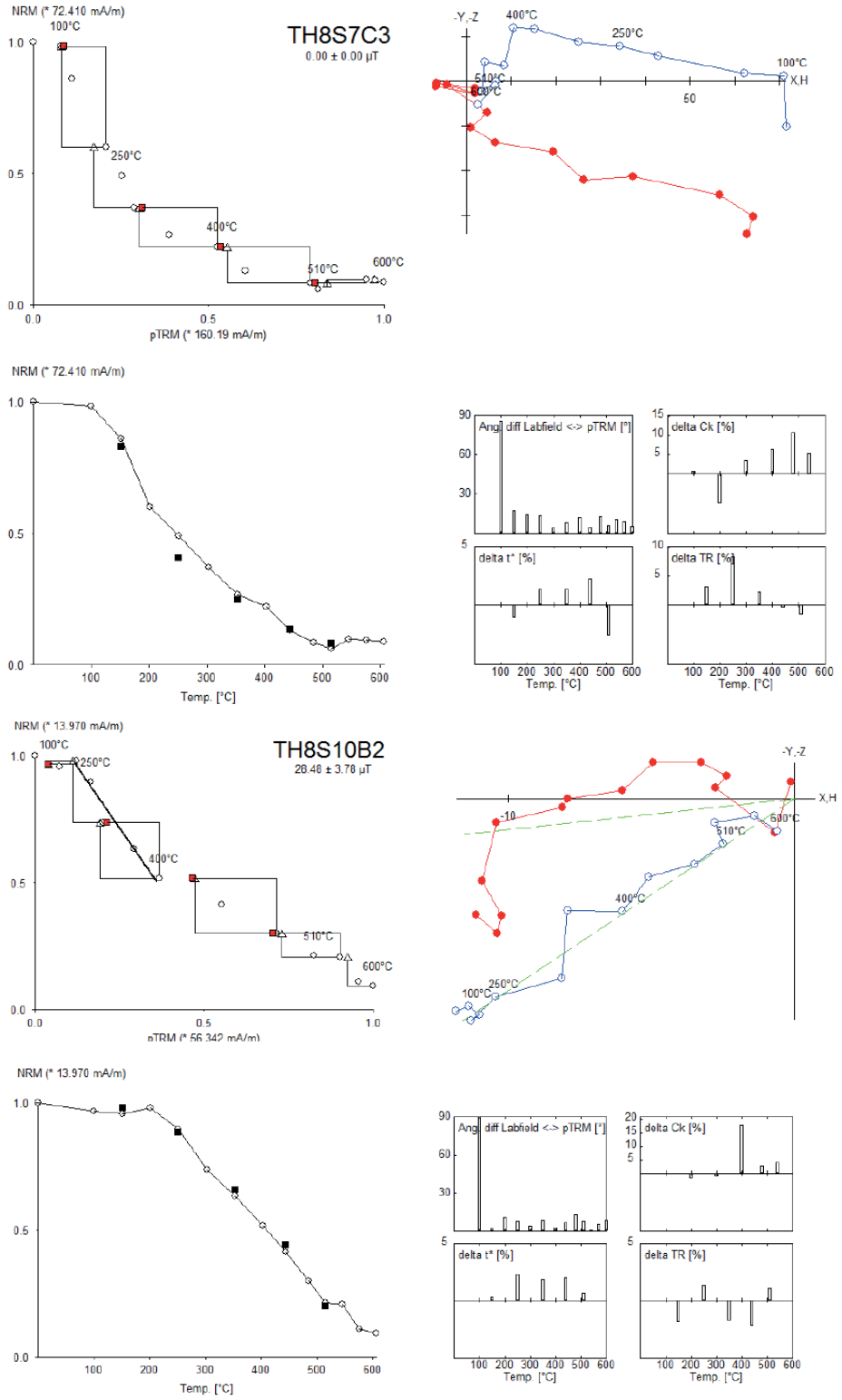

Figure A.5.: Result of Thellier experiments of TH8S7C3 and TH8S10B2. For explanations see figure A.1.

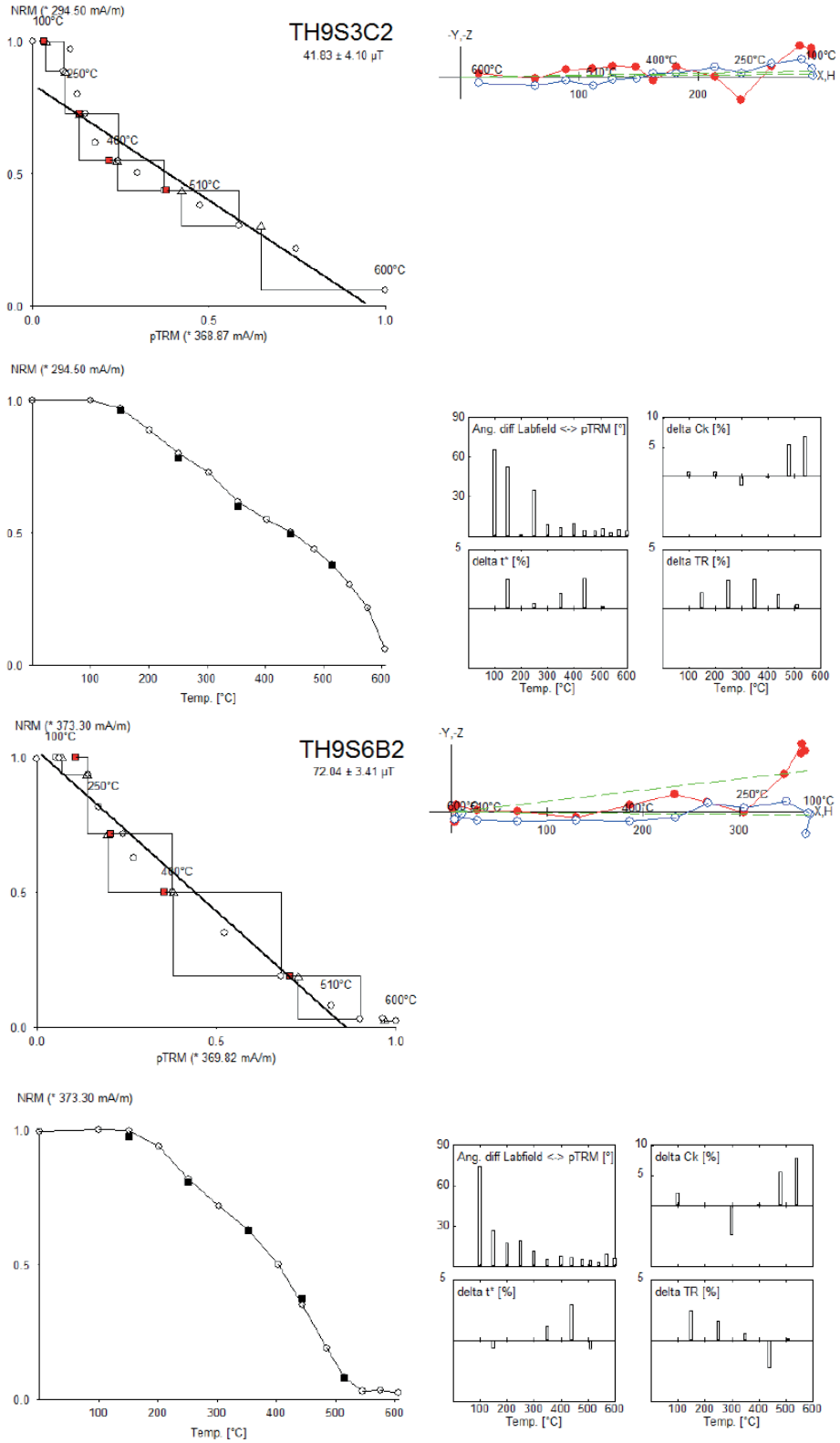

Figure A.6.: Result of Thellier experiments of TH9S3C2 and TH9S6B2. For explanations see figure A.1.

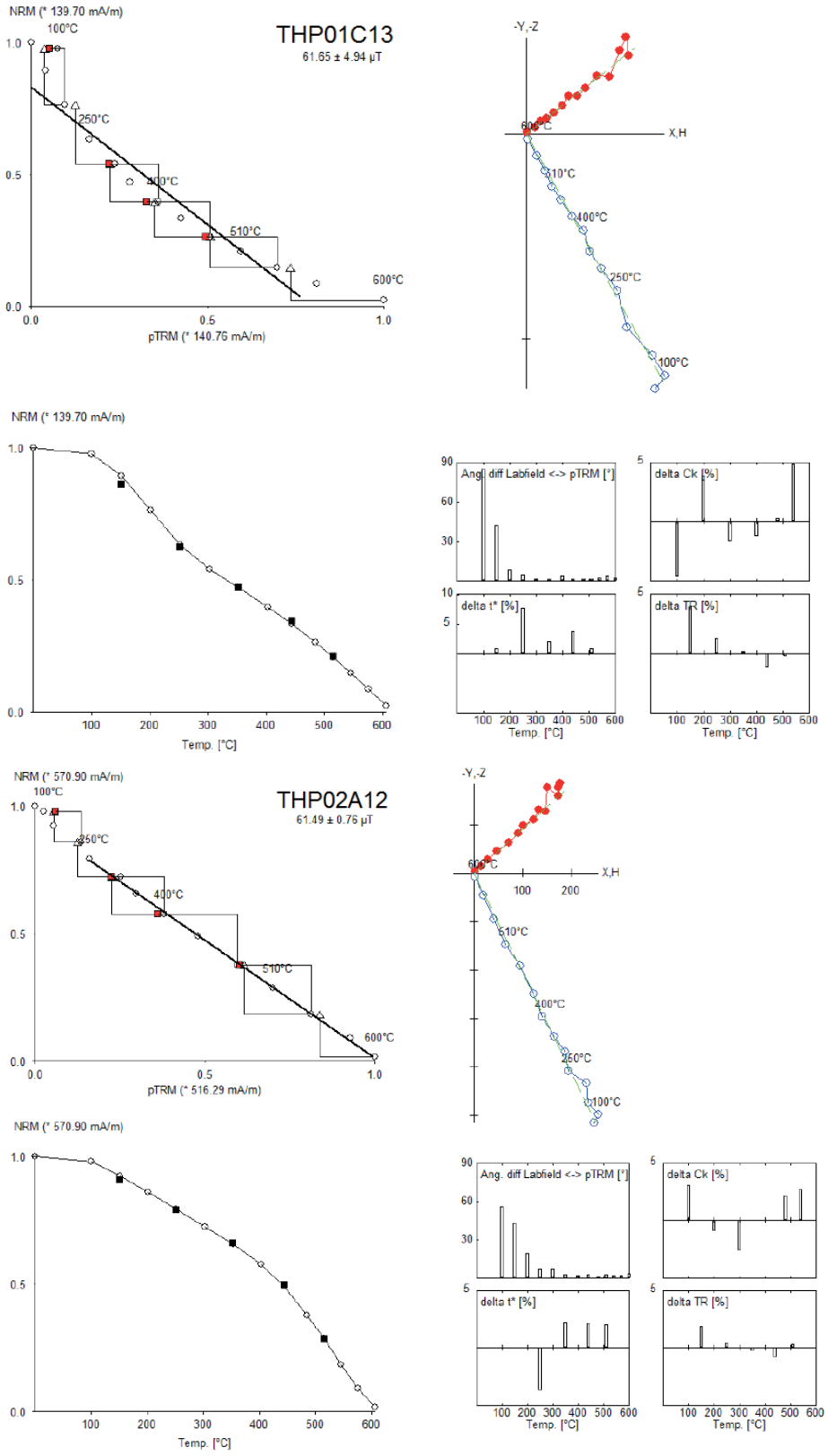

Figure A.7.: Result of Thellier experiments of THP01C13 and THUP02A12. For explanations see figure A.1.

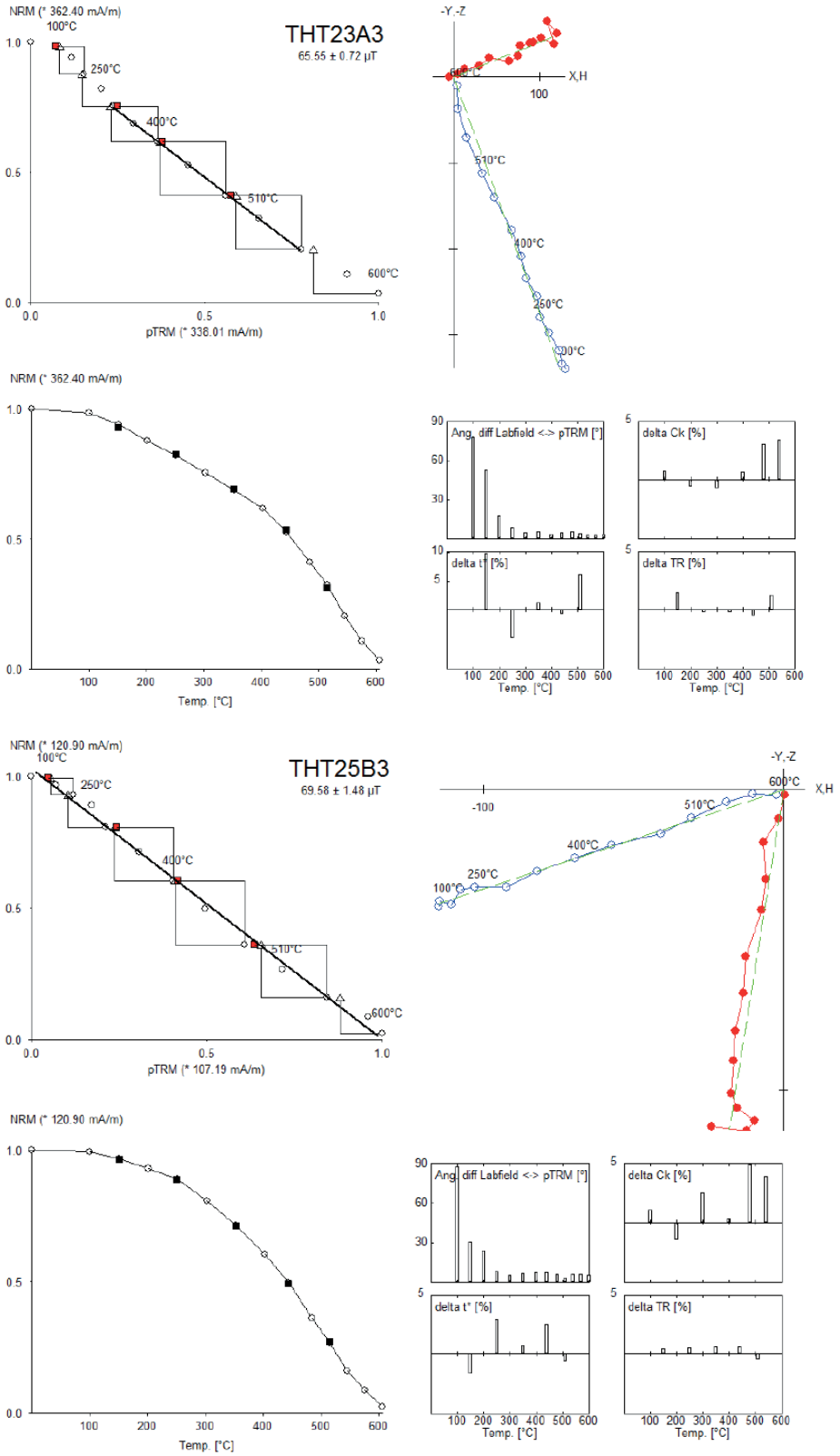

Figure A.8.: Result of Thellier experiments of THT23A3 and THT25B3. For explanations see figure A.1.

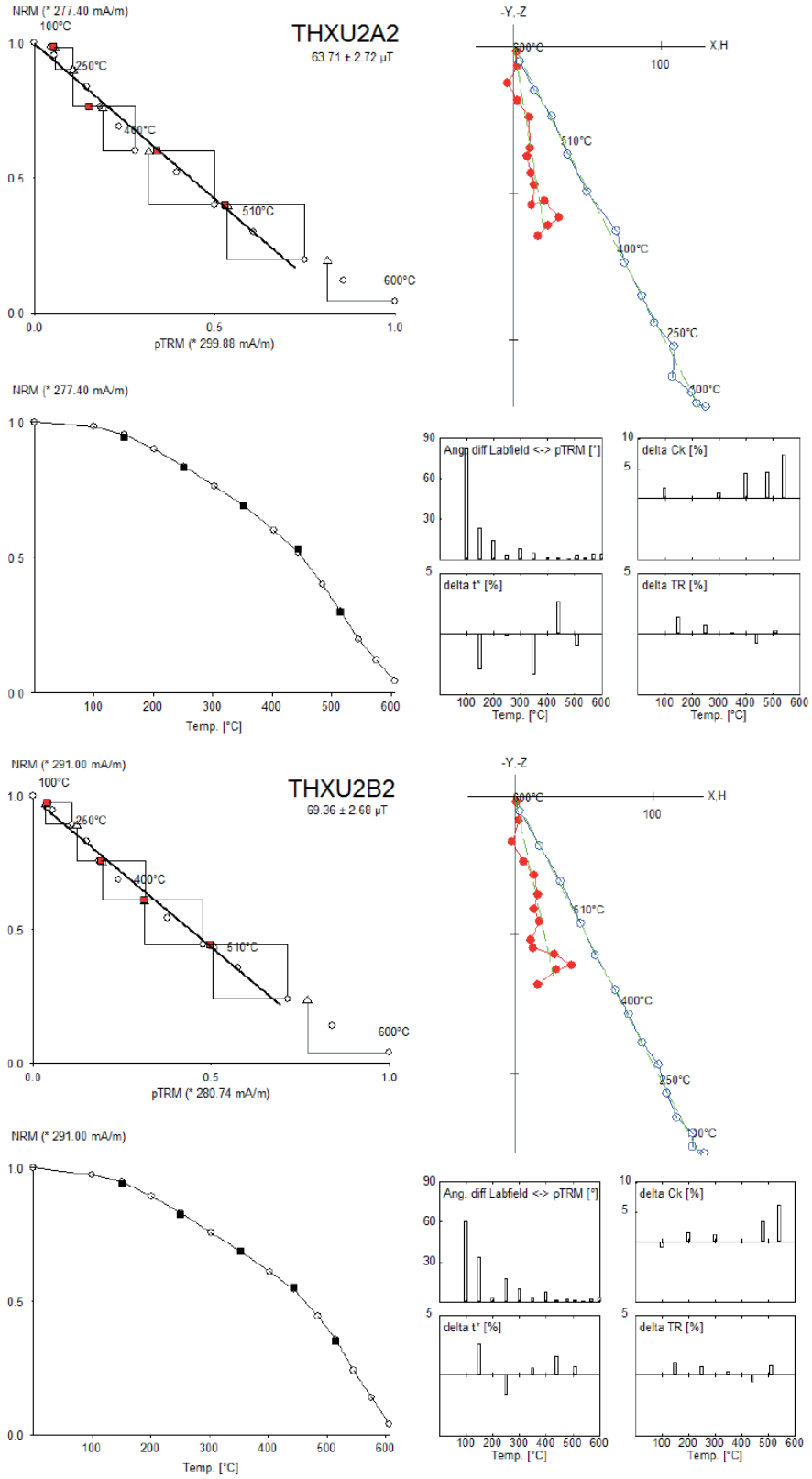

Figure A.9.: Result of Thellier experiments of THXU2A2 and THXU2B2. For explanations see figure A.1.

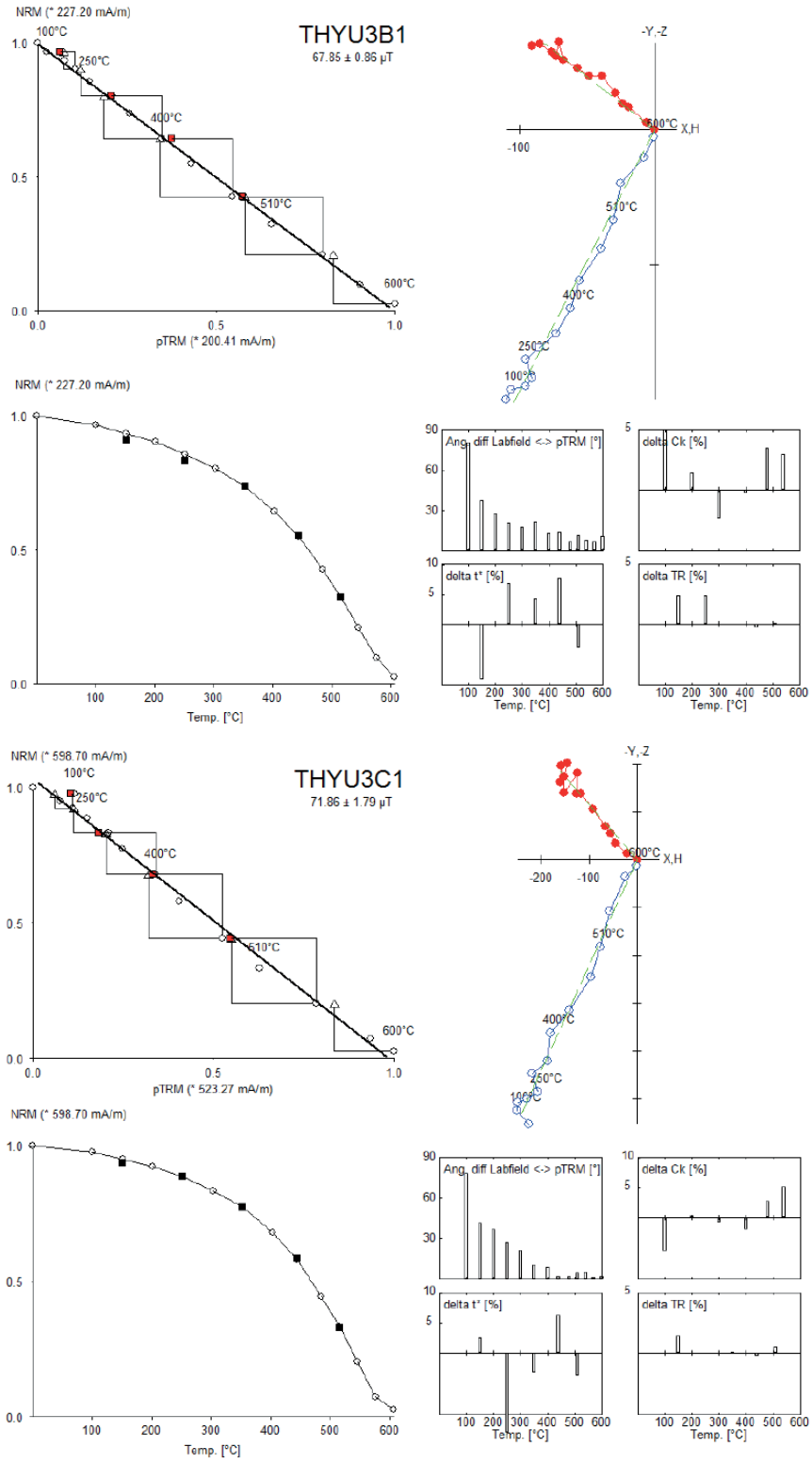

Figure A.10.: Result of Thellier experiments of THYU3B1 and THYU3C1. For explanations see figure A.1.

Appendix B.

MSP Method Results

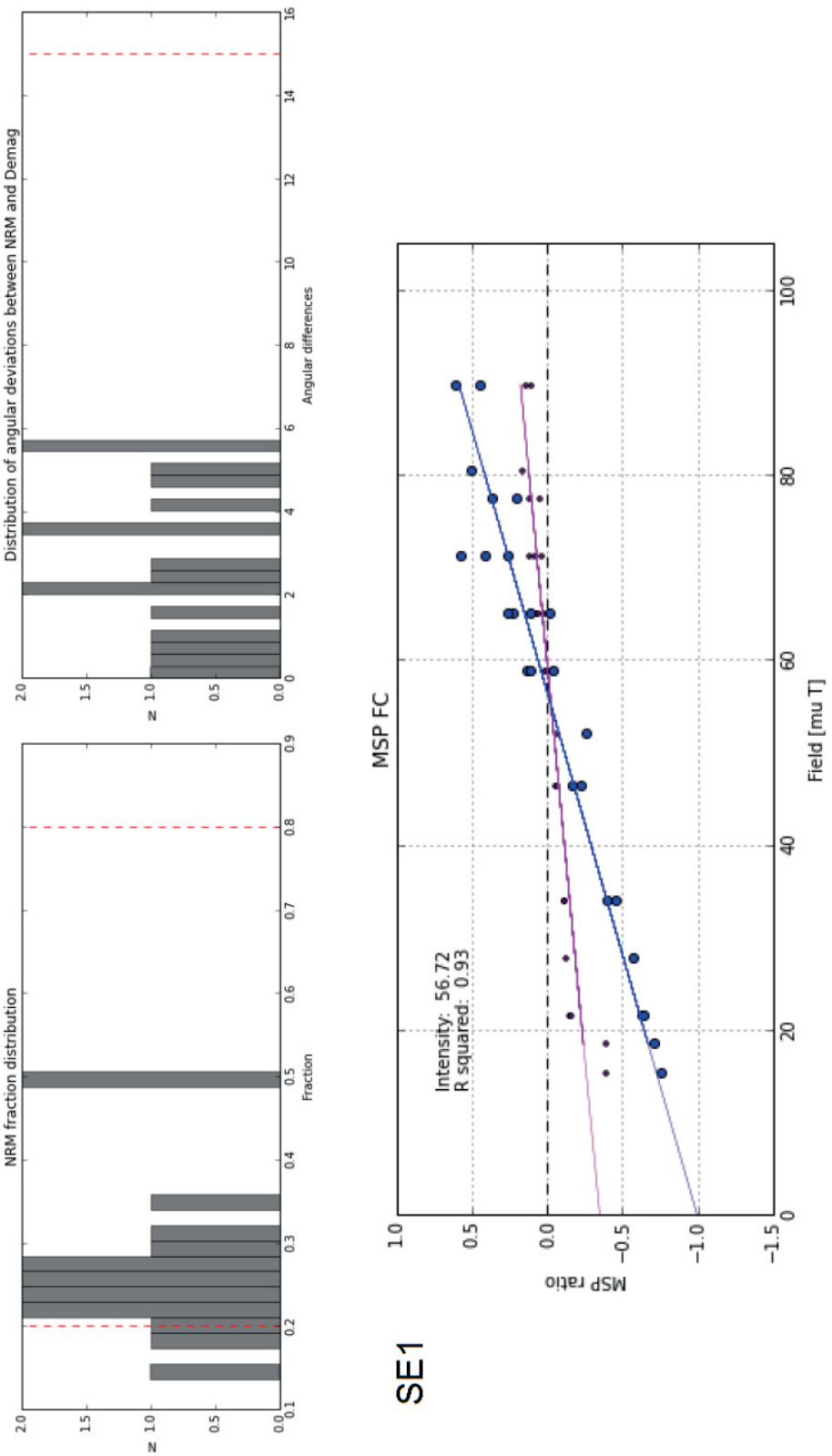

Figure B.1.: MSP result of SE1. Shown are NRM fraction distribution (upper left), the distribution of angular deviation between NRM and demagnetisation (upper right) and the resulting plot of the fraction corrected MSP result.

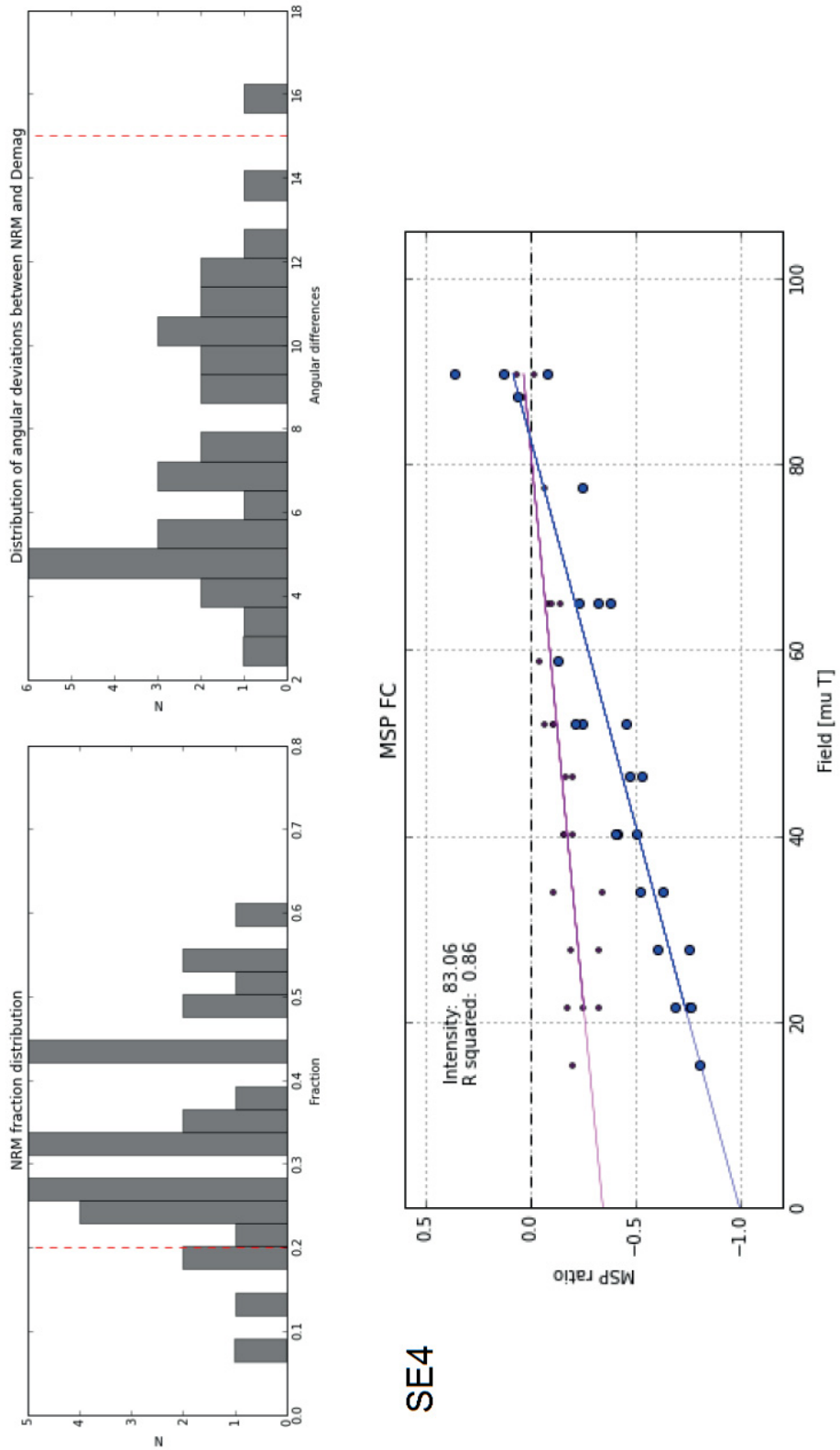

Figure B.2.: MSP result of SE4. For explanation see figure B.1.

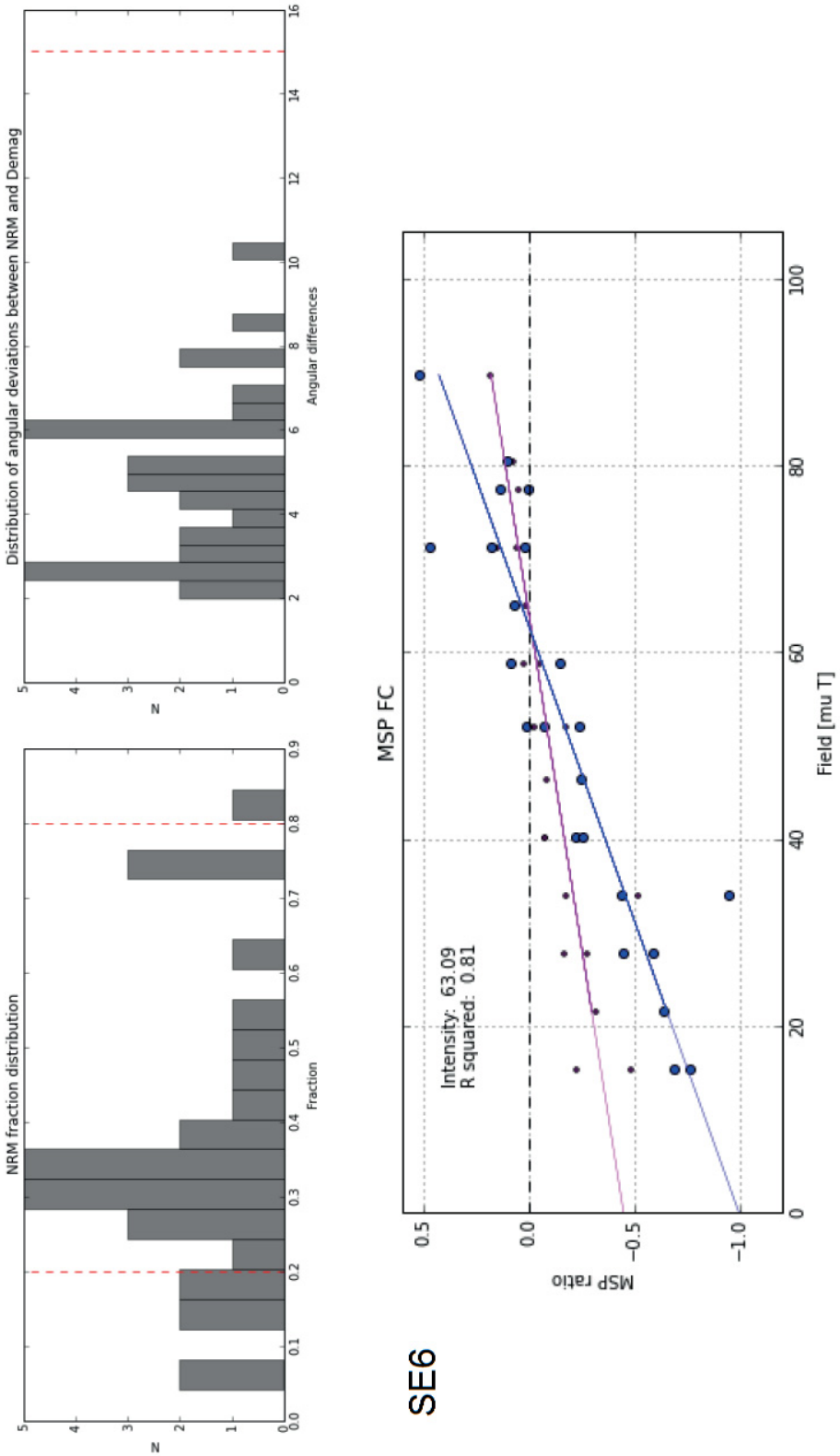

Figure B.3.: MSP result of SE6. For explanation see figure B.1.

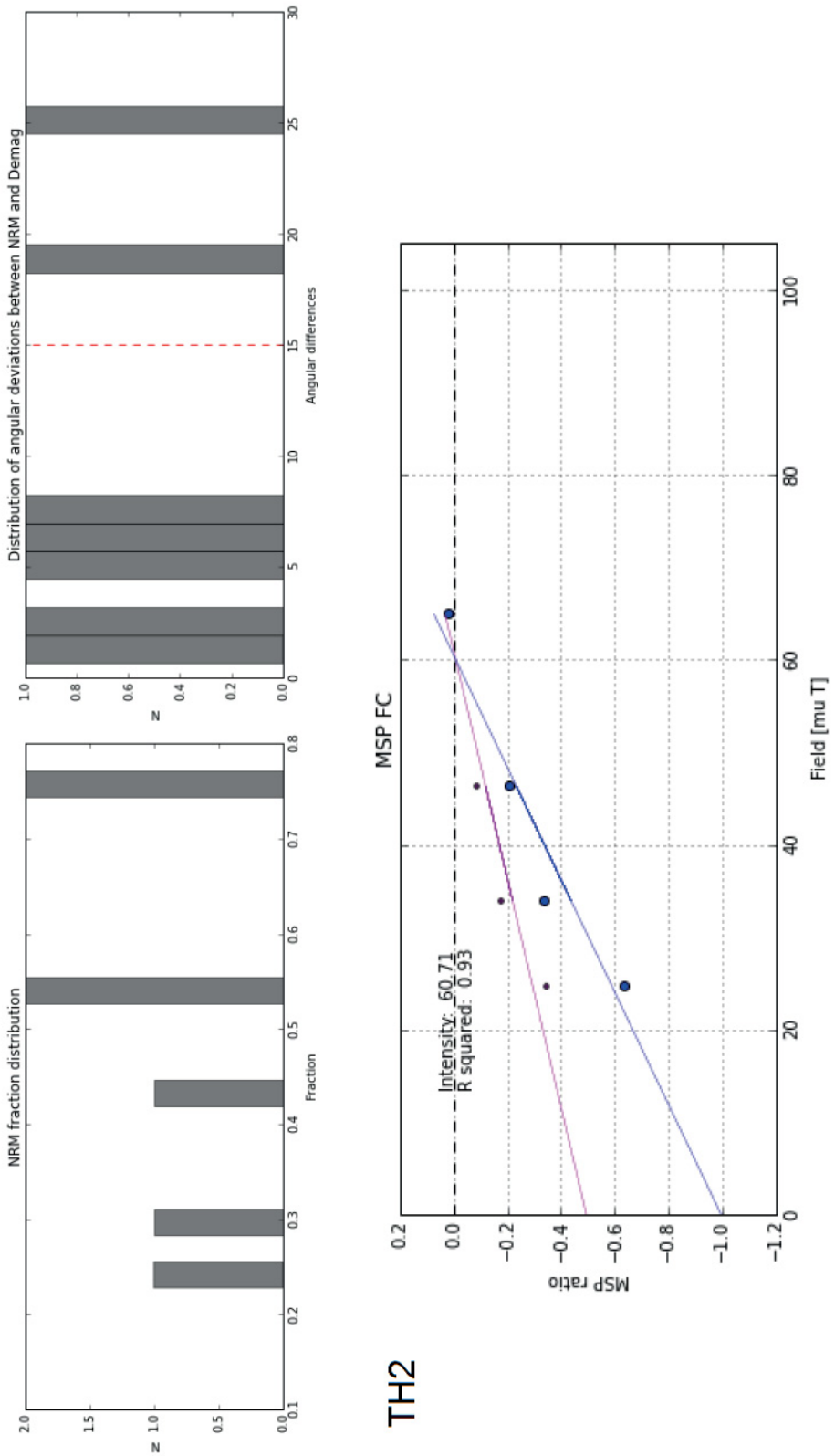

Figure B.4.: MSP result of TH2. For explanation see figure B.1.

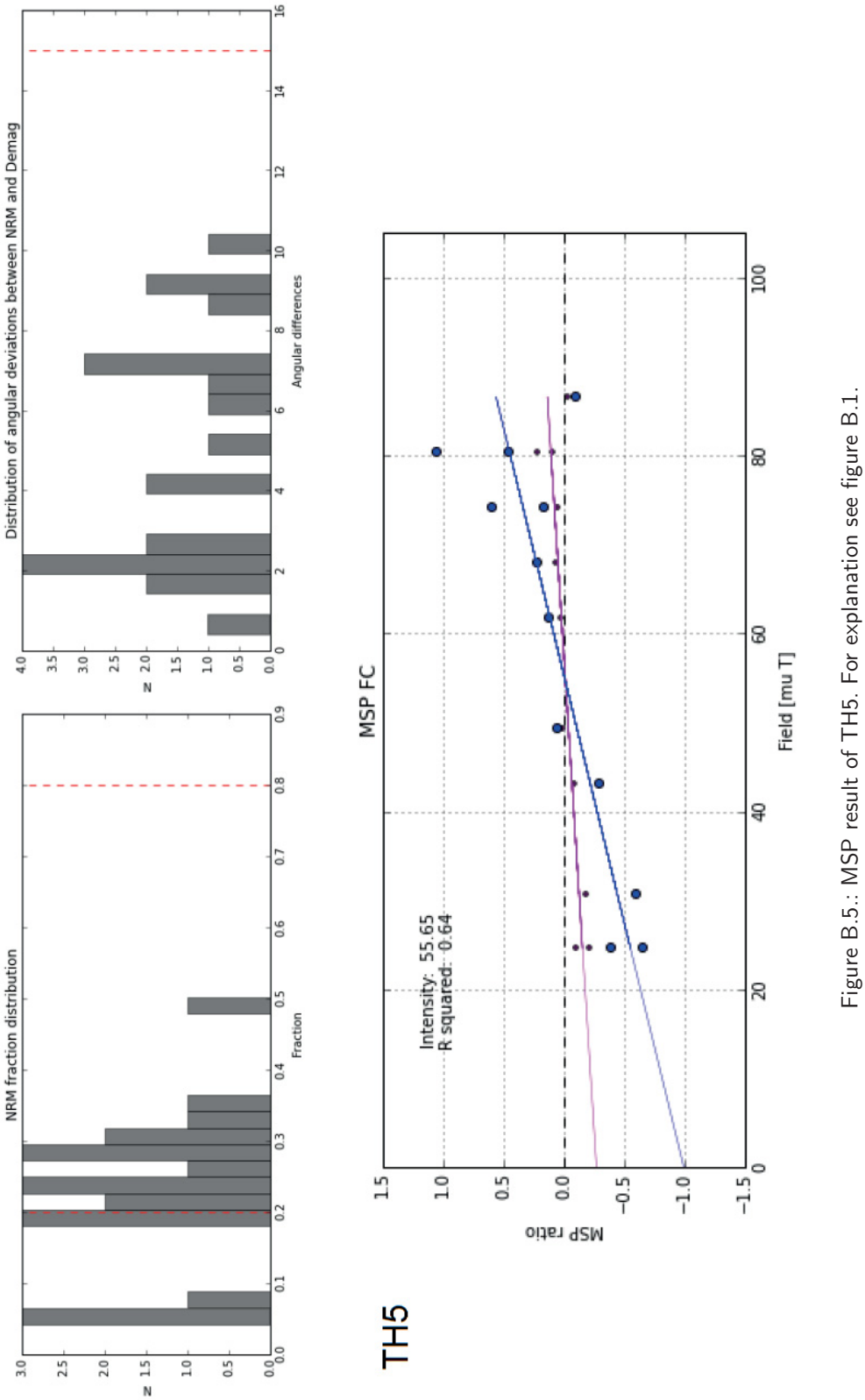

Figure B.5.: MSP result of TH5. For explanation see figure B.1.

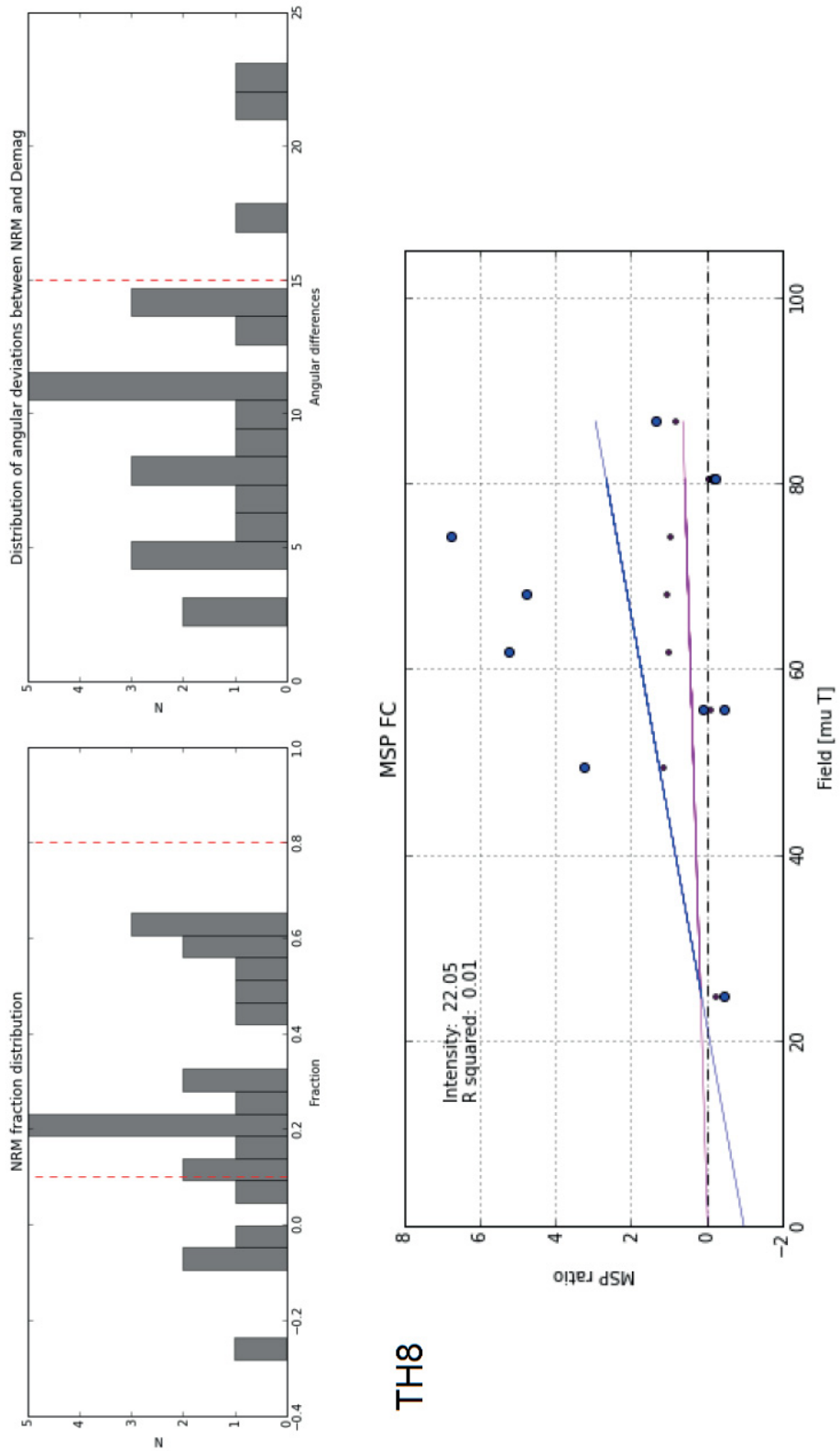

Figure B.6.: MSP result of TH8. For explanation see figure B.1.

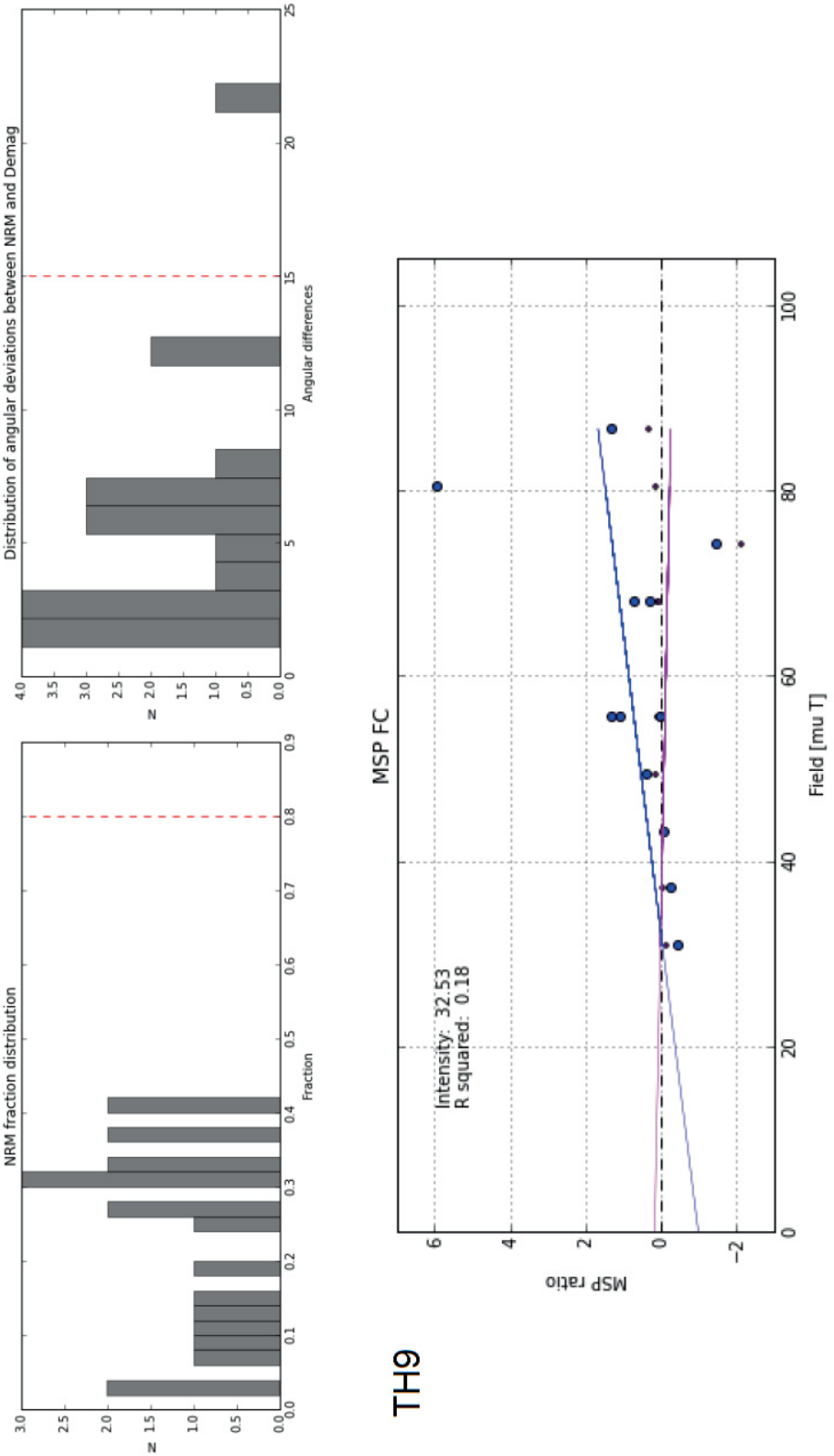

Figure B.7.: MSP result of TH9. For explanation see figure B.1.

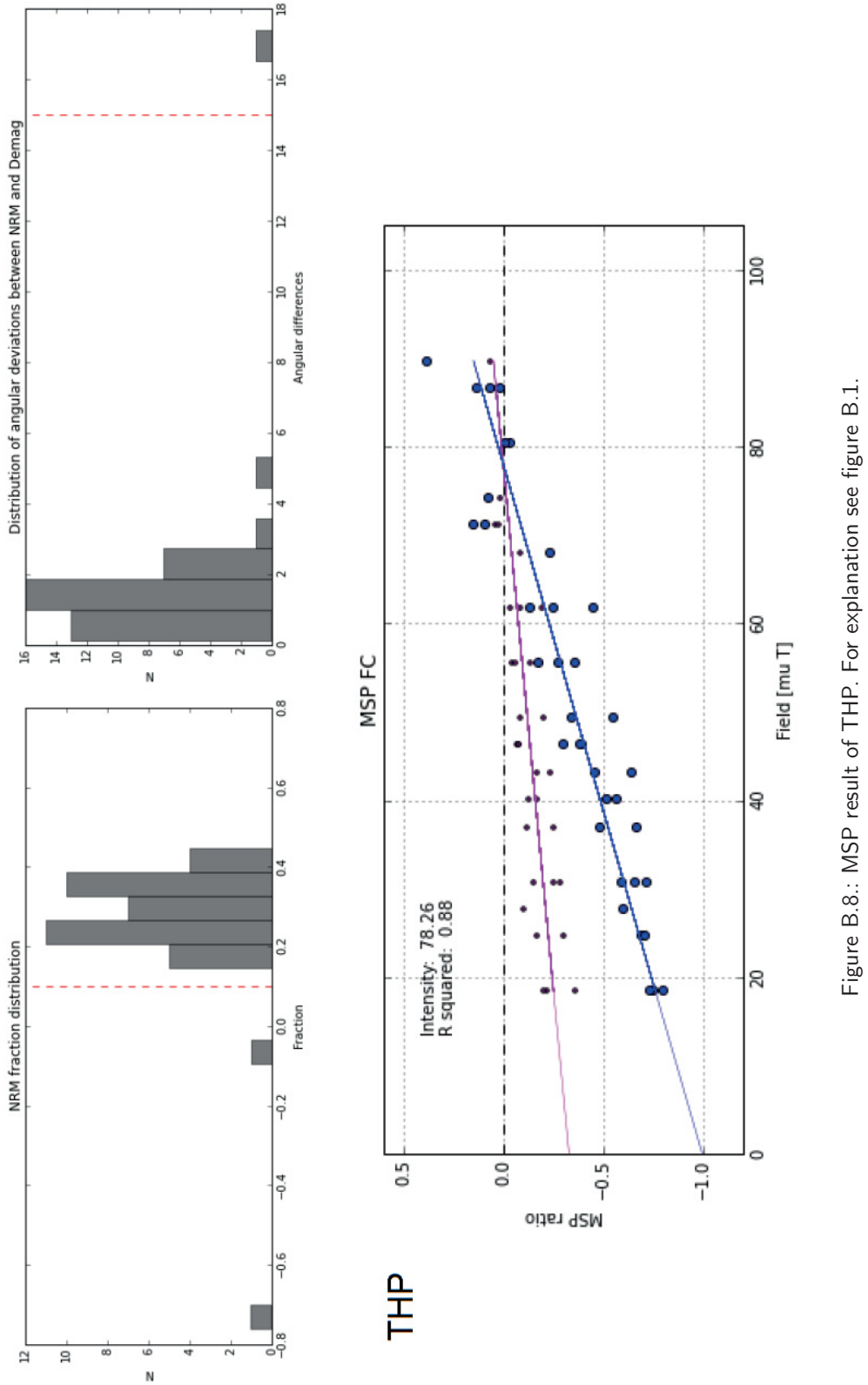

Figure B.8.: MSP result of THP. For explanation see figure B.1.

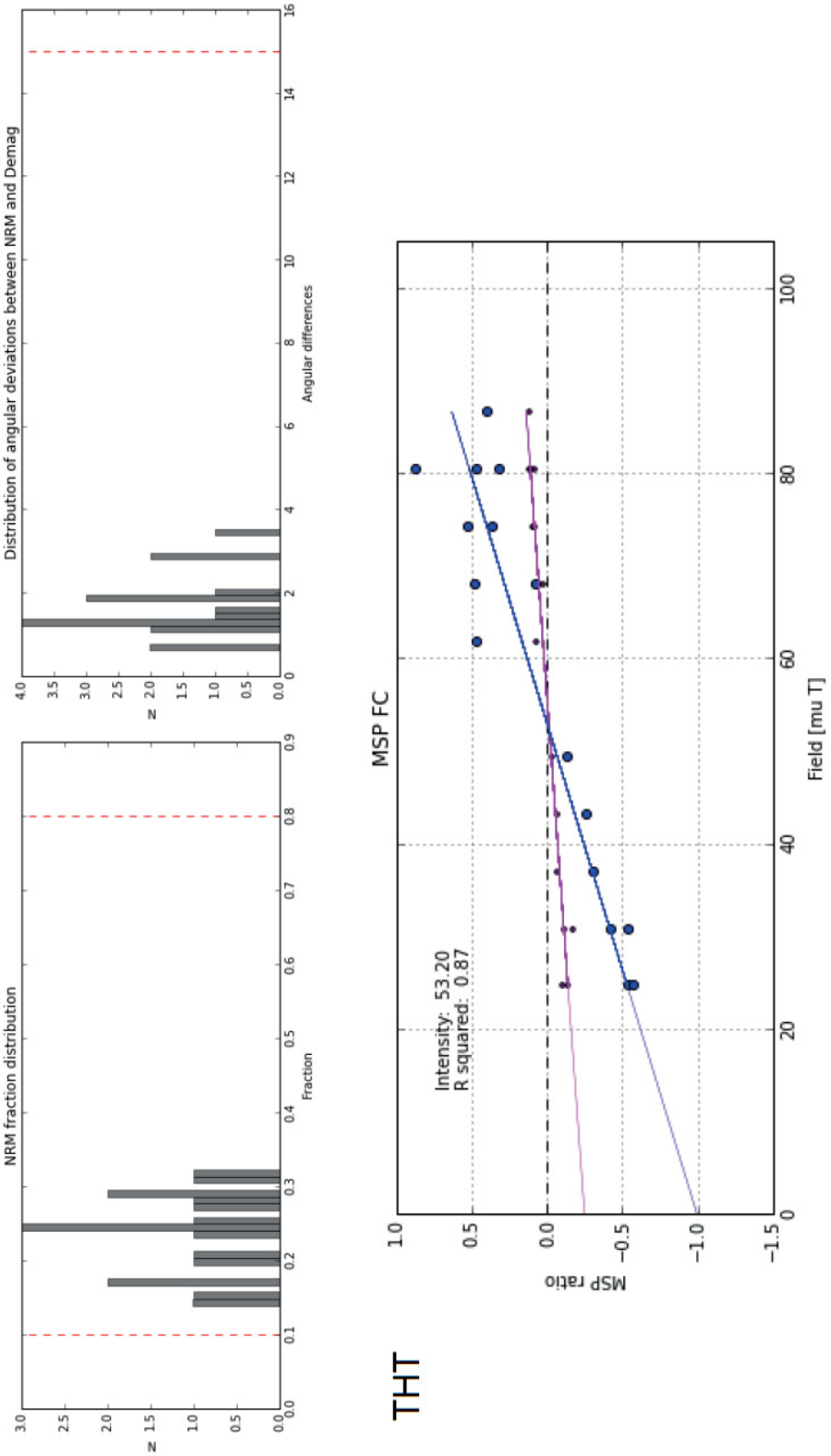

Figure B.9.: MSP result of THT. For explanation see figure B.1.

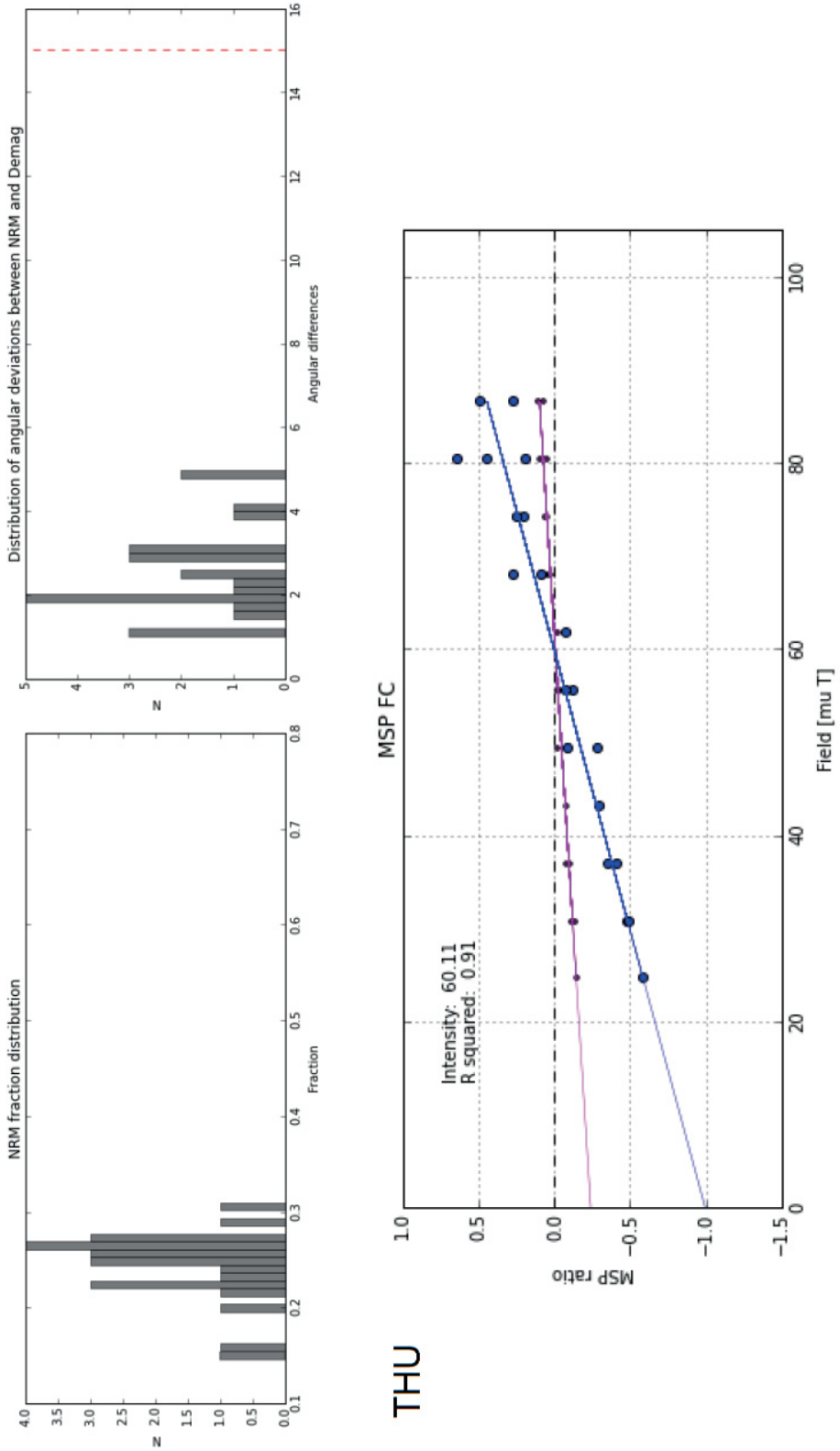

Figure B.10.: MSP result of THU. For explanation see figure B.1.

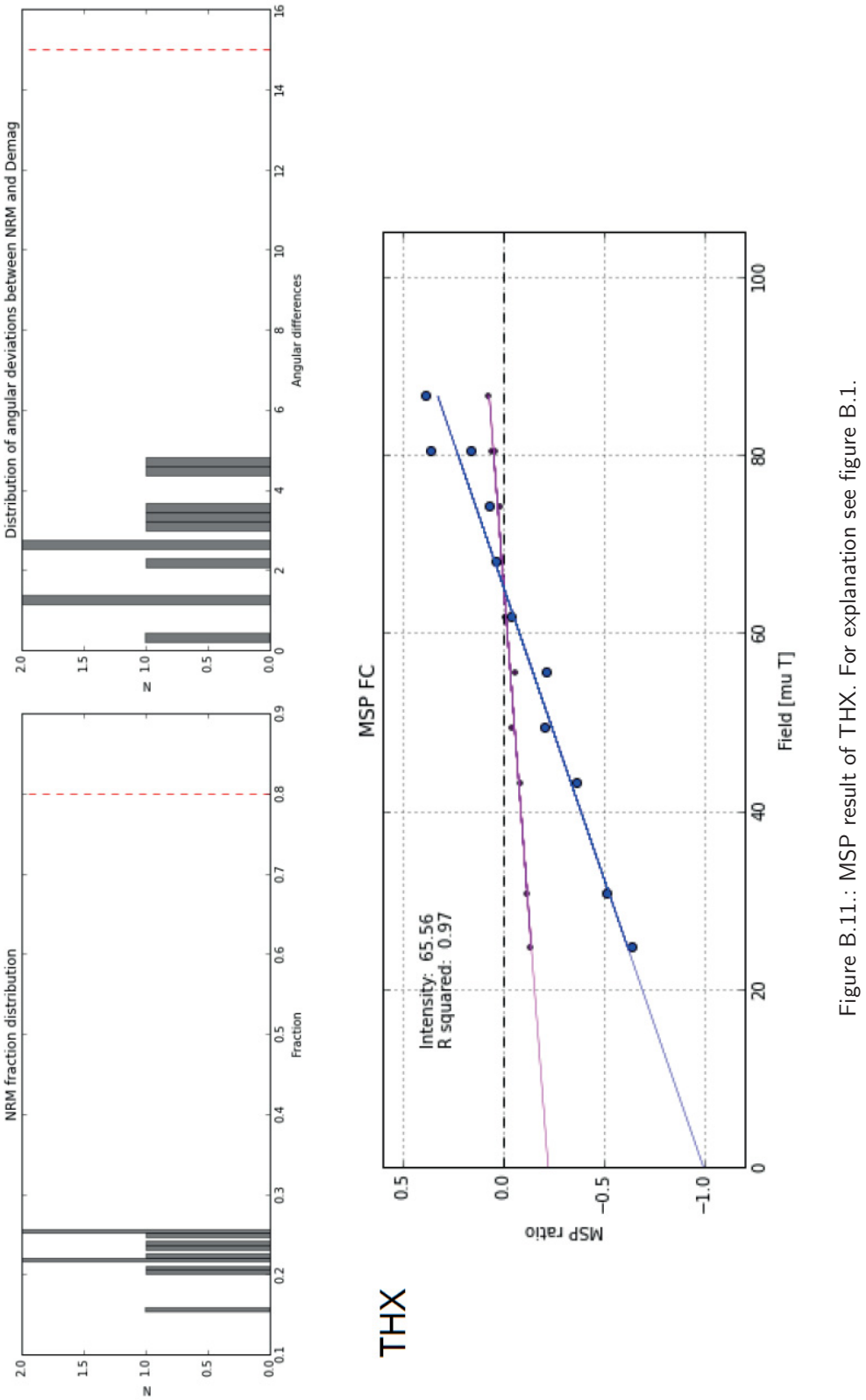

Figure B.11.: MSP result of THX. For explanation see figure B.1.

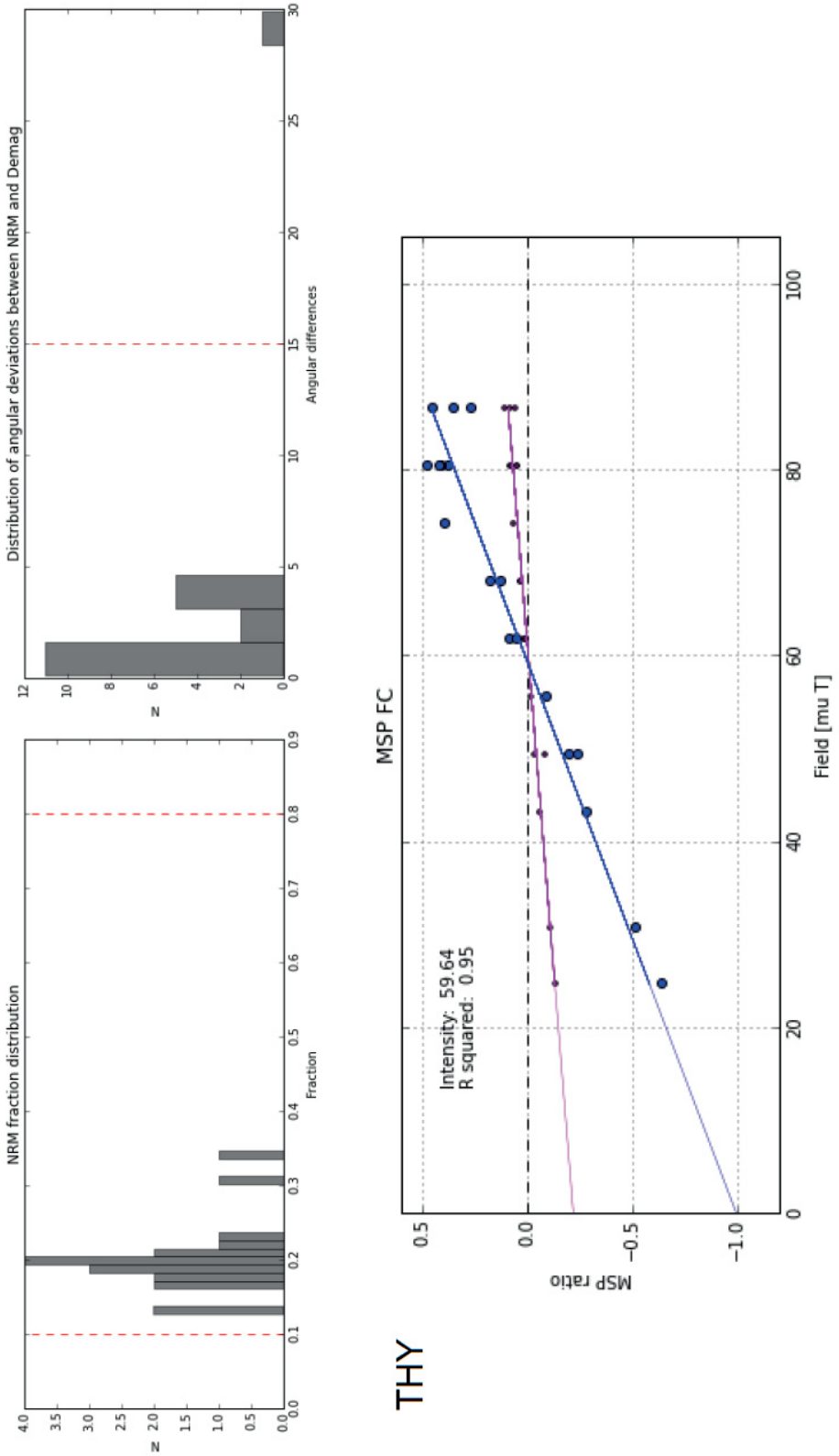

Figure B.12.: MSP result of THY. For explanation see figure B.1.